VISCOELASTICITY AND INSTABILITIES IN SOFT COMPOSITES

by

Yuhai Xiang

A dissertation submitted in partial fulfillment of

the requirements for the degree of

Doctor of Philosophy

(Mechanical Engineering)

at the

UNIVERSITY OF WISCONSIN–MADISON

2022

Date of final oral examination: 08/05/2022

The dissertation is approved by the following members of the Final Oral Committee:

Stephan Rudykh, Assistant Professor, Mechanical Engineering

AJ Boydston, Professor, Chemistry

Christian Franck, Professor, Mechanical Engineering

Tom Krupenkin, Associate Professor, Mechanical Engineering

Lih-Sheng (Tom) Turng, Professor, Mechanical Engineering

ACKNOWLEDGMENTS

I am grateful to all of those who helped, encouraged, mentored and supported me in my Ph.D. journey.

First and foremost, I would like to thank my beloved wife **Cuizhuo Lu**. Without her support, I cannot finish my Ph.D. dissertation. We experience sweet and sour together. She trusts me firmly and always supports me.

I am deeply grateful to my advisor **Prof. Stephan Rudykh**. He advises me to start a long-term project and encourage me to jump into it. One of the most gains from my Ph.D. journey is to dig into a hard problem with perseverance and patience. Now I have confidence that I can handle any challenge calmly and I believe this research habit is a lifelong benefit for me.

I would like to thank my collaborator. **Prof. AJ Boydston**, **Prof. Christian Franck**, **Dean Chen**, **Qi Yao**, **Nitesh Arora**, **Cody Schilling**, **Jialiang Tao** and **Danming Zhong** for their support and suggestions in my research projects.

I am grateful to my dissertation committee members **Prof. Tom Krupenkin** and **Prof. Lih-Sheng (Tom) Turning** for their attendance in my Ph.D. defense.

I would like to express my special gratitude to the brothers and sisters in Gracepoint. And I want to especially thank **Daniel Wu** and **Josiah Wernow** for being my mentor in the past year and for proofreading the first manuscript of my dissertation.

ABSTRACT

Harnessing the instabilities in soft composites, we can design materials with auxetic properties, tunable bandgap, negative viscoelasticity, and tunable stiffness. Moreover, instabilities leading to drastic microstructure transformations can be employed to develop soft robots, flexible electronics, and adhesive systems. However, it is difficult to change the instability-induced functionality once the required structure is fabricated since the geometry of the manufactured structure is fixed. Viscoelasticity as an intrinsic property for soft materials provides an opportunity to overcome this limitation and expand the design space. In particular, we could achieve richer functionality by adjusting temperature and applied strain rate without changing the geometric parameters. A deeper understanding of the influence of viscoelasticity in soft materials and the interplay between instability and viscoelasticity can be helpful for the design of soft materials with novel properties.

In this dissertation, we primarily focus on: (i) the nonlinear viscoelasticity of soft photocured polymer used in 3D printing and (ii) the interplay of viscoelasticity and instabilities in soft laminate and particulate composites. Firstly, we explore the influence of light intensity used in the 3D printing process on the viscoelasticity of soft photocured polymer. We present a theoretical framework and carried out the uniaxial test to validate the model. Next, we perform numerical analysis to detect the instabilities in visco-hyperelastic laminates and present a simple qualitative model to capture this rate-dependent critical buckling strain. Additionally, we probe the transformation of buckling patterns in the load-hold loading path and explore the dynamic properties of the buckled laminates. Finally, we study the rate-dependent critical strain and wavelength in soft particulate composites via numerical analysis and further examine the dynamic modulus, damping, stiffness and energy absorption of the buckled particulate composites.

TABLE OF CONTENTS

LIST OF FIGURES

LIST OF TABLES

CHAPTER 1

INTRODUCTION

1.1 Instability

Instability was regarded as a mode of failure and thus as something that should be avoided in engineering applications [45, 23]. Recently, however, it has been used to realize the novel functionalities of materials. For example, instability is utilized to design acoustic switches [146, 15], soft robotics [12, 157], materials with negative Poisson's ratio [16, 86, 110], tunable stiffness [101] and tunable color [84].

1.1.1 Instability in hyperelastic soft composites

In hyperelastic soft composites, instability can develop at microscopic and macroscopic length scales [50, 90]. Macroscopic instability refers to the buckling shape whose wavelength is significantly larger than the characteristic length of the microstructure. In contrast, the wavelength in microscopic instability is comparable with the characteristic length of the microstructure. The onset of macroscopic instabilities can be predicted by the loss of ellipticity requiring the evaluation of the effective tensor of elastic moduli. The effective tensor of elastic moduli can be evaluated either from phenomenological models [103, 104, 105, 106, 120] or computed through micromechanics-based homogenization approaches [2, 35, 60, 97, 95, 96, 127]. Analysis of microscopic instabilities, however, is more challenging and needs more sophisticated methods such as Bloch wave analysis [50, 114, 136]. Notice that Geymonat et al. [50] have rigorously proved that the Bloch-Floquet analysis is equivalent to the loss of ellipticity analysis for instability with infinite wavelength. Extensive research in instabilities has been carried out in 2D laminates, 3D fiber composites, and

particulate composites.

The pioneering work on the elastic instabilities in periodic laminates was given by [124] who derived an analytical expression for the compressive strength of linear elastic 2D laminate composites. Later on, Parnes and Chiskis [116] revisited the elastic buckling in periodic linear elastic laminates. They found that the microscopic instability will appear in dilute composites while the macroscopic instability appears in non-dilute composites. For instabilities in hyperelastic laminates, Triantafyllidis and Maker [136] investigated the microscopic and macroscopic instability of the 2D laminates under plane strain conditions and discussed the influence of geometry and material properties on the buckling behaviors of Stören − Rice and Mooney-Rivlin material. Merodio and Ogden [103, 104, 105, 106] presented a series of works on the instabilities of the nonlinear elastic fiber-reinforced composites under plane deformation by using the loss of ellipticity analysis. Nestorović and Triantafyllidis [114] demonstrated that load orientation, material properties, and fiber volume fraction could significantly affect the buckling of hyperelastic laminates. Bertoldi and Lopez-Pamies [18] analytically analyzed the macroscopic and microscopic instabilities in periodic 2D hyperelastic laminates with three phases (matrix, interphase and fiber) by using the loss of ellipticity and Bloch-Floquet analysis. They found that the interphase significantly affects the stability of the hyperelastic laminates. Li et al. [90] explored the instabilities in soft laminates through experiments, analytical methods and numerical simulations. The results showed mechanical behavior of the laminates can be tailored by selecting the material properties and geometry parameters. Rudykh and Bertoldi [125] investigated the anisotropic laminate magnetorheological elastomers (MREs) subjected to finite deformation. They provided a general analytical model which enables the prediction of the onset of the macroscopic instability of the laminate hyperelastic MREs. Gao and Li [47] investigated the mechanical behavior of

laminates with three phases: the stiffer interfacial phase, the softer matrix phase and the transition phase between the stiff and matrix phase. They explored the transition phase's influence on the linear elastic composites' instability through analytical analysis, and post-buckling analysis (FEA) was also performed to validate the analytical method. The results show that the transition zone significantly affects the wrinkling pattern. Greco et al. [57], Greco et al. [58] investigated the failure behaviors of periodic laminates by considering the interaction between local fiber buckling and fiber/matrix interface microcrack. They showed that the microcrack is vital to predicting the actual failure behavior of microcracked composites. Arora et al. [5] further investigated the influence of the inhomogeneous transition zone on the elastic instability of the hyperelastic laminates by using the Bloch-wave approach. They found that the critical strain and the buckling mode can be tuned by the properties of the inhomogeneous transition zone. Li et al. [87] explored the influence of compressibility on the onset of instability of the finite-deformed laminates through the Bloch-Floquet analysis. They found that the compressible laminates buckled at larger deformation compared to the incompressible laminates. El Hamdaoui et al. [41] predicted the fiber kinking and splitting failure modes in hyperelastic laminates with the loss of ellipticity analysis. Pathak et al. [117] studied the interplay between macroscopic and microscopic instabilities in the magnetoactive (MAE) laminates undergoing large deformation subjected to the external magnetic field. They showed that MAEs can develop an antisymmetric microscopic buckling mode that cannot be probed without a magnetic field. In addition, they demonstrated that the bucking pattern can be significantly tuned by the applied magnetic field. More recently, Li et al. [88] reported the experimental observations of instability-driven domain formations in soft hyperelastic laminates.

Agoras et al. [2] studied the macroscopic instability of the 3D fiber composites with

randomly distributed fibers under general finite deformation. They showed that the modulus contrast between fiber and matrix has a more significant effect on the onset of the macroscopic instability than other parameters. Rudykh and deBotton [127] studied the hyperelastic fiber composites with the loss of ellipticity analysis. In particular, they analyzed the instability of neo-Hookean and Gent composites. They showed that the critical stretch ratio mainly depends on fiber volume fraction and the contrast between the moduli of fiber and matrix. Slesarenko and Rudykh [132] investigated the macroscopic and microscopic instabilities in 3D periodic fiber composites undergoing finite deformations through Bloch-Floquet analysis. They also showed that the buckling mode is determined by the fiber volume fraction and the modulus contrast in the fiber and matrix phases. They also found that the macroscopic and microscopic instability tend to develop in composites with high and low fiber volume fractions, respectively. Galich et al. [46] investigated the role of fiber arrangement on elastic instabilities in 3D fiber composites. They found that the elastic instabilities can be tuned by the selection of the periodicity of the fiber arrangements. Moreover, they revealed that critical stretches are bound by the critical values for the 3D laminates and the fiber composites with square arrays of fibers. Li et al. [85] examined the elastic instabilities in the 3D-printed fiber composites and they found that the fiber will show softening behavior upon arriving at the critical strain. They observed the transition between the microscopic instability to macroscopic instability with an increase in the fiber volume fraction for the fiber composites with square in-plane periodicity. For composites with a rectangular in-plane periodicity of fibers, buckling develops in the direction with a narrower distance between fibers. Arora et al. [6] studied the influence of stiffening behavior on the microscopic and macroscopic instabilities in 3D fiber composites. They found that stiffening dictates the interplay between macroscopic and microscopic instabilities and matrix stiffening behavior

makes the composites more stable. More recently, Arora et al. [7] experimentally and numerically showed that the buckling orientation of fibers can be tuned by the in-plane periodicity and shear modulus contrast in 3D fiber composites.

For particulate composites with distributed inclusions, Lopez-Pamies and Castaneda [95, 96] provided a general homogenization framework that can probe the onset of macroscopic instabilities in cylindrical particulate composites undergoing finite deformation. Triantafyllidis et al. [137] investigated instability in the porous solids and particulate composites with periodically distributed stiff circular inclusions by a novel numerical technique based on Bloch wave analysis. Michel et al. [108] considered the influence of the fiber distribution, the fiber volume fraction, the material models and the cross-section of the inclusions on microscopic and macroscopic instabilities of the particulate composites. The effect of interface de-cohesion, matrix cavitation and fiber contact were also considered. They found that both macroscopic and microscopic instabilities can develop in the composites with periodic inclusions. Avazmohammadi and Castaneda [9] examined the particulate composites in which the inclusions with elliptical cross-sections are randomly distributed in the soft matrix. In particular, the homogenization approach and the loss of strong ellipticity analysis are used to identify the instability. Li et al. [83] observed the domain formation and pattern transition in soft particulate composites and demonstrated that the buckling pattern could be tuned by adjusting the initial geometry parameters. Goshkoderia et al. [53] examined the elastic instability in magnetoactive elastomer (MAE) composites with periodically distributed particles. They revealed that the new instability-induced pattern could be formed in the soft MAE composites subjected to the magnetic field and these newly formed patterns are determined by the magnitude of the applied magnetic field. Through the Bloch-Floquet analysis, Chen et al. [28] examined the elastic instability in soft particulate composites un-

der large deformations and extensively studied the buckling pattern with different geometric parameters.

1.1.2 Instability in viscoelastic soft composites

The strong dissipation effect was previously regarded as an adverse effect and thus should be avoided [13]. In recent decades, however, dissipation in mechanical instabilities attracted more attention because the interplay between instabilities and viscoelasticity and the spatial patterning of viscoelastic properties offers opportunities to create metamaterials with rate-dependent behavior [39]. For example, Alur and Meaud [3] investigated the mechanical behavior of the non-dilute viscoelastic laminates undergoing finite deformation. They found that the effective stiffness and damping properties can be adjusted by tuning the pre-strain. Slesarenko and Rudykh [131] demonstrated the tunability of the instability-induced pattern in viscoelastic laminates by using different applied strain rates. Che et al. [26] showed that the snaping sequence of the viscoelastic architected materials could be adjusted by temperature. Che et al. [27] further investigated the snap-through instabilities in the 3D printed viscoelastic metastructure and observed that the metastructure was temporarily bistable after a critical time which can be tuned by the temperature before relaxing to the undeformed state. Dykstra et al. [38] explored the snap-through response of viscoelastic metamaterials in experiments and found that the mechanical instability will be significantly affected beyond a certain strain rate. A soft compliant mechanism model was used to qualitatively capture the experimental behavior. They found that the high rate-sensitivity originates in the nonlinear and inhomogeneous deformation rate. Gomez et al. [52] proposed a truss model to capture the dynamics of the snap-through instability in the presence of viscoelasticity. They showed two types of possible snap-through: (i) the truss immediately snaps

back or (ii) pseudo-bistability (the truss will creep slowly first before acceleratingly snapping back). They also found that inertial effects need to be taken into consideration to accurately capture the pseudo-bistability. Janbaz et al. [71] introduced a viscoelastic bi-beam structure and showed that the bi-beam could be used to design lattice metamaterials with switchable auxetic behaviors and negative viscoelasticity. Urbach and Efrati [140] provided a theoretical framework to quantitatively study the delayed instability in the viscoelastic shells and found that the incompressible viscoelastic system will not lose stability if it is abruptly brought from the rest state to the locally stable state despite the existence of the stress relaxation. Bossart et al. [22] introduced an oligomodal metamaterial with switchable Poisson's ratio due to the existence of viscoelasticity. Glaesener et al. [51] provided a theoretical-numerical-experimental study for truss-based metamaterial and demonstrated that a viscoelastic beam approach calibrated by the tensile test of the individual strut specimen can well capture the response of the truss lattice metamaterial.

1.2 Outline of this dissertation

In Chapter 2, we provide the theoretical and modeling background. We overview nonlinear mechanics, hyperelastic and visco-hyperelastic models. The numerical details, including geometric structure, material models and boundary conditions, are also included.

In Chapter 3, we study the nonlinear viscoelasticity of soft photocured polymers typically used in Digital Light Processing (DLP) 3D printing. A continuum thermodynamics framework is used to capture the dependence of viscoelasticity of the photocured polymer on the light intensity used in the 3D printing process.

In Chapter 4, we focus on the instabilities in the visco-hyperelastic laminates under in-plane deformation. In particular, we present a theoretical method and numerical simulations

to study rate-dependent instability behavior. We further investigate the pattern transformation in the load-and-hold deformation state and the dependence of the dynamic mechanical properties on the cyclic loading frequency and pre-strain. In addition, the experiments are also carried out on the 3D printed soft laminate composites to validate the numerical method.

Chapter 5 investigates the role of viscoelasticity in the critical strain and wavelength onset of buckling in particulate composites subjected to in-plane deformation with a constant strain rate through simulations. In particular, we employ the single and multiple-branch visco-hyperelastic models. In addition, we perform experiments on the 3D-printed soft particulate composites to verify the numerical analysis.

Chapter 6 further explores the interaction between instability and viscoelasticity in soft particulate composites. In particular, we investigate the rate-dependent dynamic mechanical properties, negative stiffness of post-buckling response, and the energy absorption undergoing large deformation.

Finally, Chapter 7 concludes the dissertation and provides prospective research.

CHAPTER 2

THEORETICAL AND MODELING BACKGROUND

2.1 Nonlinear mechanics

A material point of a continuum solid in the reference configuration Ω_0 can be identified with its position vector $\boldsymbol{X}$. After deformation, $\boldsymbol{X}$ will be mapped into the current configuration Ω at the current time t with the corresponding position vector $\boldsymbol{x}$ (see Fig. 2.1) as

$$\boldsymbol{x} = \boldsymbol{\chi}(\boldsymbol{X}, t), \boldsymbol{X} \in \Omega_0 \tag{2.1}$$

Accordingly, the deformation gradient tensor is defined as

$$\mathbf{F} = \text{Grad } \boldsymbol{\chi}(\boldsymbol{X}, t) = \frac{\partial \boldsymbol{x}}{\partial \boldsymbol{X}} \tag{2.2}$$

where Grad is the gradient operation with respect to $\boldsymbol{X}$. The determinant of the deformation gradient tensor $J = \det \mathbf{F} > 0$ represents the volume ratio between the current and reference configuration. Let $\boldsymbol{\chi}_{\text{t}}$ denote the history of the motion χ up to time t as

$$\boldsymbol{\chi}_t (\boldsymbol{X}, s) = \boldsymbol{\chi} (\boldsymbol{X}, t - s) , 0 \leq s \leq t \tag{2.3}$$

In general, the Cauchy stress $\boldsymbol{\sigma}$ of a particle in the continuum body is determined by the history of motion $\boldsymbol{\chi}$ [43, 115, 139, 166], symbolically,

$$\boldsymbol{\sigma} = \mathbf{F} (\boldsymbol{\chi}_t (\boldsymbol{X}, s) ; \boldsymbol{X}, t) , s \geq 0 \tag{2.4}$$

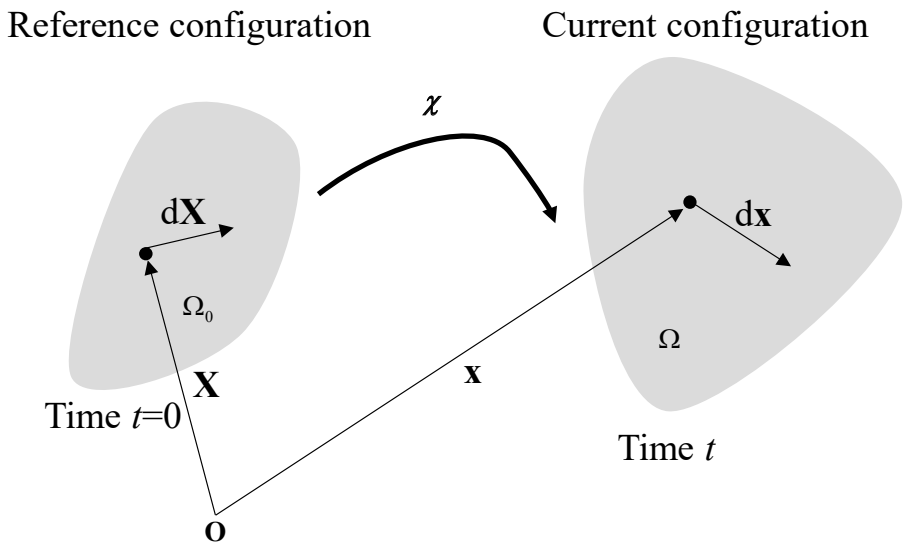

Figure 2.1: Configuration and motion of a continuum body.

where $\mathcal{F}$ is a constitutive functional with respect to $\boldsymbol{\chi}_{\mathrm{t}}(\boldsymbol{X}, s)$. Note that since χ_{t} is the possible motion history for Ω_0 as a whole, $\mathcal{F}$ is not restricted to $\boldsymbol{X}$ although it explicitly depends on $\boldsymbol{X}$. The history of motion of all particles in Ω_0 will contribute to the stress at a specific particle in Ω_0 at the current time t. For simple material, in which the stress at a particle is determined by the cumulative history of the deformation gradient at that particle [115], the general constitutive equation 2.4 can be simplified as

$$\boldsymbol{\sigma}=\mathbf{F}\left(\mathrm{Grad}\,\boldsymbol{\chi}_t\left(\boldsymbol{X}, s\right); \boldsymbol{X}, t\right), s \geq 0 \tag{2.5}$$

The corresponding first Piola-Kirchoff ($\mathbf{P}$) and second Piola-Kirchoff ($\mathbf{S}$) stress tensors are related to the Cauchy stress through

$$\mathbf{P} = J\boldsymbol{\sigma}\mathbf{F}^{-T} \text{and } \mathbf{S} = J\mathbf{F}^{-1}\boldsymbol{\sigma}\mathbf{F}^{-T} \tag{2.6}$$

, respectively. In the reference configuration, the equation of motion (absence of body forces) is written as

$$\mathrm{Div}\mathbf{P} = \rho_0 \frac{D^2\chi}{Dt^2} \tag{2.7}$$

where Div denotes the divergence operator in the reference configuration. $D()/Dt$ is the material time derivative operator and ρ_0 is the initial mass density of the material. In the quasi-statically loading condition, Eq. 2.7 modifies to

$$\mathrm{Div}\mathbf{P} = 0 \tag{2.8}$$

In the following subsection, we introduce two specific cases of simple material: hyperelastic and visco-hyperelastic material.

2.2 Constitutive models

2.2.1 Hyperelastic model

For hyperelastic material, the mechanical behavior can be described by a strain energy density function (SEDF) W_H, and the second Piola-Kirchoff stress $\mathbf{S}_H$ can be obtained by

$$\mathbf{S}_H = 2\frac{\partial W_H}{\partial \mathbf{C}}, \tag{2.9}$$

where $\mathbf{C} = \mathbf{F}^T\mathbf{F}$ is the right Cauchy-Green deformation tensor. For incompressible hyperelastic material ($J = 1$), Eq. 2.9 is rewritten as

$$\mathbf{S}_H = 2\frac{\partial W_H}{\partial \mathbf{C}} - p\mathbf{C}^{-1} \tag{2.10}$$

where p is an unknown Lagrange multiplier. The SEDF of an isotropic hyperelastic material can be expressed in terms of the invariants of the right Cauchy-Green tensor as $W_H = W_H(I_1, I_2, I_3)$, where,

$$I_1 = tr\mathbf{C}, \quad I_2 = \frac{1}{2}\left[(tr\mathbf{C})^2 - tr\mathbf{C}^2\right], \quad I_3 = \det\mathbf{C} = J^2 \tag{2.11}$$

For incompressible hyperelastic material, $I_3 = 1$. The SEDF of the homogeneous incompressible material described by the neo-Hookean model is

$$W_H = \frac{\mu_H}{2}(I_1 - 3) \tag{2.12}$$

where μ_H is the initial shear modulus. Substituting Eq. 2.12 into 2.10, the second Piola-Kirchoff stress is shown to be

$$\mathbf{S}_H = \mu_H\mathbf{I} + p\mathbf{C}^{-1} \tag{2.13}$$

where $\mathbf{I}$ is the identity tensor.

2.2.2 Visco-hyperelastic model

Soft materials show strong nonlinear viscoelasticity [25, 102, 150], so their mechanical properties can be tuned by temperature and applied strain rate. Deriving an accurate model which can predict the mechanical responses of the soft materials is vital to designing the structure with desired functionalities.

In this section, we review the general theory of thermodynamics for visco-hyperelastic theory [111, 123]. Any thermodynamic process should satisfy the second law of thermody-

namics. In continuum mechanics, it is written as Clausius-Duhem inequality [123]

$$\mathbf{S} : \frac{1}{2}\dot{\mathbf{C}} - \dot{W} \geq 0 \tag{2.14}$$

The elastic SEDF can be denoted as

$$W = W\left(\mathbf{C}, \xi_1, \cdots, \xi_M\right) \tag{2.15}$$

where $\xi_\alpha \, (\alpha = 1, \cdots, M)$ are the internal variables, substituting Eq. 2.15 into Eq. 2.14, we have

$$\left(\mathbf{S} - 2\frac{\partial W}{\partial \mathbf{C}}\right) : \frac{1}{2}\dot{\mathbf{C}} - \sum_{\alpha=1}^{M} \frac{\partial W}{\partial \xi_\alpha} \cdot \dot{\xi}_\alpha \geq 0 \tag{2.16}$$

From Eq. 2.16, we have

$$\mathbf{S} = 2\frac{\partial W}{\partial \mathbf{C}} \tag{2.17}$$

$$-\sum_{\alpha=1}^{M} \frac{\partial W}{\partial \xi_\alpha} : \dot{\xi}_\alpha \geq 0 \tag{2.18}$$

To determine the internal variables, M set of internal evolution equations should be given as

$$\dot{\xi}_\alpha = \xi_\alpha \left(\mathbf{C}, \xi_1, \xi_2, \cdots \xi_M\right) \tag{2.19}$$

Eqs. 2.17, 2.18 and 2.19 are fundamental equations for the dissipation processes. The viscoelastic process is also known as a dissipation process, so it should satisfy these equations. Therefore, the critical problem for formulating a thermodynamically-based model is to choose a reasonable SEDF W, internal variables ξ_α, and their evolution equations. There are no general expressions for visco-hyperelastic models. A constitutive equation would be considered reasonable if it is based on mechanism images and experimental data and satisfies

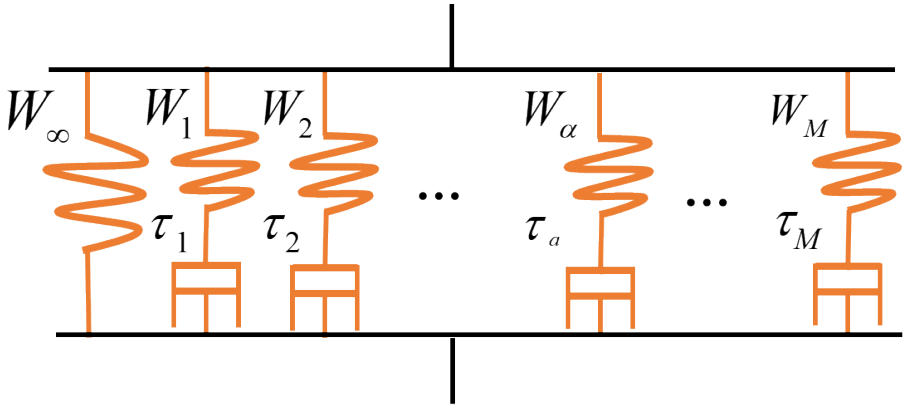

Figure 2.2: The rheological representation of the generalized Maxwell model.

Eq. 2.18 [134]. In the following, we introduce one specific visco-hyperelastic framework from Holzapfel [64].

Here, we introduce a visco-hyperelastic model [64] based on the rheological representation of the generalized Maxwell model (schematically illustrated in Fig. 2.2. The corresponding SEDF W_V is

$$W_V = W_\infty + \sum_{\alpha=1}^{M} W_\alpha \tag{2.20}$$

where W_∞ characterize the equilibrium state as $t \to \infty$, $W_\alpha = \beta_\alpha W_\infty$ represents the SEDF characterizing the non-equilibrium response; this corresponds to the non-linear spring in α^{th} branch; here, β_α is the strain-energy factor that can be used to characterize the value of the instantaneous shear modulus of the α^{th} branch [64]. The second Piola-Kirchoff stress $\mathbf{S}_\mathrm{V}$ is

$$\mathbf{S}_V = 2\frac{\partial W_V}{\partial \mathbf{C}} = \mathbf{S}_\infty + \sum_{\alpha=1}^{M} \mathbf{Q}_\alpha \tag{2.21}$$

where $\mathbf{S}_\infty$ is the equilibrium stress, $\mathbf{Q}_\alpha$ is the non-equilibrium stress of the α^{th} branch. The

equilibrium stress $\mathbf{S_\infty}$ and non-equilibrium stress $\mathbf{Q}_\alpha$ are

$$\mathbf{S}_\infty = 2\frac{\partial W_\infty}{\partial \mathbf{C}} - p_\infty \mathbf{C}^{-1} \tag{2.22}$$

and

$$\dot{\mathbf{Q}}_\alpha + \frac{\mathbf{Q}_\alpha}{\tau_\alpha} = \beta_\alpha \mathrm{Dev}(\dot{\mathbf{S}}_\infty) \tag{2.23}$$

where p_∞ is an unknown Lagrange multiplier, $\dot{()}$ is time derivative operator and $\mathrm{Dev}() = ()-1/3\left[() : \mathbf{C}\right]\mathbf{C}^{-1}$ is the deviatoric operator. The SEDF of the homogeneous material whose equilibrium (W_∞) and instantaneous (W_α) response are described by the neo-Hookean model is

$$W_V = \frac{\mu_\infty}{2}\left(I_1 - 3\right) + \sum_{\alpha=1}^{M} \frac{\mu_\alpha}{2}\left(I_1 - 3\right) \tag{2.24}$$

where μ_∞ is the initial shear modulus of equilibrium response, $\mu_\alpha = \beta_\alpha \mu_\infty$ is the initial instantaneous shear modulus of the α^{th} branch. Accordingly, the initial shear modulus of the instantaneous response can be defined as $\mu_0 = \mu_\infty(1 + \sum_\alpha \beta_\alpha)$. The second Piola-Kirchoff stress of the visco-hyperelastic model in Eq. 2.21 is calculated as

$$\mathbf{S}_V\left(t\right) = \mu_\infty \mathbf{I} + p_\infty \mathbf{C}^{-1} + \sum_{\alpha=1}^{M} \int_0^t \mu_\alpha \exp\left(\frac{-(t-\tau)}{\tau_\alpha}\right) \overset{\bullet}{\left[\mathbf{I} - \frac{\mathbf{I} : \mathbf{C}\left(\tau\right)}{3}\mathbf{C}\left(\tau\right)^{-1}\right]} d\tau \tag{2.25}$$

2.3 Numerical simulation

To investigate the buckling behavior of visco-hyperelastic composites under large deformation, we implement the finite element analysis (FEA) using a commercial software package COMSOL. All the numerical results in the following chapter are employed without consideration of the inertial effect for exclusively discussing the effect of viscoelasticity. Additionally,

the incompressible material is selected in all our simulations. In particular, when the incompressible hyperelastic materials are adopted in COMSOL, the SEDF consists of the isochoric part [30] as

$$W = W\left(\overline{I}_1, \overline{I}_2\right) \tag{2.26}$$

where $\overline{I}_1 = \mathrm{Tr}\overline{\mathbf{C}}$ and $\overline{I}_2 = \frac{1}{2}\left(\overline{I}_1^2 - \mathrm{Tr}\overline{\mathbf{C}}^{\mathbf{2}}\right)$ and $\overline{\mathbf{C}} = J^{-2/3}\mathbf{C}$ is the isochoric right Cauchy-Green tensor. In COMSOL, a weak constraint ($\int_\Omega \left((1-J)\,dp_w + \left(p_w + \frac{1}{3}\mathrm{Tr}\,(s)\right)dJ\right)dV = 0$) is built-in to ensure the incompressibility condition ($J = 1$). Here p_w is an auxiliary variable.

In this thesis, we focus on the laminate and particulate composites undergoing in-plane compression. Accordingly, the average deformation gradient tensor is

$$\overline{\mathbf{F}} = \overline{\lambda}\mathbf{e}_1 \otimes \mathbf{e}_1 + \overline{\lambda}^{-1}\mathbf{e}_2 \otimes \mathbf{e}_2 + \mathbf{e}_3 \otimes \mathbf{e}_3 \tag{2.27}$$

where $\overline{\lambda}\,(t) = 1 - \varepsilon(t)$ is the applied macroscopic stretch ratio in the compression direction, $\varepsilon\,(t)$ is the applied compression strain. Here and hereafter, the superscript (m) represents the soft matrix for both laminate and particulate composites. The superscript (f) denotes the stiff fiber of laminates and superscript (i) represents the stiff inclusions of particulate composites (see Fig. 2.3 and Fig. 2.4).

2.3.1 Numerical modeling details for laminate composite

We consider a periodic laminate composite consisting of two phases, as schematically illustrated in Fig. 2.3 (a), w_0 and d_0 are initial width of the unit cell and fiber, respectively. The volume fractions of the fiber and matrix are expressed as $v^{(f)}$ and $v^{(m)} = 1 - v^{(f)}$, respectively. The mechanical response of the matrix and fiber material is described by the

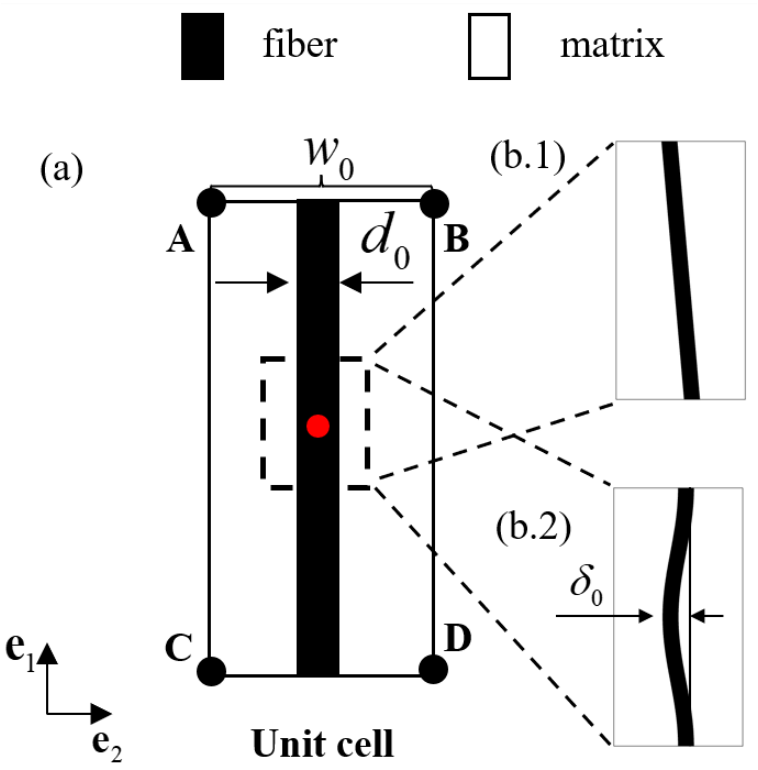

Figure 2.3: (a) Schematically illustration of the unit cell of the laminate composite. (b) two types the geometric imperfections: (b.1) angle imperfections and (b.2) Cosine function-shaped imperfections.

incompressible neo-Hookean and the visco-hyperelastic model [64], respectively (as introduced in Sec. 2.2.2).

We implement the numerical analysis through finite element simulations in COMSOL 5.6. We apply the in-plane compression through the following periodic boundary conditions imposed on the unit cell:

$$\boldsymbol{U}_{top} - \boldsymbol{U}_{down} = \left(\overline{\mathbf{F}} - \mathbf{I}\right)\left(\boldsymbol{X}|_{top} - \boldsymbol{X}|_{down}\right) \tag{2.28}$$

$$\boldsymbol{U}_{right} - \boldsymbol{U}_{left} = \left(\overline{\mathbf{F}} - \mathbf{I}\right)\left(\boldsymbol{X}|_{right} - \boldsymbol{X}|_{left}\right) \tag{2.29}$$

where $\boldsymbol{U} = [U_1, U_2]^T$ are the displacement vector, U_1 and U_2 are the displacement components in $\mathbf{e_1}$ and $\mathbf{e_2}$, respectively. The subscript "top", "down", "left" and "right" denote the edges of AB, CD, AC and BD, respectively, and the "A", "B", "C" and "D" are illustrated in Fig. 2.3 (a). To prevent rigid body motion, we impose a constraint as $\mathbf{U}|_{\text{center}}=\mathbf{0}$. Here the subscript "center" is the center point of the unit cell (see the red point in Fig. 2.3 (a)). For discussion, we set the contrast in the initial equilibrium shear modulus of fiber and matrix as $\mu_\infty^{(f)}/\mu^{(m)} = 15$ and the contrast in initial instantaneous shear modulus of fiber and matrix as $\mu_0^{(f)}/\mu^{(m)} = 100$.

2.3.2 Numerical modeling details for particulate composite

Consider the soft particulate composite consisting of stiff circular inclusions embedded in the soft matrix, as illustrated in Fig. 2.4. The geometry of the structure is defined through the periodicity aspect ratio $\eta = w_0/h_0$ and inclusion spacing ratio $\xi = d_0/h_0$; where w_0 and h_0 are the width and height of the primitive unit cell, and d_0 is the diameter of the inclusions. The stiff inclusions are modeled by the incompressible neo-Hookean and the soft

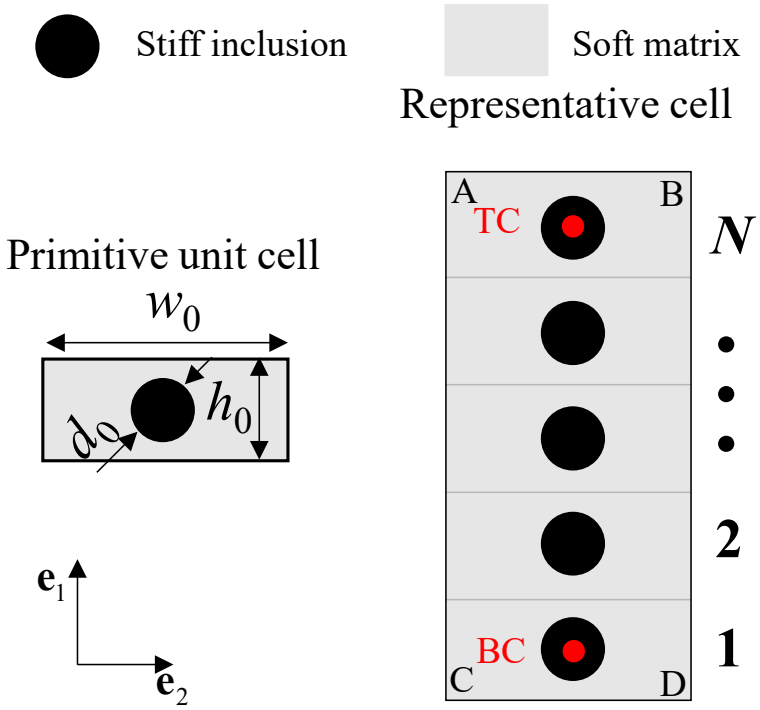

Figure 2.4: Schematic illustration of the primitive unit and representative cell.

matrix is characterized by the visco-hyperelastic model [64] (as introduced in Sec. 2.2.2).

To analyze the instabilities in the soft composite, we carry out the numerical analysis through finite element simulations in COMSOL 5.6. We use a single-column inclusion system with a large enough number of inclusions ($N = 40$, if not specified otherwise) along $\mathbf{e_1}$-direction in the representative cell (see Fig. 2.4). We apply the in-plane unidirectional compression by imposing the periodic displacement boundary conditions on the representative cell as

$$\boldsymbol{U}_{AB} - \boldsymbol{U}_{CD} = \left(\overline{\mathbf{F}} - \mathbf{I}\right)\left(\boldsymbol{X}|_{AB} - \boldsymbol{X}|_{CD}\right) \tag{2.30}$$

$$\boldsymbol{U}_{BD} - \boldsymbol{U}_{AC} = \left(\overline{\mathbf{F}} - \mathbf{I}\right)\left(\boldsymbol{X}|_{BD} - \boldsymbol{X}|_{AC}\right) \tag{2.31}$$

where the subscript AB, CD, AC, and BD denote the interior node on the top, bottom, left, and right edges of the representative cell, respectively, and the "A", "B", "C", and "D" are illustrated in Fig. 2.4. To prevent rigid body motion, we impose a constraint as $\boldsymbol{U}|_{\mathrm{TC}}+\boldsymbol{U}|_{\mathrm{BC}}= 0$. Here the subscript "TC" and "BC" are the center points of inclusions on the top and bottom of the representative cell, respectively (see the red points in Fig. 2.4).

In chapter 5, we focus on composite configuration with weak interactions between columns of inclusions; accordingly, we assign a high unit cell aspect ratio, $w_0/h_0 = 32$. The inclusion spacing ratio is set as $\xi = 0.8$. The initial equilibrium shear modulus of the matrix $\mu_\infty^{(m)} = 0.1614$ MPa. The contrast between the initial shear modulus of stiff inclusions and the initial equilibrium shear modulus of the matrix is set as $\mu^{(i)}/\mu_\infty^{(m)} = 10^5$. Thus, the deformation in stiff inclusions is negligible in comparison with that of the soft matrix.

In chapter 6, we focus on composites configuration with non-negligible and weak interactions between columns of inclusions. In particular, we assign $\eta = 3.0$ and $\xi = 0.8$ and $\eta = 32$ and $\xi = 0.8$ for the composites with non-negligible and weak interactions between columns of

inclusions, respectively. For convenience, we name the composites with $\eta = 3.0$ and $\xi = 0.8$ as well as $\eta = 32$ and $\xi = 0.8$ as composite one and two, respectively. Our numerical analysis is performed with the material parameters from Alur and Meaud [3]. Specifically, the initial shear modulus of the stiff inclusions is set as $\mu^{(i)} = 5.49{\times}10^4$ MPa, resembling the steel. The soft matrix material resembles polyurethane which is simulated by the single-branch visco-hyperelastic model with $\mu_\infty^{(m)} = 1.115$ MPa, $\beta = 134.5$ and $\tau = 0.15$s. The contrast between the initial shear modulus of stiff inclusions and the initial equilibrium shear modulus of the matrix is around $5{\times}10^4$, so the deformation in stiff inclusions is negligible in comparison with that of the soft matrix. The stress-strain response of the particulate composite undergoing the compression with a constant strain rate was reported to be identical for a given Weissenberg number $Wi = \dot{\varepsilon}\tau$ [153]. Therefore, in chapter 5 and 6, we may use Wi as the dimensionless strain rate if not specified otherwise.

CHAPTER 3

MECHANICAL CHARACTERIZATION AND CONSTITUTIVE MODELING OF VISCO-HYPERELASTICITY OF PHOTOCURED POLYMERS

Yuhai Xiang, Cody Schilling, Nitesh Arora, AJ Boydston, Stephan Rudykh

*(*Reprinted from Additive Manufacturing of Elsevier)*

In this chapter, we study the nonlinear behavior of soft photocured polymers typically used in 3D-printing. We perform experimental testing of 3D-printed samples cured at various controlled light intensities. The experimental data show the dependence of the material elasticity and rate-sensitivity on the curing light intensity. To elucidate these relations, we develop a physically-based visco-hyperelastic model in the continuum thermodynamics framework. In our model, the macroscopic viscoelastic behavior is bridged to the microscopic molecular chain scale. This approach allows us to express the material constants in terms of polymer chain physical parameters. We consider different physical mechanisms governing hyperelasticity and rate-dependent behaviors. The hyperelastic behavior is dictated by the crosslinked network; whereas, the viscous part originates in the free and dangling chains. Based on our experimental data, we illustrate the ability of the new constitutive model to accurately describe the influence of the light intensity on photocured polymer viscoelasticity.

3.1 Introduction

3D-printing of soft materials has been employed in numerous areas such as tissue engineering [36, 61], drug delivery devices [112, 145] and soft robots [75]. The technology

expands the design space by allowing the fabrication of complicated geometries, composition, and tailored properties [119, 168]. A promising soft material fabrication method – Digital Light Processing (DLP) 3D printing – utilizes photo-polymerization in the layer by layer curing process [4, 10, 74, 76, 129]. The produced materials typically exhibit rich material nonlinearity and rate-sensitivity [21, 133, 148], and their properties are highly dependent on the printing process parameters. Motivated by providing the understanding of the soft digital material behavior, in this chapter, we develop a new physically-based visco-hyperelastic model in the continuum thermodynamics framework. Previously, Zarrelli et al. [164] – utilizing the Kohlrausch-Williams-Watts (KWW) equations [130] – developed a constitutive model that describes the dynamic relaxation modulus during curing. The model incorporates the four coupled phenomena: photophysics, photochemistry, chemomechanical coupling, and mechanical deformation. A general thermodynamic framework has been proposed by Long et al. [94]; the model allows simulating different mechanisms-induced photochemical-thermal-mechanical coupling behavior of photo-active polymer undergoing finite deformation. Recently, Zhao et al. [167] investigated the effects of oxygen on the stress relaxation and bending actuation of the light-activated polymers. Most recently, Wu et al. [149] studied the evolution of material properties during the photo-polymerization. They applied a phase evolution model to characterize the coupling between mechanical and chemical reactions during the curing process; the developed "multibranch" viscoelastic model captures the nonlinear viscoelastic behavior of the photocured polymer. Sain et al. [128] proposed a thermal-chemo-mechanically coupled constitutive framework for cured glassy thermoset polymer. Yu et al. [160] presented a theoretical framework to consider the effects of light intensity, light wavelength, and photoinitiator concentration on self-healing behavior. The shape distortion of the structures created by DLP 3D printing technology is investigated by

using photo-polymerization reaction kinetics and Euler–Bernoulli beam theory [148].

Photo-polymerized polymers frequently exhibit strong nonlinear viscoelastic behavior under finite deformation [113, 149]. To model finite deformation viscoelastic behaviors, the so-called phenomenological and physically-based constitutive models are used. While here, we mostly focus on the physically-based models, interested readers are referred to the works by [66, 73, 77, 98, 99, 109, 147], among many others.

Physically-based viscoelastic models can be formulated by consideration of the viscous-related micromechanisms, such as the reptational motion of molecular chains [14, 40, 170], re-orientation and stretch relaxation of chain segments [92], as well as the breaking and reattaching of temporary crosslinks [93]. These models, however, include fitting parameters that are not directly related to the underlying physical mechanisms. For the thermodynamically consistent models [92, 109, 170], appropriate restrictions are imposed on their fitting parameters. On the other hand, physically-based models can be developed by directly characterizing the viscous related microscopic structures so that all material constants can be connected to the microscopic quantities [89, 91, 135, 141, 142, 152]. For a more detailed discussion of the topic, the readers are referred to the recent review by Xiang et al. [151]. We note that there is a large number of viscoelastic models incorporating finite-deformation, while only a few models consider the specifics of the viscoelasticity in the photocured polymer [67, 68, 128, 149].

In this chapter, we develop a finite-deformation physically-based visco-hyperelastic constitutive model for photocured polymers. Our finite-deformation viscoelastic model incorporates the rate-dependent behaviors by considering the microstructure of the polymer, including the crosslinked network, and free and dangling chains (schematically shown in Fig. 3.3). Moreover, the light intensity-dependent crosslinked network and the nonlinear viscosity of

free and dangling chains are also included in the model.

We further apply our model for a particular material – 2-hydroxyethyl acrylate (HEA) – that we produce through DLP 3D-printing with the light intensity-controlled viscoelasticity. We illustrate the ability of the constitutive model to accurately describe the experimentally observed influence of the light intensity on the photocured polymer viscoelasticity.

The chapter is organized as follows: Section 3.2 describes the procedures for 3D printing and mechanical characterization. Section 3.3 presents the continuum thermodynamic framework for viscoelastic materials, the formulation for light intensity-dependent nonlinear viscosity of the free and dangling chains, and the expressions for light intensity-dependent Helmholtz free energy density. Section 3.4 includes the modeling and experimental results, followed by discussions and concluding remarks.

3.2 Material fabrication and experiments

The sample fabrication procedure is schematically shown in Fig. 3.1. The typical DLP printing system comprises a light projector, moving stage, and a resin vat [4, 76], Wu et al. [149]. The geometric features of the specimens are digitally sliced into a series of images. Then, these images are sequentially projected by the DLP projector (Optoma HD27 1080p DLP Home projector) into the liquid resin vat to cure it into a solid layer [129]. Thenceforth, the stage moves vertically to a new position, and the next layer is cured. The layer by layer process is repeated until the final structure of the specimen is completely printed (depicted in Fig. 3.1 (b)).

Specimen preparation. Typical vat photopolymerization resins consist of monomers, crosslinkers, and photoinitiators. Our resin consisted of 2-hydroxyethyl acrylate (HEA) as the monomer and Irgacure 819 as the photoinitiator (0.25 wt % with respect to the

monomer mass). No additional crosslinker was added as commercial HEA contains several single weight percent of diacrylate impurities [129]. Different levels of the visible (or white) light intensity I controlled through gray scale adjustments in Microsoft PowerPoint were used to produce specimens with varying mechanical properties, while keeping other environmental variables fixed, including the temperature, the layer exposure time (20 seconds), the initial concentration of uncured liquid resin and the thickness of each projected layer (100 µm). In particular, we printed the specimens at four different visible (or white) light intensities, namely, $I = 12.56 \text{ klx} \pm 2.58 \text{ klx}$, $15.10 \text{ klx} \pm 4.28 \text{ klx}$, $21.53 \text{ klx} \pm 3.37 \text{ klx}$, and $27.17 \text{ klx} \pm 3.23 \text{ klx}$. Average intensities were measured using an Extech HD450 Light meter at the vat interface. All printed parts were rinsed with acetone to remove excess monomer and post-cured by irradiating with white light for a minimum of 12 hours. For each light intensity, at least 6 dog bone specimens are printed, each comprised of 30 total cured layers. The dimensions of the specimen are provided in Fig. A.1 in Appendix A.1. To ensure the specimen can be tightly fixed by the screw grippers, two holes at the ends of the specimen (Fig. 3.2).

Experimental setup. The mechanical testing was performed in the experimental apparatus schematically shown in Fig. 3.2. The linear actuators and a load cell with Labview are used to synchronize displacement measurement, imaging, and force data collection (Landauer et al. [79]. The optical system for recording data (consisting of a control computer, camera, a long-distance microscopy lens, polarizing filters, and LED light panels) are installed on a vibration-isolated table, and the collected data is analyzed by the DIC. The DIC camera is aligned to the uniform deformation area in the middle of the specimen. A secondary camera is used to detect possible abnormal deformation conditions. For the uniaxial tensile test, screw-actuated grips are attached to the base of the load frame and the load cell, and the

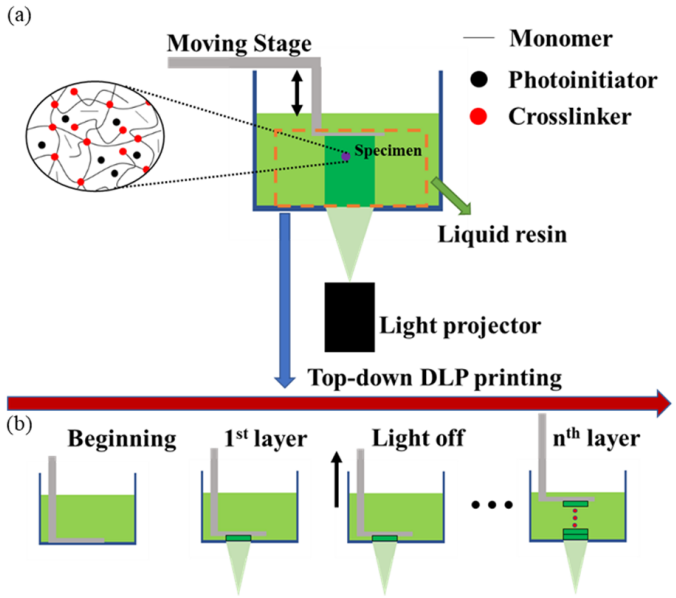

Figure 3.1: Schematic representation of the DLP 3D printing process. 3D geometric images of specimens are sliced into pictures and are projected sequentially into a liquid resin to cure the layer-by-layer structure. (a) The DLP 3D printing system, (b) the procedures for top-down DLP printing.

specimen is tightly gripped with the griping-force exerted by the screw grips.

The uniaxial tensile tests were performed at three different strain rates $\dot{\varepsilon} = 10^{-3}\ s^{-1}$, $10^{-2}\ s^{-1}$, and $10^{-1}\ s^{-1}$; the tests were repeated at least twice for each strain rate. The nominal stress P is calculated as $\mathrm{P} = \mathrm{F}/A_0$, where F is the force data collected by the load cell, and A_0 is the original area of the cross-section of the DIC measured region. The results show that all the HEA specimens tested here exhibit strong viscoelastic behavior.

3.3 Theory

3.3.1 The continuum thermodynamics

Consider a polymer molecular network composed of the crosslinked network, free and dangling chains, as schematically shown in Fig. 3.3. The free chains are not chemically bound

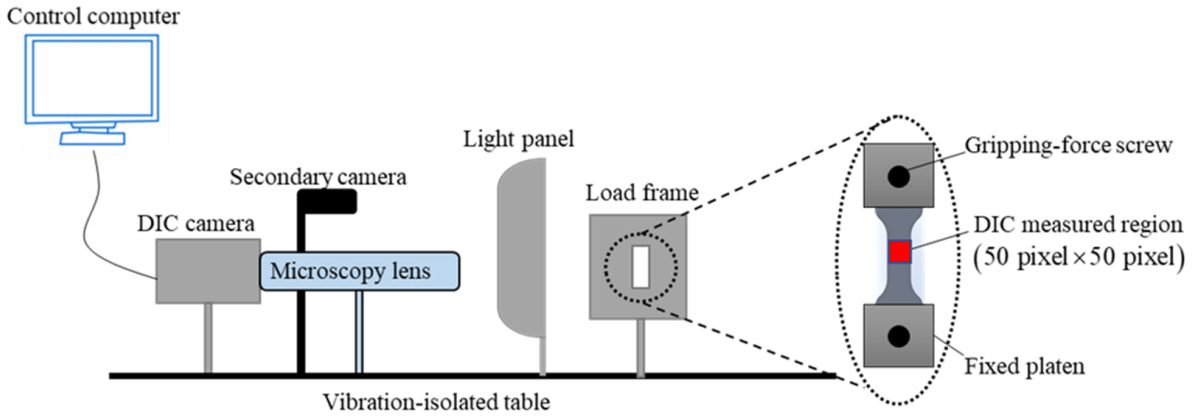

Figure 3.2: Schematic of the top and side views of the experimental setup and the front view of the fixtures for the uniaxial tensile test.

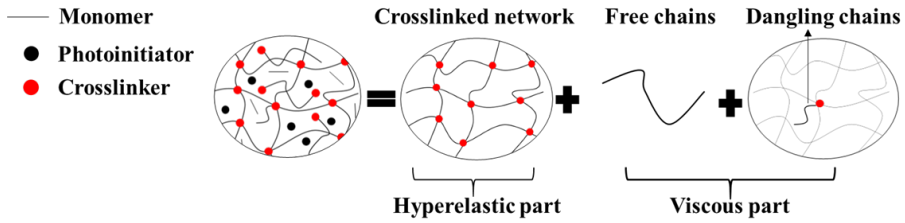

Figure 3.3: The schematic diagram of the molecular chain network: the molecular network composed of the crosslinked network, free chains, and dangling chains.

to the crosslinked network, while the dangling chains are connected to the crosslinked network by a single end-link. Whereas the crosslinked network is attributed to the purely hyperelastic mechanical response, the free and dangling chains are responsible for the viscous response. The corresponding macroscopic mechanical behavior of the polymer can be described by the rheological model, as shown in Fig. 3.4. The branches A, B_1 and B_2represent the crosslinked network, free chains, and dangling chains, respectively.

The deformation acting on all the branches is identical (see, Fig. 3.4); hence, the applied deformation gradient tensor $\mathbf{F}$ is equal to the deformation gradient tensor of the branch A, B_1 and B_2, i.e., $\mathbf{F}=\mathbf{F}_A=\mathbf{F}_{B_1}=\mathbf{F}_{B_2}$. For branches B_1 and B_2, the deformation gradient tensor

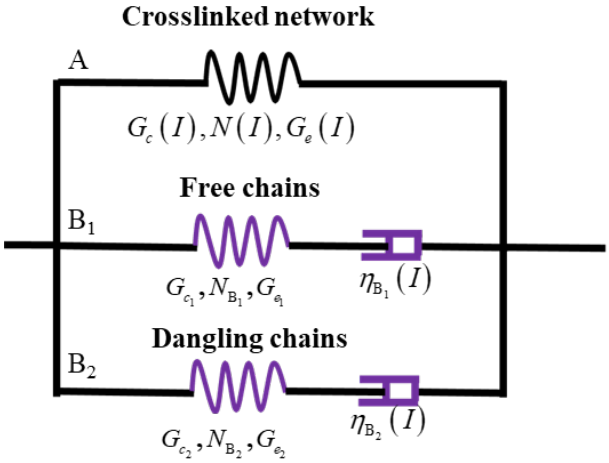

Figure 3.4: The macroscopic rheological representation of viscoelasticity.

can be multiplicatively decomposed into the elastic part and viscous part as $\mathbf{F}_{\mathrm{B_n}}=\mathbf{F}^{\mathrm{e}}_{\mathrm{B_n}}\mathbf{F}^{\mathrm{i}}_{\mathrm{B_n}}$ (n=1,2). $\mathbf{F}^{\mathrm{e}}_{\mathrm{B_n}}$ and $\mathbf{F}^{\mathrm{i}}_{\mathrm{B_n}}$ denote the deformation gradient tensor of the spring and dashpot, respectively.

Next, the continuum thermodynamics is introduced to capture the viscoelastic behavior [66, 123, 170]. The Helmholtz free energy density functions of the springs are $W_{\mathrm{A}}(\mathbf{F}_{\mathrm{A}})$, $W_{\mathrm{B_1}}\left(\mathbf{F}^{\mathrm{e}}_{\mathrm{B_1}}\right)$ and $W_{\mathrm{B_2}}\left(\mathbf{F}^{\mathrm{e}}_{\mathrm{B_2}}\right)$, so that the total Helmholtz free energy density of the printed material is

$$W\left(\mathbf{F}_{\mathrm{A}},\mathbf{F}^{\mathrm{e}}_{\mathrm{B_1}},\mathbf{F}^{\mathrm{e}}_{\mathrm{B_2}}\right)=W_{\mathrm{A}}(\mathbf{F}_{\mathrm{A}})+W_{\mathrm{B_1}}\left(\mathbf{F}^{\mathrm{e}}_{\mathrm{B_1}}\right)+W_{\mathrm{B_2}}\left(\mathbf{F}^{\mathrm{e}}_{\mathrm{B_2}}\right) \tag{3.1}$$

The total Cauchy stress is given by

$$\mathbf{T}=J^{-1}\frac{\partial W}{\partial \mathbf{F}}\mathbf{F}^{T}=\mathbf{T}_{\mathrm{A}}+\sum_{\mathrm{n=1}}^{2}\mathbf{T}_{\mathrm{B_n}} \tag{3.2}$$

where $J=\det(\mathbf{F})$,

$$\mathbf{T}_{\mathrm{A}}=J^{-1}\frac{\partial W_{\mathrm{A}}(\mathbf{F}_{\mathrm{A}})}{\partial \mathbf{F}}\mathbf{F}^{\mathrm{T}} \tag{3.3}$$

and

$$\mathbf{T}_{\mathrm{B_n}}=J^{-1}\frac{\partial W_{\mathrm{B_n}}\left(\mathbf{F}^{\mathrm{e}}_{\mathrm{B_n}}\right)}{\partial \mathbf{F}}\mathbf{F}^{\mathrm{T}} \tag{3.4}$$

According to the Clausius-Planck inequality [65]

$$\mathbf{P}:\dot{\mathbf{F}}-\dot{W}\geq 0 \tag{3.5}$$

where, $\mathbf{P}$ is the total first Piola–Kirchhoff stress, we have

$$\left(\mathbf{P}-\frac{\partial W}{\partial \mathbf{F}}\right):\dot{\mathbf{F}}-\sum_{\mathrm{n}=1}^{2}\frac{\partial W}{\partial\left(\mathbf{F}_{\mathrm{B_n}}\mathrm{H}^{\mathrm{i}}_{\mathrm{B_n}}\right)}:\frac{\partial\left(\mathbf{F}_{\mathrm{B_n}}\mathrm{H}^{\mathrm{i}}_{\mathrm{B_n}}\right)}{\partial \mathrm{F}^{\mathrm{i}}_{\mathrm{B_n}}}:\dot{\mathbf{F}}^{\mathrm{i}}_{\mathrm{B_n}}\geq 0 \tag{3.6}$$

where $\mathbf{H}^{\mathrm{i}}_{\mathrm{B_n}}$ is the inverse of $\mathbf{F}^{\mathrm{i}}_{\mathrm{B_n}}$. According to the Eq. 3.6, we have

$$\mathbf{P}=\frac{\partial W}{\partial \mathbf{F}} \tag{3.7}$$

and

$$\sum_{\mathrm{n}=1}^{2}\frac{\partial W}{\partial \mathbf{F}^{\mathrm{e}}_{\mathrm{B_n}}}:\left(\mathbf{F}^{\mathrm{e}}_{\mathrm{B_n}}\dot{\mathbf{F}}^{\mathrm{i}}_{\mathrm{B_n}}\mathbf{H}^{\mathrm{i}}_{\mathrm{B_n}}\right)\geq 0 \tag{3.8}$$

Introducing the inelastic Cauchy stress

$$\mathbf{T}^{NEQ}_{\mathrm{B_n}}=\frac{1}{\det\left(\mathbf{F}^{\mathrm{e}}_{\mathrm{B_n}}\right)}\frac{\partial W_{\mathrm{B_n}}\left(\mathbf{F}^{\mathrm{e}}_{\mathrm{B_n}}\right)}{\partial \mathbf{F}^{\mathrm{e}}_{\mathrm{B_n}}}\left(\mathbf{F}^{\mathrm{e}}_{\mathrm{B_n}}\right)^{\mathrm{T}} \tag{3.9}$$

The Eq. 3.8 can be rewritten as

$$\mathbf{T}^{NEQ}_{\mathrm{B_n}}:\mathbf{L}^{\mathrm{i}}_{\mathrm{B_n}}\geq 0 \tag{3.10}$$

where $\mathbf{L}^{\mathrm{i}}_{\mathrm{B_n}}$=$\mathbf{F}^{\mathrm{e}}_{\mathrm{B_n}}\dot{\mathbf{F}}^{\mathrm{i}}_{\mathrm{B_n}}\mathbf{H}^{\mathrm{i}}_{\mathrm{B_n}}\mathbf{H}^{\mathrm{e}}_{\mathrm{B_n}}$, $\mathbf{H}^{\mathrm{e}}_{\mathrm{B_n}}$ is the inverse of $\mathbf{F}^{\mathrm{e}}_{\mathrm{B_n}}$. Due to the symmetry of $\mathbf{T}^{NEQ}_{\mathrm{B_n}}$, the Eq. 3.10 is rewritten as

$$\mathbf{T}^{NEQ}_{\mathrm{B_n}}:\mathbf{D}^{\mathrm{i}}_{\mathrm{B_n}} \geq 0 \tag{3.11}$$

where $\mathbf{D}^{\mathrm{i}}_{\mathrm{B_n}}=\left(\mathbf{L}^{\mathrm{i}}_{\mathrm{B_n}}+\left(\mathbf{L}^{\mathrm{i}}_{\mathrm{B_n}}\right)^{\mathrm{T}}\right)/2$. To satisfy the Eq. 3.11, a kinetic evolution equation is given by Hong [66] as

$$\mathbf{D}^{\mathrm{i}}_{\mathrm{B_n}}=\mathbf{M}:\mathbf{T}^{NEQ}_{\mathrm{B_n}} \tag{3.12}$$

where $\mathbf{M}$ is a positive-definite fourth-order tensor, defined as [123]

$$\mathbf{M}=\frac{1}{2\eta_{\mathrm{B_n}}}\left(\mathbb{I}-\frac{1}{3}\mathbf{I}\otimes\mathbf{I}\right) \tag{3.13}$$

where $\mathbb{I}=\delta_{ik}\delta_{jl}\boldsymbol{e}_i\otimes\boldsymbol{e}_j\otimes\boldsymbol{e}_k\otimes\boldsymbol{e}_l$ is the fourth-order symmetric identity tensor, $\mathbf{I}$ is the second-order identity tensor. $\eta_{\mathrm{B_n}}$ is the viscosity of dashpot $\mathrm{B_n}$ (for Eq. 3.13, the incompressibility of the elastomer is assumed). The procedure for determining the nonlinear viscosity coefficients $\eta_{\mathrm{B_n}}$ is described next; to this end, the viscosity of free chains are determined based on Wu et al. [149] and Zhou et al. [170], and the viscosity of dangling chains is calculated based on Wu et al. [149] and Pearson and Helfand [118].

3.3.2 The nonlinear viscosity of free chains and dangling chains

Free chains

For describing the free chain contribution, we follow the work of Wu et al. [149]. We assume that the relative viscosity η of melt changes as a function of the degree of conversion of monomers as $\eta = exp\left(c_{\mathrm{p}}p\right)$ during curing; here, p is the degree of conversion of monomers, and c_{p} is a relative viscosity coefficient related to p. Since a higher light intensity can

transform more monomers for a given projection time, a higher degree of conversion is produced. Therefore, we assume that the relative viscosity η is the function of light intensity I, namely, $\eta = exp\,(c_{\mathrm{I}} I)$, where c_{I} is a relative viscosity coefficient related to light intensity. Thus, for the dashpot in the branch B_1 (free chains), the nonlinear viscosity is assumed to be dependent on the light intensity I as

$$\eta_{\mathrm{B}_1}(I, \mathbf{F}) = \eta_{\mathrm{B}_1}^{I_0}(\mathbf{F}) \exp(\, c_1 I) \tag{3.14}$$

where c_1 is a relative viscosity coefficient for the dashpot B_1. The relationship between viscosity and deformation is formulated by Zhou et al. [170] as

$$\eta_{\mathrm{B}_1}^{I_0}(\mathbf{F}) = \frac{\eta_{\mathrm{B}_1}^{0}}{\alpha(\mathbf{F})^2} \tag{3.15}$$

where $\eta_{\mathrm{B}_1}^{0}$ is the initial viscosity of the dashpot $\mathbf{B}_1$ in the reference state, and,

$$\alpha(\mathbf{F}) = \frac{\int |\mathbf{F}\cdot\mathbf{R}|^2 f_0(\boldsymbol{R})\, d^3\boldsymbol{R}}{\left\langle \boldsymbol{R}_{\mathrm{ee}}^2 \right\rangle_0 \int \frac{|\mathbf{F}\cdot\boldsymbol{u}_0|}{4\pi} d^2\boldsymbol{u}_0} \tag{3.16}$$

$$\left\langle \boldsymbol{R}_{\mathrm{ee}}^2 \right\rangle_0 = \int |\mathbf{F}\cdot\boldsymbol{R}|^2 f_0(\boldsymbol{R})\, d^3\boldsymbol{R} \tag{3.17}$$

where f_0 is the statistical distribution function of end to end vector $\boldsymbol{R}$ of the free chains (or dangling chains) in the reference state and the Gaussian distribution is usually adopted [89, 170]; $\boldsymbol{u}_0$ is the initial unit tangent vector of free chains (or dangling chains).

Dangling chains

Now, we build upon the formulation above Eq. 3.14, and introduce the contribution of the dangling chains into the material viscoelastic response. For the dashpot in the branch B_2(dangling chains), similar to the dashpot B_1, the nonlinear viscosity is also formulated as

$$\eta_{B_2}(I,\mathbf{F}) = \eta_{B_2}^{I_0}(\mathbf{F}) \exp(\ c_2 I) \tag{3.18}$$

where c_2 is a relative viscosity coefficient for the dashpot B_2 and $\eta_{B_2}(\mathbf{F})$ can be expressed by Pearson and Helfand [118] (more details are provided in Appendix A.2) as

$$\eta_{B_2}^{I_0}(\mathbf{F}) = \eta_{B_2}^{0} \alpha(\mathbf{F}) \exp\left(\frac{\Gamma'}{\alpha(\mathbf{F})^2}\right) \text{ and } \quad \Gamma' = \frac{12}{25}\Gamma \tag{3.19}$$

where $\eta_{B_2}^{0} = \left(\frac{4\Gamma}{5}\right)^{-1/2} \frac{b^2 n_{B_2} N_{B_2} \sqrt{\pi} \zeta_{B_2}}{5\left(v'\right)^{5/2}}$ is a parameter related to the viscosity of dashpot B_2,$v' = 0.6$ and ζ_{B_2} is the friction constant for dangling chains, $\Gamma = \frac{N_{B_2} b^2}{d_2^2}$is a tube-related geometric factor (the arm of dangling chains retract in a confining tube to relax stress), in which b is the length of the Kuhn monomers, and d_2 is the tube diameter of the dangling chains in the reference state.

3.3.3 Helmholtz free energy density

Crosslinked network

The Helmholtz free energy density $W_A$of the crosslinked network can be expressed as [154]

$$W_A = G_c(I) N(I) \ln\left(\frac{3N(I) + \frac{1}{2} I_1(\mathbf{C})}{3N(I) - I_1(\mathbf{C})}\right) + G_e(I) \sum_{i=1,2,3} \frac{1}{\lambda_i} \tag{3.20}$$

where $\mathbf{C}=\mathbf{F}^{\mathbf{T}}\mathbf{F}$ is the right Cauchy-Green tensor of spring A (crosslinked network) and $I_1(\mathbf{C})$ is the first invariant of $\mathbf{C}$; λ_i denotes the principal stretches of spring A. $G_c(I)$ and $G_e(I)$ are the initial elastic moduli corresponding to the responses of the crosslinked network and the entanglement of the spring A, respectively. The moduli are expressed as

$$G_c(I)=n(I)\,k_BT \quad \text{and} \quad G_e(I)=\alpha n(I)\,N(I)\,k_BT\frac{b^2}{3(d_0(I))^2} \tag{3.21}$$

where n is the numbers of chains per volume (or chain number density) in the crosslinked network; N is the number of the Kuhn monomers per chain in the crosslinked network; k_B and T are the Boltzmann constant and Kelvin temperature; α is a tube-related geometric factor; d_0 is the tube diameter of the crosslinked network in the reference state, and it is proportional to $\left(nNb^2\right)^{-1}$ [44], so that the entanglement modulus can be expressed as

$$G_e=\frac{\alpha k_BTb^4(nN)^2}{3\beta} \tag{3.22}$$

where β is a proportionality factor. The chain density n and number of the Kuhn monomers per chain N of the crosslinked network depends on light intensity. Here, we assume that

$$n=n_0\exp\left(\alpha_1\left(I-I_g\right)\right)\ ;\ N=N_0\exp\left(-\alpha_2\left(I-I_g\right)\right)\ ;\ (\alpha_1>0,\alpha_2>0) \tag{3.23}$$

where I_g is the critical light intensity for the gel point[1]; α_1 and α_2 are light intensity-dependent factors for chain number density and the number of Kuhn monomers per chain of the crosslinked network, respectively; n_0 and N_0 are the number density of chains and the number of the Kuhn monomers per chain in the crosslinked network at the gel point; nN is the number density of monomers of the crosslinked network, and nN increases with an

1. *The materials are in a liquid state if the light intensities is lower than* I_g

increase in light intensity, thus, $\alpha_1 - \alpha_2 > 0$. Substituting Eq. 3.23 into 3.21, we have

$$G_c\left(I\right) = G_c^0 \exp\left(\alpha_1\left(I - I_g\right)\right) \text{ and } G_e\left(I\right) = G_e^0 \exp\left(2\left(\alpha_1 - \alpha_2\right)\left(I - I_g\right)\right) \tag{3.24}$$

where

$$G_c^0 = n_0 k_B T \qquad \text{and} \qquad G_e^0 = \frac{\alpha k_B T b^4 (n_0 N_0)^2}{3\beta} \tag{3.25}$$

are the initial moduli corresponding to the response of the crosslinked network and the entanglement of the spring A (crosslinked network) at the gel point, respectively. Thus, Eq. 3.20 can be rewritten as

$$\begin{aligned} W_{\mathrm{A}} = G_c^0 \exp\left(\alpha_1\left(I - I_g\right)\right) N_0 \exp\left(-\alpha_2\left(I - I_g\right)\right) \ln\left(\frac{3N_0 \exp\left(-\alpha_2\left(I - I_g\right)\right) + \frac{1}{2} I_1(\mathbf{C})}{3N_0 \exp\left(-\alpha_2\left(I - I_g\right)\right) - I_1(\mathbf{C})}\right) \\ + G_e^0 \exp\left(3\left(\alpha_1 - \alpha_2\right)\left(I - I_g\right)\right) \sum_{i=1,2,3} \frac{1}{\lambda_i} \end{aligned} \tag{3.26}$$

We note that the adopted microstructure-based model for the specific Helmholtz free energy density functions for the crosslinked network W_{A} [154] will also be used for describing free and dangling chains $W_{\mathrm{B_n}}$. The model allows us to connect the material parameters to viscous-related microscopic quantities and this characteristic can be further utilized to capture the light intensity-dependent viscoelastic behavior. In addition, the entanglements between chains play an important role in the mechanical behavior of the crosslinked network, free and dangling chains. We note that alternative models, such as 3-chain model [70], Arruda–Boyce model [8], or Gent model [49], could also be used. On the other hand, the utilized model accounts for the entanglement mechanism, thus, potentially improving the accuracy for describing the mechanical behavior of polymer chains.

Free and dangling chains

The hyperelasticity of the free and dangling chains (of the springs in branches B_n (n = 1, 2)) is assumed to be governed by a similar Helmholtz free energy density W_{B_n}, namely,

$$W_{B_n}=G_{c_n}N_{B_n}\ln\left(\frac{3N_{B_n}+\frac{1}{2}I_1\left(\mathbf{C}^e_{B_n}\right)}{3N_{B_n}-I_1\left(\mathbf{C}^e_{B_n}\right)}\right)+G_{e_n}\sum_{i=1,2,3}\frac{1}{\lambda^e_{i_n}}. \tag{3.27}$$

Here, G_{c_n} and G_{e_n} are initial modulus of the *temporary* crosslinked network and the entanglement modulus of the spring in branches B_n, respectively; N_{B_n} is the number of the Kuhn monomers in a single free or dangling chain; $\mathbf{C}^e_{B_n}$ is the right Cauchy-Green tensor of spring B_n; $I_1\left(C^e_{B_n}\right)$ is the first invariant of $C^e_{B_n}$, and $\lambda^e_{i_n}$ represents the principal stretches of spring B_n. Here, we assume the material parameters for spring B_n (temporary hyperelastic properties of free chains and dangling chains) to be independent of light intensity. At certain projection times, high light intensities can transform a more significant number of free chains or dangling chains into the crosslinked network, as compared to low light intensities; however, simultaneously producing more free and dangling chains. Therefore, overall, the light intensities have much more effect on the crosslinked network in comparison to the insignificant effect on the free and dangling chains.

Thus, the combination of Eqs. 3.2-3.4, 3.12-3.14, 3.18, 3.26, and 3.27, comprises the visco-hyperelastic constitutive model for photocured polymers.

3.4 Results

Here, we specify the visco-hyperelastic model for the uniaxial loading and apply the analysis to the experimental data on the 3D-printed HEA polymer material. For the uniaxial tensile deformation, the gradient deformation tensor of the spring A and B_n(shown in

Fig. 3.4) can be expressed as

$$\mathbf{F}=\mathbf{F}_{\mathrm{A}}=\mathbf{F}_{\mathrm{B_n}}=\mathbf{F}^{\mathrm{e}}_{\mathrm{B_n}}\mathbf{F}^{\mathrm{i}}_{\mathrm{B_n}}=\lambda\mathbf{e}_1\otimes\mathbf{e}_1+\lambda^{-1/2}\left(\mathbf{I}-\mathbf{e}_1\otimes\mathbf{e}_1\right) \tag{3.28}$$

$$\mathbf{F}^{\mathrm{e}}_{\mathrm{B_n}}=\lambda^{\mathrm{e}}_{\mathrm{B_n}}\mathbf{e}_1\otimes\mathbf{e}_1+\left(\lambda^{\mathrm{e}}_{\mathrm{B_n}}\right)^{-1/2}\left(\mathbf{I}-\mathbf{e}_1\otimes\mathbf{e}_1\right);\ \mathbf{F}^{\mathrm{i}}_{\mathrm{B_n}}=\lambda^{\mathrm{i}}_{\mathrm{B_n}}\mathbf{e}_1\otimes\mathbf{e}_1+\left(\lambda^{\mathrm{i}}_{\mathrm{B_n}}\right)^{-1/2}\left(\mathbf{I}-\mathbf{e}_1\otimes\mathbf{e}_1\right) \tag{3.29}$$

where λ represents the uniaxial stretch ratio, the superscripts "e" and "i" indicate the elastic (spring) and inelastic (viscous dashpot), respectively. Here, we consider the materials to be incompressible.

Substituting Eq. 3.28 and 3.29 into Eq.3.26 and 3.27 using Eq. 3.2, the total nominal stress is determined as

$$\begin{aligned}
P_{11}(t) = {} & G_c^0 \exp\left(\alpha_1\left(I-I_g\right)\right)\frac{\left(\lambda(t)-\lambda^{-2}(t)\right)}{\left(1-\frac{I_1(t)}{3N_0\exp(-\alpha_2(I-I_g))}\right)\left(1+\frac{1}{2}\frac{I_1(t)}{3N_0\exp(-\alpha_2(I-I_g))}\right)} \\
& + G_e^0\exp\left(3\left(\alpha_1-\alpha_2\right)\left(I-I_g\right)\right)\left(\lambda^{-1/2}(t)-\lambda^{-2}(t)\right) \\
& + \sum_{n=1}^{2} G_{c_{\mathrm{n}}}\frac{\left(\lambda(t)\left(\lambda^{i}_{\mathrm{B_n}}(t)\right)^{-2}-\lambda^{-2}(t)\lambda^{i}_{\mathrm{B_n}}(t)\right)}{\left(1-\frac{I_{1e}(t)}{3N_{\mathrm{B_n}}}\right)\left(1+\frac{1I_{1e}(t)}{23N_{\mathrm{B_n}}}\right)} + G_{e_n}\left(\left(\lambda(t)\lambda^{i}_{\mathrm{B_n}}(t)\right)^{-1/2}-\lambda^{-2}(t)\lambda^{i}_{\mathrm{B_n}}(t)\right)
\end{aligned} \tag{3.30}$$

where $I_1 = \lambda^2 + 2\lambda^{-1}$. The first term of Eq. 3.30 represents the stress of branch A (crosslinked network) and the second term denotes the stress from branches B_1 and B_2 (free chains and dangling chains). Then, substituting the expressions of the viscosity of free chains 3.14 and dangling chains 3.18 into the kinetic evolution equation 3.12, we have

$$\frac{d\lambda^i_{\mathrm{B}_1}(t)}{dt} = \frac{\lambda^i_{\mathrm{B}_1}(t)\alpha(\mathbf{F})^2}{3\eta^0_{\mathrm{B}_1}\exp\left(c_1 I\right)}\left[G_{c_1}\frac{\left(\lambda^2(t)\left(\lambda^i_{\mathrm{B}_1}(t)\right)^{-2} - \lambda^{-1}(t)\lambda^i_{\mathrm{B}_1}(t)\right)}{\left(1-\frac{I^{\mathrm{B}_1(t)}_{1e}}{3N_{\mathrm{B}_1}}\right)\left(1+\frac{1I^{\mathrm{B}_1(t)}_{1e}}{23N_{\mathrm{B}_1}}\right)} + G_{e_1}\left(\lambda^{1/2}(t)\left(\lambda^i_{\mathrm{B}_1}(t)\right)^{-1/2} - \lambda^{-1}(t)\lambda^i_{\mathrm{B}_1}(t)\right)\right] \tag{3.31}$$

$$\frac{d\lambda^i_{\mathrm{B}_2}(t)}{dt} = \frac{\lambda^i_{\mathrm{B}_2}(t)}{3\eta^0_{\mathrm{B}_2}\alpha(\mathbf{F})\exp\left(\frac{\Gamma'}{\alpha(\mathrm{F})^2}+c_2 I\right)}\left[G_{c_2}\frac{\left(\lambda^2(t)\left(\lambda^i_{\mathrm{B}_2}(t)\right)^{-2} - \lambda^{-1}(t)\lambda^i_{\mathrm{B}_2}(t)\right)}{\left(1-\frac{I^{\mathrm{B}_2}_1(t)}{3N_{\mathrm{B}_2}}\right)\left(1+\frac{1}{2}\frac{\mathrm{I}^{\mathrm{B}_2}_1(t)}{3N_{\mathrm{B}_2}}\right)} + G_{e_2}\left(\lambda^{1/2}(t)\left(\lambda^i_{\mathrm{B}_2}(t)\right)^{-1/2} - \lambda^{-1}(t)\lambda^i_{\mathrm{B}_2}(t)\right)\right] \tag{3.32}$$

where $I^{\mathrm{B_n}}_{1e} = \left(\lambda^e_{\mathrm{B_n}}\right)^2 + 2\left(\lambda^e_{\mathrm{B_n}}\right)^{-1} = \lambda^2\left(\lambda^i_{\mathrm{B_n}}\right)^{-2} + 2\lambda^{-1}\lambda^i_{\mathrm{B_n}}$ is the first invariant of the right Cauchy-Green tensor of spring B_n.

The material constants are determined as follows. First, we determine the time-independent material constants G^0_c, α_1, N_0, G^0_e, α and I_g by using the data at a low strain rate ($\dot{\varepsilon} = 10^{-3}\ s^{-1}$) in Section 3.4.1. Then, these material constants are used for determining the time-dependent material constants G_{c_1}, N_1, G_{e_1}, $\eta^0_{B_1}$, c_1, G_{c_2}, N_2, G_{e_2}, $\eta^0_{B_2}$, Γ' and c_2 by fitting the data with strain rates $10^{-2}\ s^{-1}$ and $10^{-1}\ s^{-1}$ (Section 3.4.2). We note that a proper initial guess of material constants is essential, and is based on the physical meaning of the material constants, thus, the parameters need to be positive, and, additionally, $\alpha_1 - \alpha_2 > 0$.

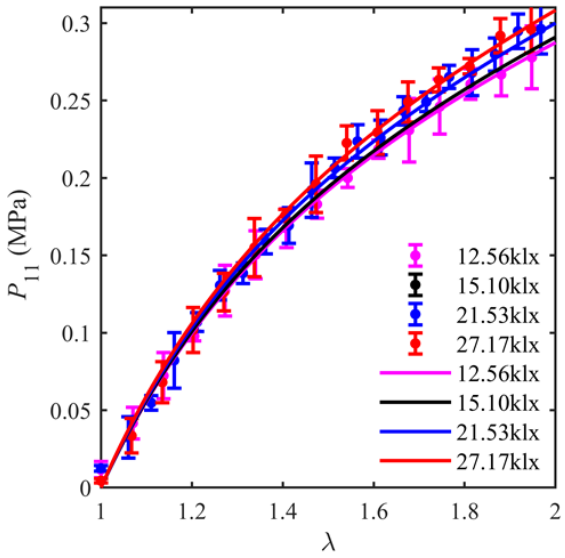

Figure 3.5: The model and experimental results for specimens with the strain rate $\dot{\varepsilon} = 10^{-3}$ s^{-1} *and different light intensities* (12.56klx, 15.10klx, 21.53klx *and* 27.17klx). *The circles and curves denote the experimental and modeling results, respectively.*

3.4.1 Material constants of the crosslinked network

Here we use the data of quasistatic deformation at a low strain rate ($\dot{\varepsilon} = 10^{-3}$ s^{-1}) to extract the material parameters of the hyperelastic part (crosslinked network). To this end, the first term in Eq. 3.30 is used. In Fig. 3.5, we show the comparison of experimental data (circular symbols) and simulation results (curves) for the specimens printed at the light intensities: $I = 12.56$ klx (magenta), 15.10 klx (black), 21.53 klx (blue), and 27.17 klx (red). As expected, the response becomes stiffer as the light intensity is increased. This is also captured by the hyperelastic material model based on the crosslinked network. The obtained material parameters are provided in Table 3.1.

Table 3.1: The material parameters of the hyperelastic (crosslinked network) part of specimens.

G_c^0(MPa)	α_1(1/x)	N_0	G_e^0(MPa)	α_2(1/lx)	I_g(lx)
0.1049	6.79×10^{-6}	1030	0.1940	6.76×10^{-6}	998

3.4.2 Material constants of the free and dangling chains

Once the material constants describing material hyperelasticity are obtained, we can evaluate the material parameters corresponding to the viscoelasticity (related to the free and dangling chains). In Fig. 3.6, we show the dependence of the nominal stress on the stretch ratio obtained from the uniaxial tests (triangular, square, and circles). In particular, the results are shown for the specimens prepared at light intensities $I = 12.56$ klx (Fig. 3.6 (a)), $I = 15.10$ klx (Fig. 3.6 (b)), $I = 21.53$ klx (Fig. 3.6 (c)), and $I = 27.17$ klx (Fig. 3.6 (d)); subjected to strain rates $\dot{\varepsilon} = 10^{-3}\ s^{-1}$ (red circles), $\dot{\varepsilon} = 10^{-2}\ s^{-1}$ (blue squares), and $\dot{\varepsilon} = 10^{-1}\ s^{-1}$ (magenta triangles). We use Eqs. 3.30-3.32 to simultaneously fit the experimental data for these specimens with strain rates ($10^{-2}\ s^{-1}$ and $10^{-1}\ s^{-1}$). The modeling results for the nominal stress-stretch curves are shown in Fig. 3.6. For completeness, the simulation results for strain rate $\dot{\varepsilon} = 10^{-3}\ s^{-1}$ are also presented. Clearly, the proposed model can accurately capture light intensity-dependent viscoelastic response. We note that this model feature comes at the cost of introducing additional material parameters, as compared to existing models; for example, Bergstrom and Boyce [14] model describes the material behavior with only 7 material parameters. On the other hand, our model enables us to capture the light intensity-dependent behavior (although, at the cost of introducing additional material parameters), which is a desirable feature for modeling DLP 3D-printed materials. The corresponding material parameters (for free and dangling chains) are provided in Table 3.2.

Utilizing the parameters listed in Table 3.1 and Table 3.2, we can compare the stress

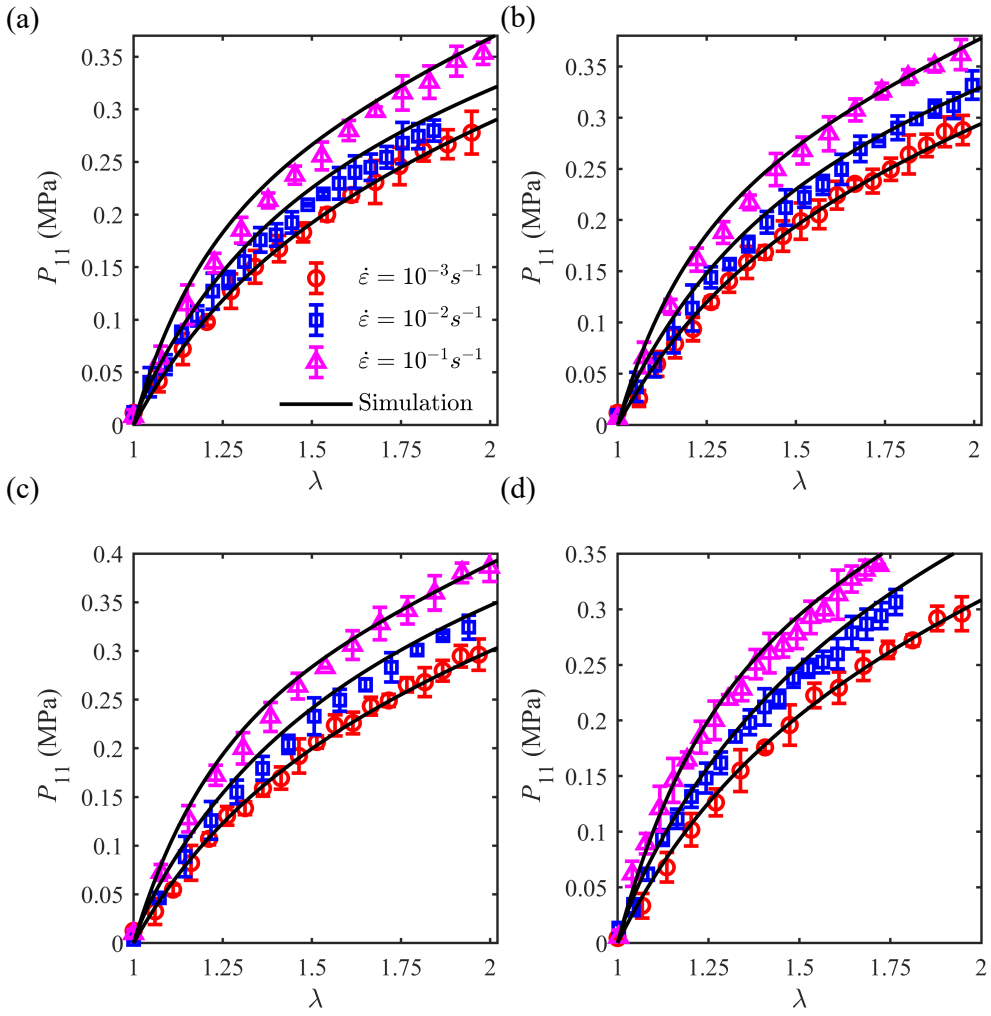

Figure 3.6: Comparison of modeling and experimental results for specimens subjected to strain rates $\dot{\varepsilon} = 10^{-3}$ s^{-1} *(red circles),* $\dot{\varepsilon} = 10^{-2}$ s^{-1} *(blue squares), and* $\dot{\varepsilon} = 10^{-1}$ s^{-1} *(magenta triangles) with projected light intensities (a)* $I = 12.56$klx; *(b)* $I = 15.10$klx; *(c)* $I = 21.53$klx *and (d)* $I = 27.17$ *klx.*

Table 3.2: The material parameters of the viscoelastic (free and dangling chains) part of specimens.

G_{c_1}(MPa)	N_1	G_{e_1}(MPa)	$\eta^0_{B_1}$(MPa · s)	c_1(1/lx)	G_{c_2}(MPa)	N_2	G_{e_2}(MPa)	$\eta^0_{B_2}$(MPa · s)	Γ'	c_2(1/x)
2.72×10^{-5}	861	0.2938	0.1553	3.11×10^{-5}	0.0456	764	3.1515	1.26	0.0022	7.99×10^{-5}

contributions from the crosslinked network, free and dangling chains, and analyze the dependence of nonlinear viscosity on the deformation and light intensity.

To analyze the stress contributions from the crosslinked network, free and dangling chains, we consider the example of the specimens prepared under light intensity $I = 12.56$ klx subjected to strain rates $\dot{\varepsilon} = 10^{-2}\ s^{-1}$ and $10^{-1}\ s^{-1}$ (the fitting parameters are listed in Table 3.1 and Table 3.2). In Fig. 3.7, we show the contribution from the hyperelastic (blue curve) and viscous (magenta curve) part to the total stress (black curve). On comparing Fig. 3.7 (a) and (b), one can observe that the stress from the viscous part increases with the increase in applied strain rate. Moreover, the contribution from the hyperelastic part is rate-independent for given light intensity.

To elucidate the dependence of viscous response on the light intensity, we consider the example of the specimens tested at the strain rate $\dot{\varepsilon} = 10^{-1}\ s^{-1}$. Fig. 3.8 (a) shows the viscous part of the stress for specimens prepared under light intensities $I = 12.56$ klx (magenta), 15.10 klx (black), 21.53 klx (blue), and 27.17 klx (red). Clearly, the viscous stress increases with an increase in light intensity. We also evaluate the contribution from the free chains (magenta circular symbols) and dangling chains (magenta square symbols) to the viscous stresses, separately, as shown in Fig. 3.8 (b). Here, the specimen prepared under light intensity $I = 12.56$ klx is used as an example. It indicates the importance of both free and dangling chains for accurate characterization of the viscous response. Interestingly, we also observe that the stress of free chains plays a more important role at smaller deformation levels. However, it relaxes much faster than the stress of dangling chains. This observation is in agreement with the fact that the relaxation time of dangling chains is much larger than that of free chains [55, 155]. Henceforth, the contribution from dangling chains is more significant than free chains under larger deformations.

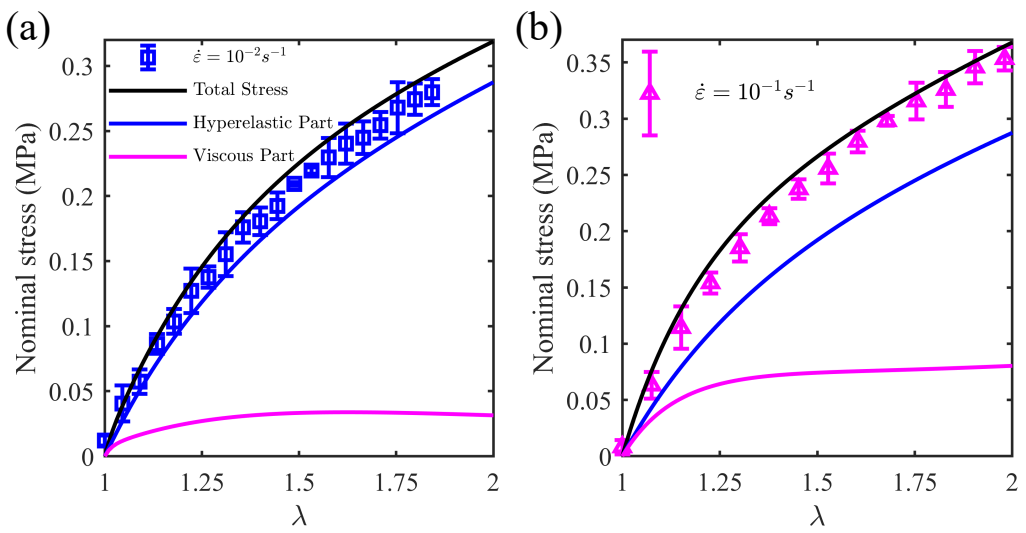

Figure 3.7: Comparison of stresses from the hyperelastic part (blue curve) and viscous part (magenta curve) under strain rates (a) $\dot{\varepsilon} = 10^{-2}$ s^{-1} and (b) $\dot{\varepsilon} = 10^{-1}s^{-1}$.

Fig. 3.9 shows the stress from free chains (circular symbols) and dangling chains (square symbols) of the specimens at four light intensities I = 12.56 klx (magenta), 15.10 klx (black), 21.53 klx (blue), and 27.17 klx (red). One can observe that the stresses from both the free and dangling chains increase with the increase in light intensity. Moreover, the contribution from free chains shows a higher sensitivity to change in light intensity than dangling chains.

Next, we study how the viscosity of the free and dangling chains evolve with deformation and light intensity. Using Eqs. 3.14-3.15, and Eqs. 3.18-3.19 together with the parameters in Table 3.1 and Table 3.2, in Fig. 3.10, we show the variation of nonlinear viscosity of these chains with deformation. We consider four different light intensities: I = 12.56 klx (magenta), 15.10 $k$lx (black), 21.53 klx (blue), and 27.17 klx (red). We observe that both the deformation and light intensity significantly affect the viscosity. In particular, the light intensity has a similar effect on the viscosity of both free and dangling chains. More specifically, the viscosity of these chains increases with the increase in light intensity. In contrast,

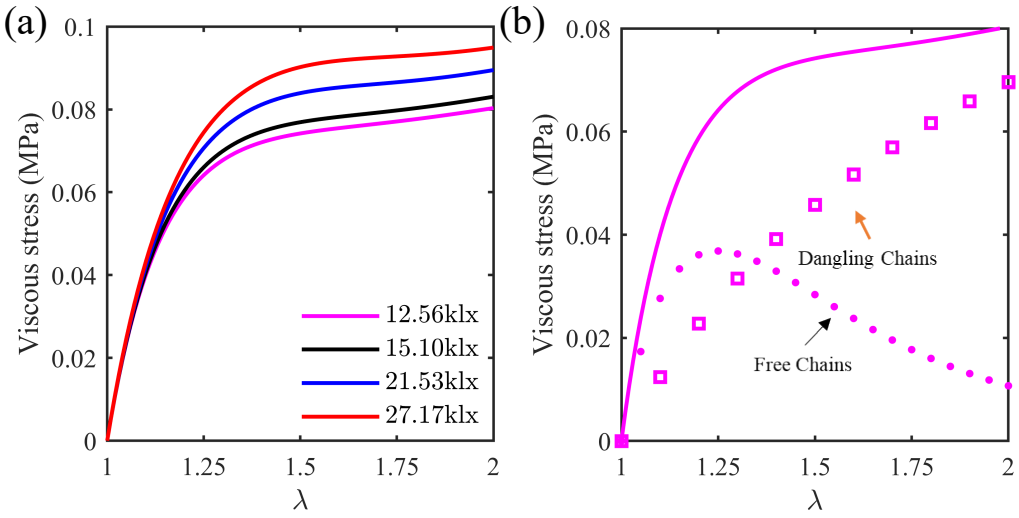

Figure 3.8: The viscous stresses of specimens tested at the strain rate $\dot{\varepsilon} = 10^{-1}\ \mathrm{s}^{-1}$. *(a) The specimens prepared under light intensities* $I = 12.56\mathrm{klx}, 15.10\mathrm{klx}, 21.53\mathrm{klx}$ *and* $27.17\mathrm{klx}$. *(b) The viscous stresses from free chains and dangling chains for the specimen with light intensity* $12.56\mathrm{klx}$.

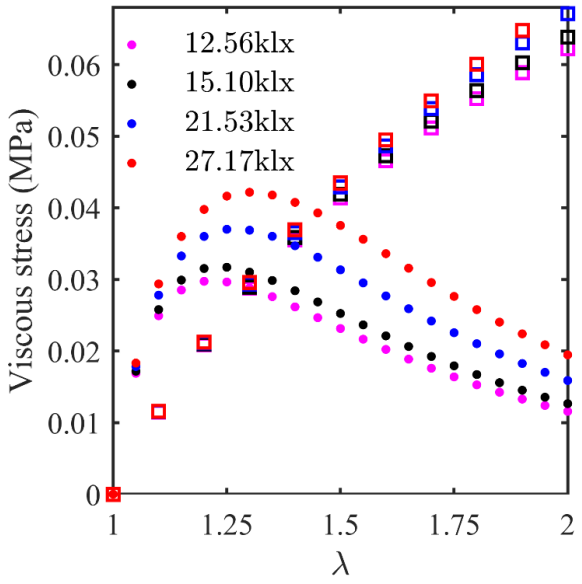

Figure 3.9: The stress from free chains and dangling chains; the circular and square symbols respectively represent the results for free chains and dangling chains.

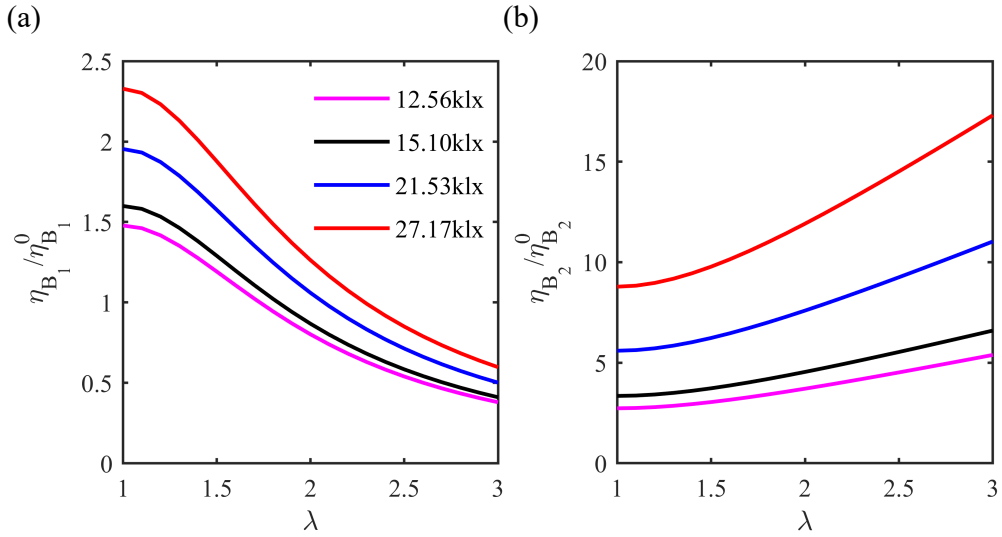

Figure 3.10: The dependence of the nonlinear viscosity of (a) free chains and (b) dangling chains on the deformation and light intensities.

the influence of deformation on the viscosity of free and dangling chains is opposite, i.e., the viscosity of free chain decreases, while that of the dangling chain increases with the increase in deformation.

We show the effect of the number of free chains on the mechanical response of the specimen in Fig. 3.11. We consider an example of the specimen prepared under light intensity $I = 27.17$ klx tested at the strain rate $\dot{\varepsilon} = 10^{-1}\ s^{-1}$. To illustrate the model predictions for the polymer behavior with an increased amount of free-chains, we show the results for (i) specimens with unchanged free chains (back curve), and (ii) with the doubled amount of free chains (red curve). We observe that free chains play a more significant role at smaller deformation levels, while the influence on the stress weakens at larger deformation levels. As expected, the viscoelastic stress contributed by free chains rapidly relaxes to a similar level as can be seen in Fig. 3.11 (b). The amounts of free chains can be adjusted by, for example, adding non-crosslinkable analogs into specimens, thus, allowing us to regulate the

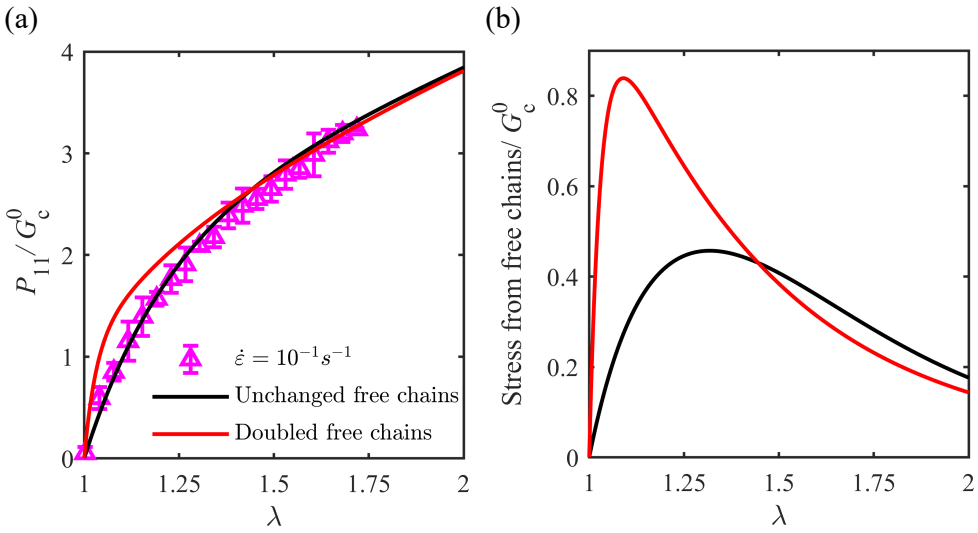

Figure 3.11: The stresses of specimens with projected light intensity I = 27.17klx tested at the strain rate $\dot{\varepsilon} = 10^{-1}s^{-1}$. (a) The total stress and (b) the stress from free chains of the free chains unchanged specimen (black curve) and free chains doubled specimen (red curve).

rate-dependent behavior of the printed specimen.

3.5 Concluding Remarks

In this chapter, we experimentally and theoretically investigate the curing light intensity-dependent viscoelastic behavior of HEA prepared by the DLP 3D-printing method. The HEA specimens are printed at different light intensities, otherwise with the same environment setting. The tensile tests are conducted on these specimens at various loading rates. The experimental results reveal the strong dependence of the viscoelasticity of HEA on the light intensity. To shed light on the dependence of the material properties of photocured polymers on curing light intensity, we develop a visco-hyperelastic model. The model is based on the continuum thermodynamics with the decomposition of the polymer microstructure response into hyperelastic and viscous parts. The hyperelastic and viscous parts are attributed to

the crosslinked network and the diffusion of free and dangling chains, respectively. The developed model is applied to characterize the rate-dependent behavior of the photocured HEA. The simulation results demonstrate the ability of this model to accurately characterize the light intensity-dependent viscoelastic response. In particular, the stresses from the crosslinked network, free chains, and dangling chains are compared, showing the necessity of simultaneously considering the contributions from free and dangling chains for accurately characterizing viscoelasticity. The evolution of viscosity with the deformation and light intensity is also presented to indicate the strong dependence of viscosity on the deformation and light intensity. The effect of the free chains on mechanical response is also discussed. Our model predicts that the free chains have a more significant effect on the mechanical response at smaller deformation levels, and their influence weakens at large strain levels. This behavior can be potentially realized in experiments by adding non-crosslinkable analogs into the specimen, thus increasing the free chain content. While the model is calibrated based on the experiment data of HEA, it can be used for a large variety of photocured polymers due to the similarity of the photopolymerization mechanism.

While the present study exclusively investigates the effect of projected light-intensity on the mechanical properties of photo-cured polymers, several other controllable factors influence the digital material behavior, for example, oxygen (through reacting with the radicals and making them inactive, or through inhibiting the photopolymerization reaction [167]), the layer thickness [81], exposure time [20], and the post-curing temperature [31]. Moreover, in multi-material 3D-printing [83, 86], depending on the characteristic microstructure size, and printing process, the mixing interphase zone can form. These interphases, while being mechanically invisible, may influence pattern formations in soft composites experiencing local buckling [5]. These factors present a rich research avenue towards the understanding of soft

3D-printed material behavior and its relation to the physical mechanism during 3D-printing.

CHAPTER 4

MICROSTRCURAL BUCKLING IN SOFT VISCO-HYPERELASTIC LAMINATES*

Yuhai Xiang, Qi Yao, Dean Chen, Jian Li, Stephan Rudykh

*(*Prepared for submission to a journal)*

We investigate the microstructural buckling phenomenon in visco-hyperelastic laminates under compressive loads. We determine the dependence of the critical strain and wavenumber on the loading strain rate. The numerical results are complemented with an analytical estimate predicting the dependence of the critical strain on the strain rate. We find that the critical strain is bound by the two limits corresponding to sufficiently fast and slow loading rates, and decreases with the increase in the strain rate, and the theoretical and numerical critical strain show good agreements. The critical wavenumber of the dilute laminates decreases with the increase in the strain rate. However, the critical wavenumber of the non-dilute laminates remains nearly zero with the change in strain rate. Then, the laminates under the "load-and-hold" regime are explored. We observe that the buckling pattern gradually disappears in the holding phase of the load-and-hold loading path. Next, we investigate the dependence of dynamic modulus and loss factor on cyclic loading frequency and pre-strain. We note that dynamic modulus and loss factor are slightly (or significantly) dependent on the pre-strain when the pre-strain is smaller (or larger) than the critical strain corresponding to quasi-static loading. Finally, we examine the instabilities in the 3D-printed laminates through experiments and simulations. The simulations show good agreement with the experimental critical strain of the 3D-printed laminates, demonstrating the capability of numerical simulation to capture the mechanical behavior of the visco-hyperelastic laminates.

4.1 Introduction

Soft composites with tunable microstructure under large deformation provide a avenue to achieve more novel properties such as auxetic properties [16, 86, 110], reconfigurable structure [156] and negative viscoelasticity [71]. Moreover, soft microstructured materials with elastic instabilities can be utilized to tune the wave propagation [15, 126].

The pioneering work Rosen [124] laid a foundation for understanding the elastic instabilities in laminate composites. He provided a theoretical expression for the buckling stress of linear elastic laminates. Parnes and Chiskis [116] further investigated the instabilities of linear elastic laminates. They found that dilute and non-dilute composites experience microscopic and macroscopic instability, respectively. In hyperelastic laminates, the instabilities can also develop at microscopic and macroscopic length scales [90]. The microscopic instability can be analyzed by employing Bloch-Floquet analysis [18, 50]. The onset of macroscopic instability can be detected through loss of ellipticity analysis which requires the evaluation of the tensor of elastic moduli. The tensor of elastic moduli can either be evaluated through micromechanics-based homogenization approaches [2, 56, 59, 127] or derived from phenomenological models [103, 104, 105, 106, 107]. We note that Geymonat et al. [50] have demonstrated the equivalence between Bloch-Floquet and loss of ellipticity analysis for infinite wavelength. Triantafyllidis and Maker [136] examined the microscopic and macroscopic instabilities in hypoelastic and hyperelastic laminates under plane-strain compression. Nestorović and Triantafyllidis [114] studied the instabilities in hyperelastic and elastoplastic laminates undergoing shear combined compression deformation. Arora et al. [5] further investigated the instabilities of hyperplastic laminates with inhomogeneous transition zones.

The majority of the studies focus on *purely* elastic or hyperelastic laminates. However, soft materials exhibit intrinsic viscoelasticity [78, 151], and the rate sensitivity of laminates

can substantially affect their buckling behavior. Biot [19] investigated the creep buckling of the confined viscoelastic laminates. Alur and Meaud [3] investigated the rate-dependent buckling behavior of the non-dilute visco-hyperelastic laminates. Slesarenko and Rudykh [131] investigated the rate dependence of wavy buckling patterns in visco-hyperelastic laminate composites, and they showed that the wavey pattern could be tuned by applying different strain rates.

Here, we focus on the role of the *visco*-hyperelasticity of laminate constituents on the microstructural buckling phenomenon. We investigate the dependence of critical buckling strain and wavenumber on the applied strain rates through the finite deformation post-buckling analysis. In addition, we analytical estimates for the critical buckling strain. We further examine the buckling pattern transformation for the "load-and-hold" regime. In addition, the influence of cyclic loading frequency and the pre-strain on dynamic mechanical properties are also explored. Finally, we show the applicability of simulations by comparing numerical results with the experimental results of 3D-printed laminates.

4.2 Numerical and analytical analysis

4.2.1 Numerical analysis of buckling of hyperelastic laminates

Viscoelasticity of material can be suppressed by fast and slow loading rates. Therefore, we can regard the material under the two extreme cases as hyperelastic materials, and then Bloch-Floquet analysis can be employed to calculate the critical strain and wavenumber [82]. The effective shear modulus contrast of fiber and matrix is $\mu_{eff}^{(f)}/\mu^{(m)} = \mu_{\infty}^{(f)}/\mu^{(m)} = 15$ for slow loading rates and $\mu_{eff}^{(f)}/\mu^{(m)} = \mu_{0}^{(f)}/\mu^{(m)} = 100$ for fast loading rates.

In Fig. 4.1, we show the critical buckling strain ε_{cr} (a) and the dimensionless critical

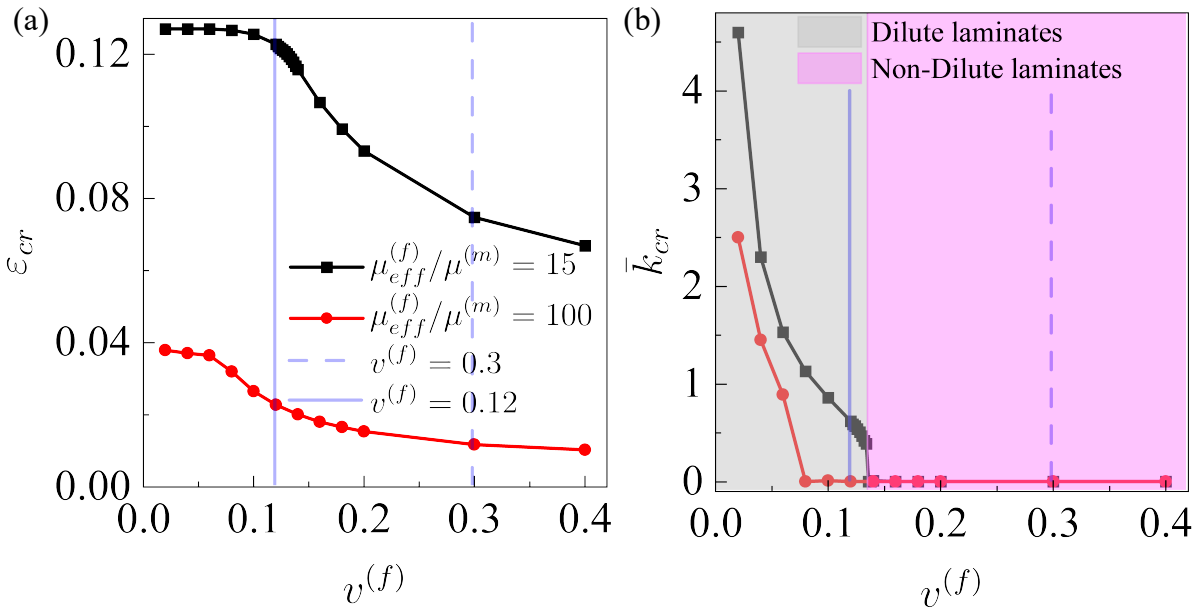

Figure 4.1: The dependence of the critical strain (a), and dimensionless critical wavenumber (b) on the fiber volume fraction.

wavenumber $\hat{k}_{cr} = k_{cr}W_0$ (b). k_{cr} is the number of the repeating pattern of the buckling shape per unit distance. The black and red curves denote the Bloch-Floquet results for $\mu_{eff}^{(f)}/\mu^{(m)} = 15$ and $\mu_{eff}^{(f)}/\mu^{(m)} = 100$, respectively. We can expect that the critical strain and wavenumber for visco-hyperelastic laminates can be transformed from the result of $\mu_{eff}^{(f)}/\mu^{(m)} = 15$ to that of $\mu_{eff}^{(f)}/\mu^{(m)} = 100$ with the increase in the loading rates. In Fig. 4.1 (b), we define two types of laminates: dilute laminates and non-dilute laminates (see the gray and pink map). For the dilute laminates, such as $v^{(f)} = 0.12$ (see the solid vertical blue line), the corresponding critical wavenumber can be transformed from a finite value to another value by increasing the loading rates. For non-dilute laminates, such as $v^{(f)} = 0.3$ (see the dashed vertical blue line), however, the critical wavenumber remains to be nearly zero regardless of loading rates.

4.2.2 Numerical analysis of buckling of visco-hyperelastic laminates

In this section, we show the details to probe the buckling behavior of visco-hyperelastic laminates through post-buckling analysis. We discuss the instabilities of both the dilute and non-dilute laminates. Specifically, we illustrate the results by examples of $v^{(f)} = 0.12$ and $v^{(f)} = 0.3$. We use the single-branch visco-hyperelastic model to characterize the visco-hyperelastic fiber. Thence, there are two parameters τ_1 and β_1. For simplicity, we ignore the subscript of τ_1 and β_1. The effective shear modulus contrast $\mu_{eff}^{(f)}/\mu^{(m)}$ is set to be bounded by $\mu_{\infty}^{(f)}/\mu^{(m)} = 15$ (for slow strain rate) and $\mu_{0}^{(f)}/\mu^{(m)} = 100$ (for fast strain rate). In addition, we find that the Weissenberg number can be introduced as a dimensionless strain rate for the loading path with a constant strain rate. Namely, the mechanical response is identical for the same Weissenberg number regardless of the value of relaxation time τ (see Appendix B.1).

The critical wavenumber of the laminates with $v^{(f)} = 0.3$ is nearly zero regardless of the loading rates (see the critical wavenumber corresponding to the dashed verticle blue line in Fig. 4.1 (b). That is, macroscopic instability is always triggered. For macroscopic instability, we can introduce a tiny angle $\theta_0 = 10^{-3}$ rad as the geometric imperfections (see Fig. 2.3 (b.1)). For $v^{(f)} = 0.12$, which is dilute laminates, the critical wavenumber changes from a certain number to another certain value, and finally arrives at zero with the increase in loading rate (see the critical wavenumber corresponding to the vertical solid blue line in Fig. 4.1 (b)). Therefore, the microscopic instability can be activated at a lower loading rate, while the macroscopic instability would gradually dominate the buckling mode with an increase in loading rates. Simulating the rate dependence of dilute laminates is far more challenging. Since the critical wavenumber of the initially triggered buckling mode is unknown for a certain strain rate, it is inappropriate to use a small angle as geometric

imperfections. We adopt the Cosine function as the imperfection, as shown in Fig. 2.3 (b.2). Specifically, the shape of fiber follows the function $\delta = \delta_0 cos\,(2\pi ks/H)$, where s range over 0 to H, $\delta_0 = \frac{d_0}{2} \times 10^{-3}$. Recall that the wavenumber k is unknown for a specific loading rate, so we have to scan the wavenumber k for a given loading rate to obtain the correct critical strain and wavenumber. In particular, we scan k from 0.001 to 5. For each scanned k, we can calculate the corresponding ε_{cr} and k_{cr}. Among them, the reasonable values of ε_{cr} and k_{cr} would correspond to the smallest value of ε_{cr}. The critical strain is monitored by the stress-strain curve and the related critical wavenumber can be directly recognized from the buckling pattern. More details about the identification of the critical strain and wavenumber are given in Appendix B.2 and Appendix B.3.

4.2.3 Theoretical prediction of the critical strain in visco-hyperelastic laminate composite

The instabilities in hyperelastic laminates have been widely investigated and the Bloch-Floquet analysis is typically used to identify the critical strain and wavenumber [18, 87]. For hyperelastic laminate composites, the buckling critical strain is determined by the fiber-to-matrix shear modulus contrast ($\mu^{(f)}/\mu^{(m)}$) which is equal to fiber-to-matrix stress contrast $\sigma_{11}^{(f)}/\sigma_{11}^{(m)}$ before buckling. For visco-hyperelastic laminates, however, there is no theoretical method to predict the strain onset of buckling. Here, we present a quantitative approach based on the assumption that the critical strain of laminate composites is determined by fiber-to-matrix stress contrast $\sigma_{11}^{(f)}/\sigma_{11}^{(m)}$.

In Fig. 4.2, we depict the critical strain versus the fiber-to-matrix stress contrast for hyperelastic laminate composite with $v^{(f)}$=0.3 (see the black dashed curve). The critical strain curve divides the regime into the buckled region (pink map) and unbuckled region

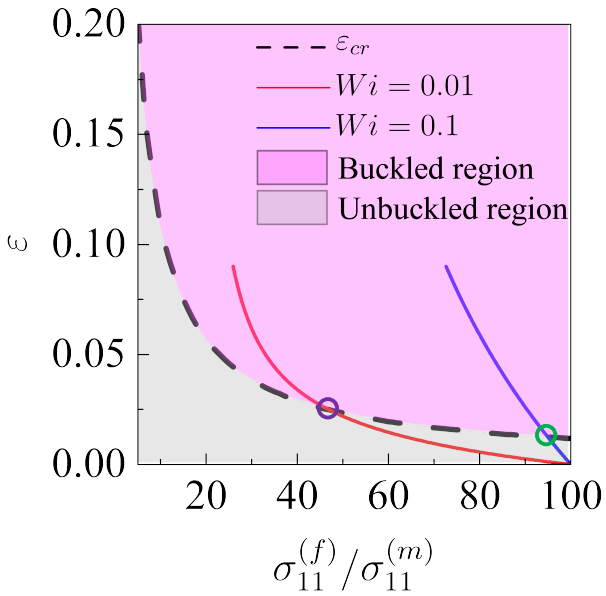

Figure 4.2: The illustration of determination of the critical strain for viscoelastic laminate composites.

(gray map). For visco-hyperelastic laminates, the $\sigma_{11}^{(f)}/\sigma_{11}^{(m)}$ changes with deformation. We illustrate the strain versus the $\sigma_{11}^{(f)}/\sigma_{11}^{(m)}$ curve based on Eqs. 2.13 and 2.25 by examples of $Wi = 0.01$ (see the red curve) and $Wi = 0.1$ (see the blue curve). We can observe that the $\sigma_{11}^{(f)}/\sigma_{11}^{(m)}$ gradually decreases with the increase in strain. As decreasing of $\sigma_{11}^{(f)}/\sigma_{11}^{(m)}$, the strain arrives at the corresponding critical strains which are the intersection of black dashed and red curves for $Wi = 0.01$ (see the violet hollow circle marker) as well as the intersection of black dashed and blue curves for $Wi = 0.1$ (see the green hollow circle marker), and then the buckling appears. For any given Weissenberg number, we can identify the intersection point as the critical strain.

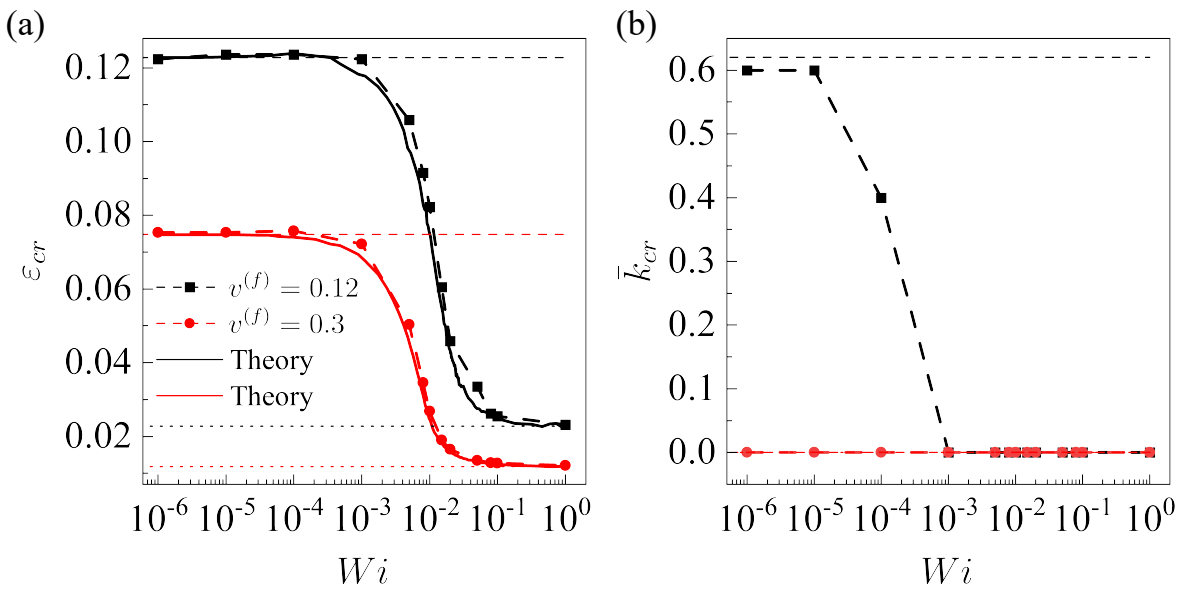

Figure 4.3: The dependence of the (a) critical strain and (b) dimensionless critical wavenumber on Wi for $v^{(f)}$=0.12 and $v^{(f)}$=0.3.

4.3 Results

4.3.1 The critical buckling strain and wavenumber

We start by examining the instability behavior of laminates undergoing compression with a constant applied strain rate. Figure 4.3 shows the numerical results of the rate-dependent critical strain (a) and wavenumber (b) for $v^{(f)} = 0.12$ (black dashed curve with square markers) and $v^{(f)} = 0.3$ (red dashed curve with circle markers). The corresponding theoretical critical strain, as introduced in see Sec. 4.2.3, is also presented for comparison (see solid curves). Dashed and dotted horizontal lines represent critical strain corresponding to the two limits (slow and fast loading rates) which are calculated from the Bloch-Floquet analysis.

As expected, the critical strain and wavenumber converge to the value corresponding

to the two limits. For instance, the black curves converge to the black dashed horizontal line at small Wi (such as $Wi = 10^{-6}$) and the black dotted horizontal line at large Wi (such as $Wi = 1$). The theoretical critical strain is in good agreement with the results from the numerical simulation (compare solid and dash-markers curves in Fig. 4.3 (a)). We observe that the critical strain decrease with the increase in strain rate. The rate dependence of the critical strain can be interpreted in terms of the fiber-to-matrix stress contrast. In hyperelastic laminates, the critical strain decrease with the increase in the fiber-to-matrix shear modulus (stress) contrast [90]. In visco-hyperelastic laminates (with visco-hyperelastic fibers), the fiber-to-matrix stress contrast increase with the increase in the strain rate for a given strain. Therefore, the corresponding critical strain decreases with an increase in the strain rate. As shown in Fig. 4.2, composites with $Wi = 0.1$ arrive at the critical strain earlier than composites with $Wi = 0.01$ (compare the violet and green hollow circle markers in Fig. 4.2).

One can note that the critical wavenumber for $v^{(f)} = 0.3$ always be close to zero with the increase in strain rate (see the red curve in (b)). Therefore, the buckling pattern always is macroscopic instability, whereas the buckling pattern for $v^{(f)} = 0.12$ changes from microscopic to macroscopic instability with the increase in strain rate. In particular, the dimensionless critical wavenumber decreases from 0.6 to nearly zero with an increase in strain rate (see the black dashed curve in (b)).

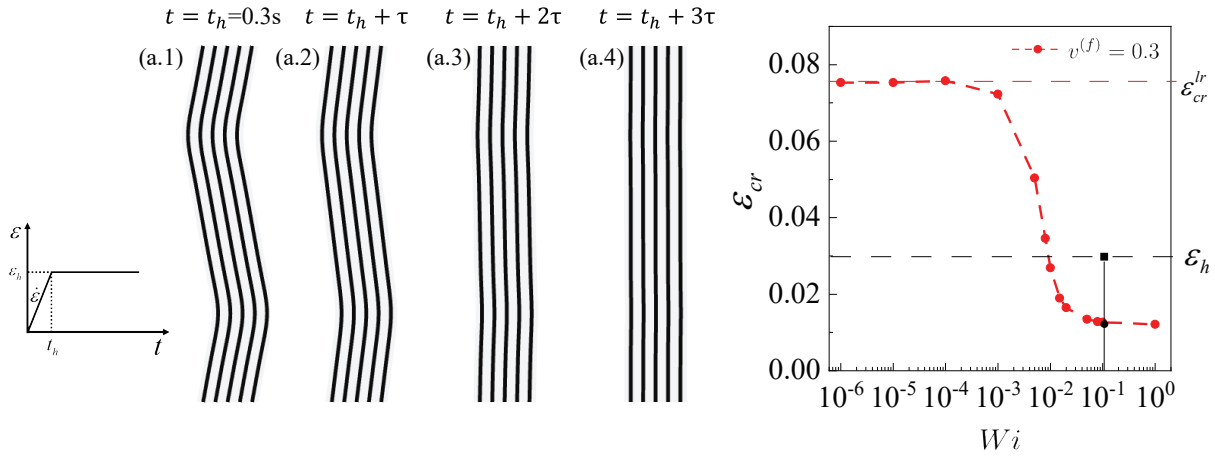

Figure 4.4: (a) The buckling pattern evolves with time in the holding process ($t > t_h$); (b) illustratively explains the rate-dependent buckling pattern.

4.3.2 The load-and-hold loading path

In this subsection, we probe the pattern transformation when applying the load-and-hold loading path defined as

$$\varepsilon(t) = \begin{cases} \varepsilon = \dot{\varepsilon} t & t \leq t_h \\ \varepsilon_h & t > t_h \end{cases} \tag{4.1}$$

where $\dot{\varepsilon} = Wi/\tau$ and t_h are the strain rate and time to reach a designated strain ε_h (see the inset on the left side Fig. 4.4 (a)). For discussions, we illustrate the results by the example of the laminate structure with $v^{(f)} = 0.3$ and the loading path $Wi = 0.1$, $\tau = 1s$ and $\varepsilon_{\mathrm{h}} = 0.03$. Figure 4.4 (a.1)-(a.4) shows the pattern transformation. Interestingly, we observe that the buckling pattern gradually disappears in the holding process ($t > t_h$). We can explain this phenomenon based on the rate-dependent critical strain, as illustrated in Fig. 4.4 (b). Since $\varepsilon_{\mathrm{h}} = 0.03$ is larger than the critical strain corresponding to $Wi = 0.1$ (the black square is above the black circle in (b)), the buckling can be triggered. However, once holding the strain, the effective strain rate would be zero, so the corresponding critical strain would be

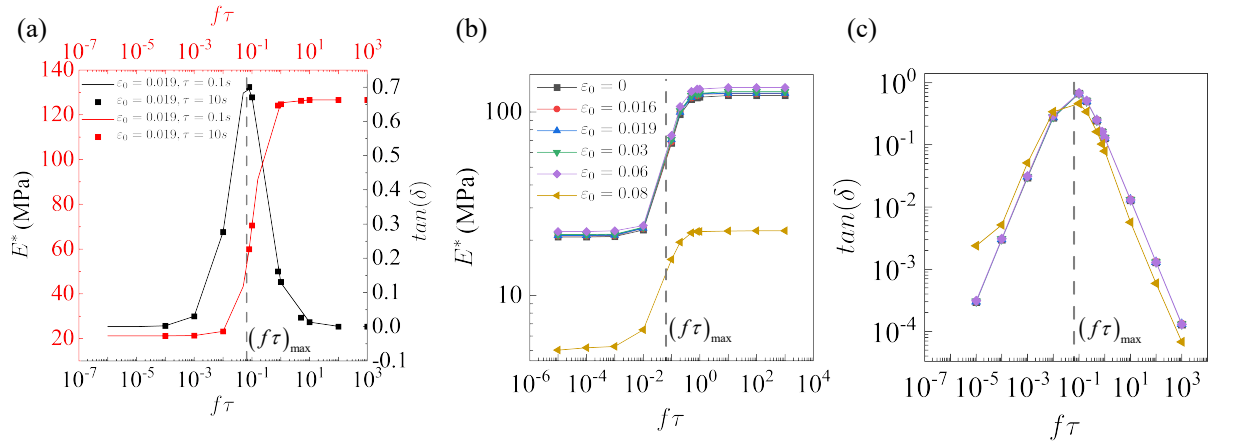

Figure 4.5: (a) The dynamic mechanical properties $|E^*|$ (red) and tanδ (black) versus $f\tau$ for different relaxation time. (b) The dynamic modulus $|E^*|$ and (c) loss factor tanδ versus $f\tau$ with different pre-strain ε_0.

equal to $\varepsilon_{cr}^{lr} = 0.07482$ which is large than the applied holding strain ε_h (the red dashed line is above the black square in (b)). Therefore the buckling pattern gradually disappears as the stress relaxes in the fiber. One can expect that the buckling pattern will be maintained if ε_h is large than ε_{cr}^{lr} (ε_h is higher than the red dashed line in (b)) due to the fact that ε_h is always larger than the critical strain for all range of strain rates. We also confirm the permanent buckling pattern in simulations (we have not shown figures here).

4.3.3 Dynamic mechanical properties under cyclic loading

In this subsection, we show the influence of the cyclic loading frequency f and pre-strain ε_0 on the dynamic modulus $|E^*|$ and loss factor (damping) $tan\delta$. The dynamic mechanical properties are determined through simulations. In particular, we pre-compress the laminates to a pre-strain ε_0 with a certain strain rate ($t < t_0$), then we hold the pre-strain for a while until the laminates relax to the equilibrium state ($t_0 < t < t_d$). Finally, we cyclic load the pre-compressed laminates to obtain the dynamic mechanical properties ($t > t_d$) (see

Appendix B.4).

The dynamic mechanical properties of homogeneous viscoelastic material are identical for the same value of $f\tau$. Inspired by this, We examine whether the dynamic mechanical properties of the laminate composite are also identical for the same value of $f\tau$ regardless of the relaxation time. The laminate structure with $v^{(f)} = 0.3$ undergoing pre-strain $\varepsilon_0 = 0.019$ is simulated as an example. Figure 4.5 (a) shows the dynamic modulus (see red curve) and loss factor (see black curve) of the composites whose fiber's relaxation time is 0.1 s (see solid curves) and 10 s (see square markers). We observe that the dynamic mechanical properties are identical for different relaxation times when the $f\tau$ is the same. The frequency dependence of the dynamic mechanical properties of the laminates is similar to that of homogeneous material. In specific, the damping increase first and then peaks at $(f\tau)_{max} = \sqrt{|E^*|_{\min}/\left(|E^*|_{\max}\right)}/2\pi$ (see the vertical gray dashed line), and finally decreases with the increase in $f\tau$. The dynamic modulus shows an increasing trend with the increase in $f\tau$ and increases sharply when $f\tau$ is around $(f\tau)_{max}$. Moreover, the dynamic modulus approach asymptotic values when $f\tau$ is small (such as $f\tau = 10^{-5}$) and large (such as $f\tau = 10$).

We further examine the influence of pre-strain ε_0 on the dynamic mechanical properties. Figure 4.5 (b) and (c) show the dynamic modulus and damping with different pre-strain ε_0, respectively. Specifically, we examine the laminates with $\varepsilon_0 = 0$ (black), 0.016 (red), 0.019 (blue), 0.03 (green), 0.06 (violet), and 0.08 (brown). In terms of section 4.3.2, we note that the buckling pattern gradually disappears (or can be maintained) in the holding process ($t_0 < t < t_d$) when the pre-strain ε_0 is smaller (or larger) than the critical strain at the quasi-static loading condition ($\varepsilon_{cr}^{lr} = 0.07482$). Therefore, we can expect that pre-strain has a distinct effect on the dynamic mechanical properties for $\varepsilon_0 < \varepsilon_{cr}^{lr}$ and $\varepsilon_0 > \varepsilon_{cr}^{lr}$.

As expected, we observe that the dynamic modulus and loss factors have a weak depen-

dence on the pre-strain when the pre-strain range from 0 to 0.06 (see the black, red, blue, green and violet curves), while the dynamic mechanical properties show a sharp change when pre-compression strain $\varepsilon_0 = 0.08$ (see the brown curve). Remarkably, the dynamic modulus significantly decreases when the pre-strain increases from 0.06 to 0.08 (compare the violet and brown curves in (b)). For example, the dynamic modulus of laminates with $\varepsilon_0 = 0.06$ is around six times of that of laminates with $\varepsilon_0 = 0.08$ for $f\tau = 1$. However, damping can be significantly increased (or decreased) for the $f\tau < (f\tau)_{max}$ (or $(f\tau > f\tau)_{max}$) when the pre-strain increases from 0.06 to 0.08 (compare the violet and brown curves in (c)). For example, the damping of the laminates with $\varepsilon_0 = 0.08$ is around 7.6 and 0.6 times of that of laminates with $\varepsilon_0 = 0.06$ for $f\tau = 1{\times}10^{-5}$ and $f\tau = 1$, respectively. One can also note that the pre-strain has a more negligible effect on the frequency dependence of the dynamic mechanical properties. The dynamic mechanical properties show similar frequency dependence even when $\varepsilon_0 > \varepsilon_{cr}^{lr}$ (see (b) and (c)).

4.4 Application of multiple-branch model for 3D-printed soft laminate composite

In this section, we characterize the instability of the 3D-printed laminate composite in experiments, validating the capability of our numerical analysis. Here, fiber and matrix are manufactured with Digital material with Shore index 95 (DM95) and TangoPlus, respectively. To accurately model the instability behavior, the visco-hyperelastic model with multiple relaxation times is applied for both fiber and matrix, the material extraction procedures are provided in Appendix B.5.

We conduct the in-plane compression at room temperature ($T = 21^{\circ}$C) with the MTS

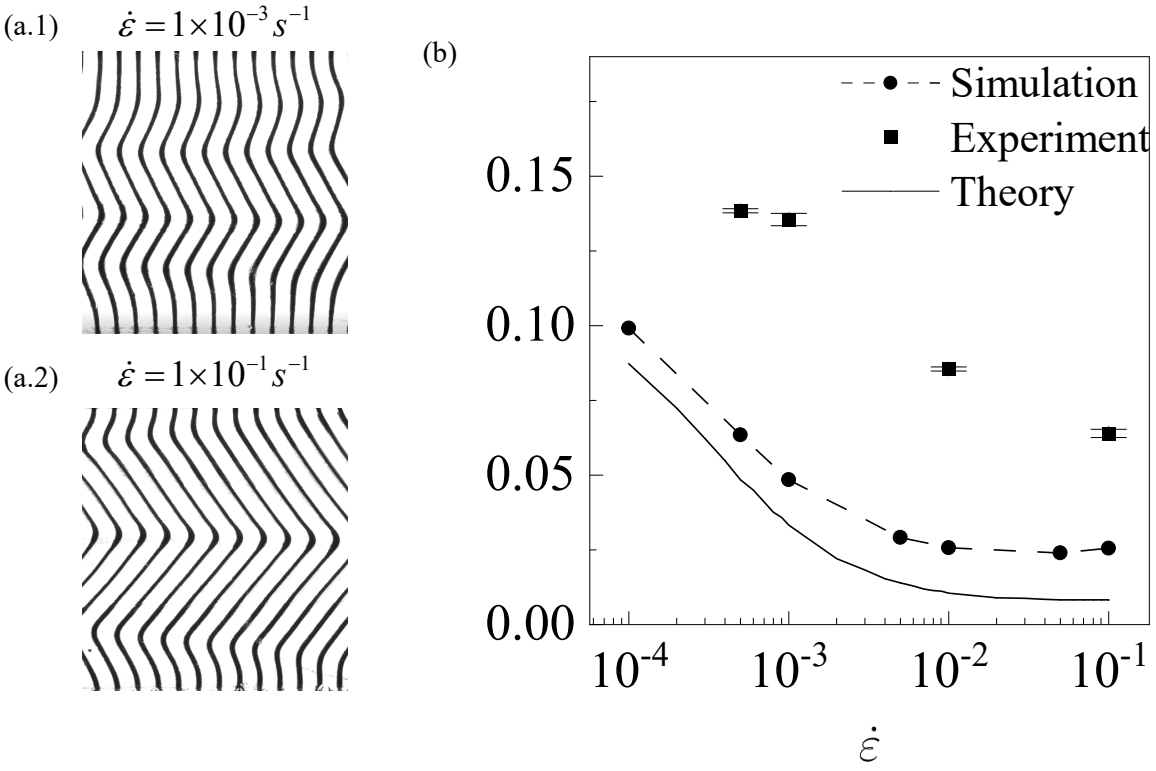

Figure 4.6: (a) The buckling pattern for (a.1) $\dot{\varepsilon} = 10^{-3}s^{-1}$ and (a.2) $\dot{\varepsilon} = 10^{-1}s^{-1}$. (b) The dependence of experimental, simulation and theoretical critical strain on applied strain rate.

system and the out-plane deformation is restricted by a transparent fixture. The structure with the volume fraction $v^{(f)} = 0.2$ is investigated. Specifically, The dimensions of samples are prepared with $d_0 = 0.8mm$ and $W_0 = 4mm$. We conduct the tests with three different applied strain rates $\dot{\varepsilon} = 10^{-3}s^{-1}$, $10^{-2}s^{-1}$ and $10^{-1}s^{-1}$, and each test is repeated at least three times. $v^{(f)} = 0.2$ corresponds to non-dilute laminates (see Fig. 4.1). Therefore, the macroscopic instability is expected; and the buckling pattern with long-wavelength is also confirmed by experiment tests for low strain rate ($\dot{\varepsilon} = 1\times10^{-3}s^{-1}$, see Fig. 4.6 (a.1)) and high strain rate ($\dot{\varepsilon} = 1\times10^{-1}s^{-1}$, see Fig. 4.6 (a.2)).

Figure 4.6 (b) shows the dependence of experimental (scatter square markers) and simulated (dashed black curve) critical strain on the applied strain rate. The theoretical critical strain is also presented for comparison (solid black curve). We note that the critical strain decreases with an increase in strain rate and the numerical simulation can well capture this rate dependence of the critical strain. We also note that the theoretical results could still give qualitative predictions for the critical strain (see the solid black curve) even though the fiber and matrix visco-hyperelastic materials.

The simulation results are lower than that of the experiments. Multiple potential reasons could be attributed to the errors. For instance, the load cell should be accelerated to achieve the stable strain rate we need in experiments, and friction in the fixture cannot be eliminated. In addition, the material parameters are from the DMA test and the non-linear response of fiber and matrix is characterized by the neo-Hookean model. Therefore, nonlinearity, such as stiffening [8, 49] and damage [151, 169], beyond the capability of the neo-Hookean model can cause deviation from the real scenarios. Furthermore, the interphases formed in the 3D-printing process could also affect the instability behavior of the soft laminates [5]. The buckling of composites can be affected by materials imperfections [62, 63, 122] or geometry

uncertainties [29, 37, 161]. We can qualify the effect of uncertainties through stochastic analysis [42, 100].

4.5 Concluding remarks

In this chapter, we study the rate-dependent instabilities in visco-hyperelastic laminates through post-buckling analysis. Based on the results for the hyperelastic laminates, we categorize laminates into dilute and non-dilute laminates. The post-buckling of the visco-hyperelastic non-dilute laminates can be simulated with the angle geometric imperfections. To identify the buckling of visco-hyperelastic dilute laminates, we implemented the Cosine function-shaped imperfections and wavenumber scanning. The post-buckling analysis indicates that the critical strain of both dilute and non-dilute laminates are bounded by value at extreme slow and fast loading cases and monotonically decreases with the increase in the strain rates. We also note that critical wavenumber for dilute laminates is also rate dependent. We provide an analytical method to determine the critical strain based on the assumption that the critical strain is controlled by the contrast in the stress of fiber and matrix. The theoretical results are in good agreement with the numerical solutions. Therefore, we can predict that the critical strain will monotonically increase with the increase in the applied strain rates if the soft matrix is visco-hyperelastic material and the stiff matrix is hyperelastic material, as demonstrated by Alur and Meaud [3].

Next, we study the load-and-hold deformation mode. We find that the buckling pattern disappears when the pre-strain (ε_h) is smaller than the critical strain (ε_{cr}^{lr}) at the quasi-static loading condition, while the buckling pattern is maintained if the holding strain ε_h is higher than ε_{cr}^{lr}. Therefore, we investigate the dependence of dynamic mechanical properties on the pre-strain with two cases: the pre-strain ε_0 larger and smaller than the ε_{cr}^{lr}. When the

pre-strain is smaller than ε_{cr}^{lr}, dynamic mechanical properties have a similar frequency dependence as the homogeneous viscoelastic materials, and the pre-strain has a slight effect on the dynamic modulus and damping. When pre-strain is larger than ε_{cr}^{lr}, dynamic mechanical properties still show similar frequency dependence behavior. However, the pre-strain can significantly change the value of dynamic modulus and damping.

We finally study the buckling of the 3D-printed soft laminate composite. The multiple-branch visco-hyperelastic model is adopted for both matrix and fiber. We note that the critical strain decrease with an increase in the strain rate and the numerical method can well predict the rate-dependence of the critical strain. In addition, we find that the analytical results can also predict the measured rate-dependent critical strain. Therefore, the analytical method is still applicable for the identification of the critical strain for the laminates even though both fiber and matrix are visco-hyperelastic materials with multiple relaxation times.

In this chapter, the non-linear response of fiber is described by the neo-Hookean model. However, other non-linear effects such as softening [34, 154], stiffening [8, 49] and damage [151, 169] are not included, and fully considering these nonlinearities could improve the accuracy of numerical simulation, especially for composites with large deformations. This chapter reveals that the instabilities of (hyperelastic and visco-hyperelastic) laminates are dominated by the stress contrast in fiber and matrix. Therefore, we can design the laminates with desired properties by carefully controlling the fiber-to-matrix stress contrast. For instance, we can adjust the fiber-to-matrix stress contrast by tuning the relaxation time of materials. In practice, we can adjust the relaxation time by changing the temperature or light intensity in the process of additive manufacturing [149, 150]. Moreover, the instabilities in visco-hyperelastic 3D fiber composites could also be controlled by the fiber-to-matrix stress contrast and this could be a potential research direction in the future. In addition,

the microstructure in soft composites can be sharply transformed by external stimuli remotely, such as electric and magnetic fields [53, 69, 72, 117]. Therefore, the properties of soft composites can be customized remotely.

CHAPTER 5

TOWARDS UNDERSTANDING THE ROLE OF VISCOELASTICITY IN INSTABILITIES IN SOFT PARTICULATE COMPOSITES*

Yuhai Xiang, Dean Chen, Nitesh Arora, Stephan Rudykh

*(*Prepared for submission to a journal)*

This chapter investigates the interplay between viscoelasticity and elastic instabilities in soft particulate composites under finite deformation. We study the dependence of the critical strain and wavelength on the applied strain rate in a soft particulate composite system. The composite is subjected to in-plane deformation at constant strain rates, and experiences microstructural buckling upon reaching exceeding the critical strain level. In the numerical simulations, we employ the single and multiple-branch visco-hyperelastic models. In addition, we perform experiments on the 3D-printed soft particulate composite. We find that the critical strain in the composites – characterized by the single-branch model – shows a non-monotonic dependence on the strain rate, reaching a maximum at a specific strain rate. The corresponding critical wavelength dependence is similarly non-monotonic and is not a smooth function of the strain rate. The buckling pattern with different critical wavelengths can be activated by changing strain rates, and a broader set of possible buckling modes can be triggered in composites with higher strain-energy factors. In the composites characterized by the multiple-branch model, the critical strain function exhibit multiple local maxima following a superposition of single-branch responses. The branch with a larger relaxation time has a more significant effect on the critical strain. Moreover, we can increase a certain local maximum of critical strain by increasing the corresponding strain-energy

factor. Furthermore, the comparison of the experiment and simulation of the 3D-printed particulate composite with a broad spectrum of relaxation times demonstrates the ability of the numerical model to predict the critical buckling strain and pattern.

5.1 Introduction

Soft microstructured materials are prone to developing elastic instabilities frequently leading to microstructure transformations [82]. In the post-buckling regime, the material can exhibit auxetic behavior [16, 86, 110], shape transformations [17], tunable color [84], and tunable bandgap [87, 146]. Moreover, buckling-induced microstructure transformations can be employed to design soft robots [121].

The "small-on-large" framework [115] is frequently used to detect the onset of instabilities. In soft composites, the instabilities can develop at microscopic and macroscopic length scales [50]. The onset of the macroscopic or longwave instability can be detected through the loss of ellipticity analysis requiring the evaluations of the tensor of elastic moduli. The tensor of elastic moduli can be calculated through analytical or numerical micromechanics-based homogenization approaches [56, 59, 127] or, alternatively, can be derived from phenomenological models [103, 104, 105, 106, 107]. The analysis of microscopic instability requires a more demanding approach and usually employs the Bloch-Floquet method [50]. Triantafyllidis et al. [137] applied the technique to study the instability of the two-phase composite with circular inclusions arranged in a square and a diagonal 2D periodic unit cell with various volume fractions. Li et al. [83] reported the experimental observations of the numerically predicted instability-induced microstructure transformations in the soft particulate composites. Chen et al. [28] examined the instability in the soft particulate composites with varying configurations of periodically distributed inclusions and reported distinct instability

patterns, including strictly doubled periodicity, seemingly nonperiodic state, and longwave patterns. Arora et al. [5] studied the influence of inhomogeneous interphase on instabilities in laminates. The effect of phase compressibility of the layered materials has been analyzed by Li et al. [87]. More recently, Li et al. [88] reported the experimental observations of instability-driven domain formations in soft laminates. Rudykh and deBotton [127] analyzed the macroscopic instabilities in 3D fiber composites. The series of works [7, 46, 85, 132] investigated the microscopic instability and associated buckling modes in deformable 3D fiber composites.

Most theoretical and numerical studies examined the instability phenomenon in purely elastic or hyperelastic materials. However, soft materials exhibit inelastic behavior. The intrinsic viscoelasticity of soft materials [78, 151, 152] can significantly influence the buckling phenomenon. Alur and Meaud [3] performed a numerical study of the rate-dependent behavior of the viscoelastic laminates with a stiff elastic layer and soft viscoelastic matrix. Slesarenko and Rudykh [131] reported the experimental observation of the tunability of wavy patterns in soft viscoelastic laminates. However, little is known about the interplay between viscoelasticity and the instability phenomenon in soft composites.

In this chapter, we examine the role of viscoelasticity in the instabilities in the soft particulate composite. Section 5.2 summarizes the numerical results, illustrating the dependence of the buckling characteristics on loading rates for the soft composite described by (i) a single-branch and (ii) multiple-branch visco-hyperelastic models. Finally, in Sec. 5.3, the applicability of the multiple-branch visco-hyperelastic model is illustrated in comparison with the experimental results for the 3D-printed soft particulate composites.

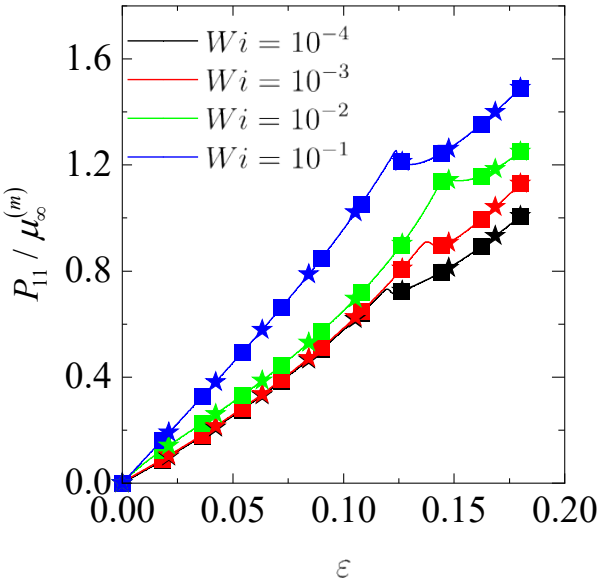

Figure 5.1: The dependence of the normalized stress-strain curves on Wi. The solid curve, square and star marks represent the results for $\tau_1 = 0.1s$, $1s$ and $10s$, respectively.

5.2 Results

5.2.1 Single-branch visco-hyperelastic model

We start by discussing the rate-dependent buckling behavior with the single-branch visco-hyperelastic model. For the single-branch model, there are only two independent parameters: relaxation time τ_1 and strain-energy factor β_1. We study the effect of τ_1 and β_1 on the critical strain and wavelength.

The effect of relaxation time $\boldsymbol{\tau_1}$

Figure 5.1 shows the dependence of normalized stress component $P_{11}/\mu_\infty^{(m)}$ on strain for different values of the Weissenberg number, $Wi = \dot{\varepsilon}\tau_1$. We illustrate the results for the composite with $\beta_1 = 1$ loading regimes from $Wi = 10^{-4}$ to 10^{-1}. In particular, the black, red,

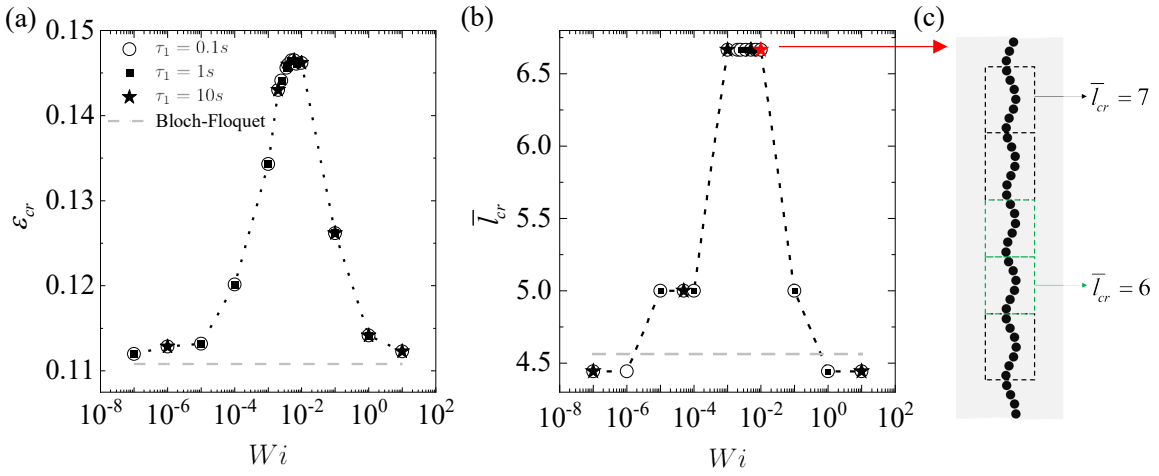

Figure 5.2: The dependence of (a) critical strain ε_{cr} and (b) normalized critical wavelength $\bar{l}_{cr}$ on Wi. (c) The buckling pattern corresponds to the red marker in (b). The circle, square, and star marks represent the results for τ_1=0.1s, 1s and 10s, respectively.

green, and blue curves and markers represent the mechanical response for composite with the applied loading rates corresponding to $Wi = 10^{-4}$, 10^{-3}, 10^{-2}, and 10^{-1}, respectively. The solid curves, square, and star markers correspond to the results for the composites with τ_1= 0.1s, 1s, and 10s, respectively. We note that the mechanical response is independent of the relaxation time τ_1 for a given Wi. The same values of Wi indicate that composites experience equivalent loading rates despite being characterized by different relaxation times τ_1. While this behavior can be expected for homogeneous material, in the particulate composite, however, is not apparent since the deformation and the deformation rate vary spatially.

Figure 5.2 shows the dependence of the critical strain ε_{cr} (a) and normalized critical wavelength $\bar{l}_{cr}$ (b) on Weissenberg number Wi, and the buckling pattern (c) corresponding to $Wi = 10^{-2}$. We highlighted the critical wavelength for the composite loading with the strain rate corresponding to $Wi = 10^{-2}$ by the red star in Fig. 5.2 (b). The normalized critical wavelength represents the number of inclusions in the repeating set of the buckled

shape. The critical strain and wavelength are identified from the stress-strain curve and the buckling pattern, respectively. Specifically, we monitor the macroscopic stress of the composites during the compression, and we identify the strain at which the stress sharply changes with the increase in the applied strain as the critical strain. The discrete Fourier transform (DFT) method is employed to identify the critical wavelength of the buckled composites (see Appendix B.6). Here, the circle, square, and star markers represent the results for the composites with τ_1= 0.1s, 1s and 10s, respectively. The critical strain is a smooth function of the Weissenberg number. We connect the markers with a dotted curve to indicate the rate dependence trend. However, the critical wavelength is not a smooth function of the Weissenberg number, so the connecting curves between the markers show the variation tendency only, not the actual value. High (such as $Wi = 10$) and low loading rates (such as $Wi = 10^{-7}$) can suppress the viscoelasticity. So that we can estimate the critical strain and wavelength for the two extreme cases through the Bloch-Floquet analysis for purely elastic composites [83, 132]. The results for the purely elastic composites are denoted by the gray dashed curve in Fig. 5.2 (a) and (b). Note that, due to the high contrast in $\mu^{(i)}/\mu_{\infty}^{(m)}$, the critical strain and wavelength in the two limits (high and low loading rates) are almost identical.

We note that the critical strain and wavelength are identical for the same Wi regardless of τ_1 (compare the different types of markers). Besides, the critical strain approaches the value corresponding to the limits for sufficiently fast (or slow) loading rates. Specifically, $\varepsilon_{cr} = 0.1123$ (for $Wi = 10$) and $\varepsilon_{cr} = 0.11198$ (for $Wi = 10^{-7}$), approaching the critical value for the elastic composites, $\varepsilon_{cr} = 0.11078$, as calculated through the Bloch-Floquet analysis. Interestingly, for Wi ranging from 10^{-7} to 10, the dependence of the critical strain on Wi is non-monotonic, with the maximum of the critical strain being significantly larger

than the values in the two extreme cases. In particular, the peak value of the critical strain is 0.1466, being larger than the critical strain (0.11078) from the Bloch-Floquet analysis (compare the peak value of the black dotted curve and the value of the gray dashed curve in Fig. 5.2 (a)). This composite behavior is different from that observed in the laminated composite, for which the critical buckling strain is a monotonic function of the strain rate bounded by the two limits for sufficiently fast and slow loading rates. For example, in the laminates with viscoelastic matrix (and elastic layers), the critical strain increases with an increase in the applied strain rate [3], and the opposite rate dependence will be observed if the fiber is viscoelastic [131].

We observe that the rate dependence of the critical wavelength is non-monotonic (see Fig. 5.2 (b)), reaching the maximum plateau at a range of intermediate values of Wi. In particular, $\bar{l}_{cr}$ reaches the highest plateau value when Wi is within the range of 10^{-3} to 10^{-2}. For low loading rates, such as $Wi = 10^{-7}$, and high loading rates such as $Wi = 10$, the critical wavelength reaches the plateau value $\bar{l}_{cr} = 4.44$ being close to the value from the Bloch-Floquet analysis ($\bar{l}_{cr} = 4.56$). Recall that the normalized critical wavelength $\bar{l}_{cr}$ represents the number of inclusions in the repeating sets of the instability-induced wavy pattern; therefore, $\bar{l}_{cr}$ might be expected to be an integer. However, a buckling pattern may not attain a perfect periodicity (with an integer number of repeating inclusions), as illustrated in Fig. 5.2 (c), where two alternating sets of six and seven inclusions can be observed. To identify the wavelength of the instability-induced irregular quasiperiodic pattern, we use the discrete Fourier transform (DFT) method. Through the analysis, we determine the dominant wavelength in the instability-induced wavy pattern (the details are provided in Appendix B.6). Note that the obtained normalized critical wavelength is not always an integer. For example, the DFT dominant wavelength of the composite undergoing deformation

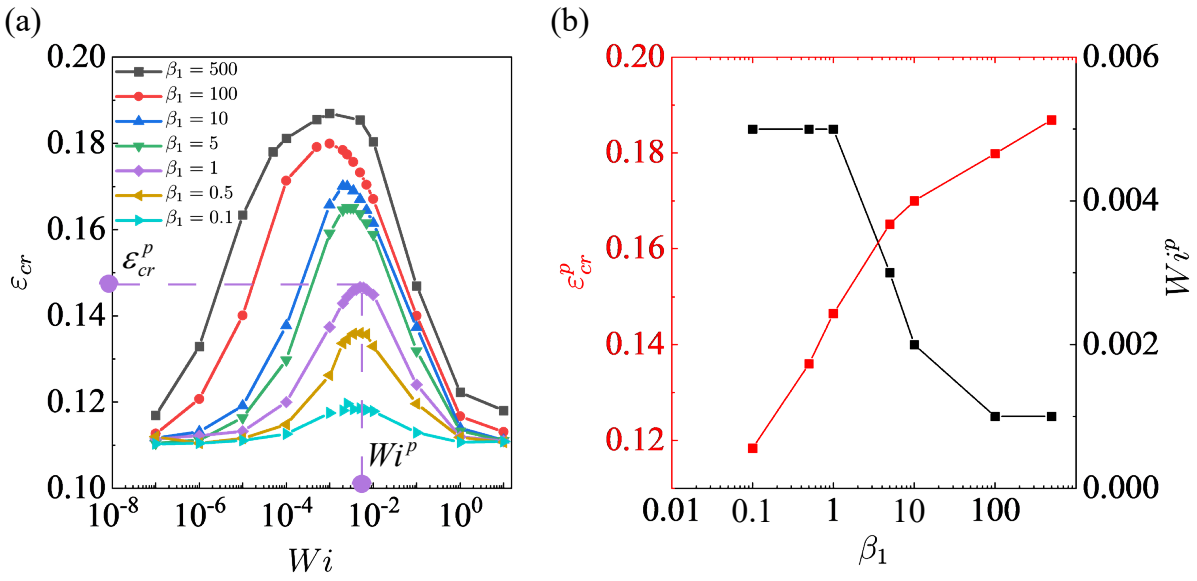

Figure 5.3: The dependence of (a) rate-dependent critical strain ε_{cr}, (b) peak point-related critical strain ε_{cr}^p and Weissenberg number Wi^p on β_1.

at the rate corresponding to $Wi = 10^{-2}$ (shown in Fig. 5.2 (c)) is 6.67; the value is between the two wavelengths with an integer number of inclusions (6 and 7) of the corresponding repeating blocks. We also note that the critical wavelength function is not smooth; with the Weissenberg number increasing from 10^{-7} to 10, the critical wavelength takes the discrete values of 4.44, 5.0, and 6.67, respectively. This observation indicates that different loading rates may activate buckling modes with different wavelengths and the wavelength of the activated modes does not continuously change with an increase in the loading rate.

The effect of the strain-energy factor $\boldsymbol{\beta_1}$

To illustrate the influence of the strain-energy factor on the buckling characteristics, we first show the dependence of the critical strain ε_{cr} on the strain-energy factor β_1 in Fig. 5.3 (a). Specifically, we show the rate-dependent critical strain for β_1 changing from 0.1 to

500. For later discussions, let us consider the dependence of the peak point-related critical strain ε_{cr}^{p} (red curve) and Weissenberg number Wi^{p} (black curve) on the strain-energy factor (see Fig. 5.3 (b)). Here, ε_{cr}^{p} is the maximum critical strain and Wi^{p} is the corresponding Weissenberg number for a given β_1 (ε_{cr}^{p} and Wi^{p} for $\beta_1 = 1$ are illustrated by the violet dashed lines in (a)).

We observe that the critical strain shows a similar rate dependence for different β_1, namely, the critical strain increases first, then, after reaching the maximum, it starts decreasing with an increase in Wi. For example, for $\beta_1 = 1$, the critical strain increases until its maximum value reaching $\varepsilon_{cr}^{p} = 0.1466$ at $Wi^{p} = 5{\times}10^{-3}$, and then decreases with a further increase in Wi (see the violet curve in (a)). In addition, the critical strain increases with an increase in β_1 (compare the different colored curves in Fig. 5.3 (a)). Figure 5.3 (b) shows that the peak point of critical strain, ε_{cr}^{p} increases with an increase in β_1. However, Wi^{p} shows the opposite trend, namely, it decreases with an increase in the strain-energy factor approaching around $5{\times}10^{-3}$ and 10^{-3} when $\beta_1 \leq 1$ and $\beta_1 \geq 100$. The dependence of the critical strain on the strain-energy factor can be related to the effective modulus contrast of inclusions and matrix. For the hyperelastic particulate composites (in the absence of viscoelasticity), it has been reported that the critical strain monotonically increases with a decrease in the inclusions-to-matrix shear modulus contrast [83]. In visco-hyperelastic materials, the effective modulus of the matrix increases with an increase in β_1. Therefore, the modulus contrast between inclusions and matrix is lower for composites with a larger strain-energy factor for a given loading rate. As a result, the corresponding critical strain increases with an increase of β_1.

Figure 5.4 shows the dependence of the normalized critical wavelength $\bar{l}_{cr}$ on Weissenberg number Wi. The results are shown for the composites with various strain-energy factor

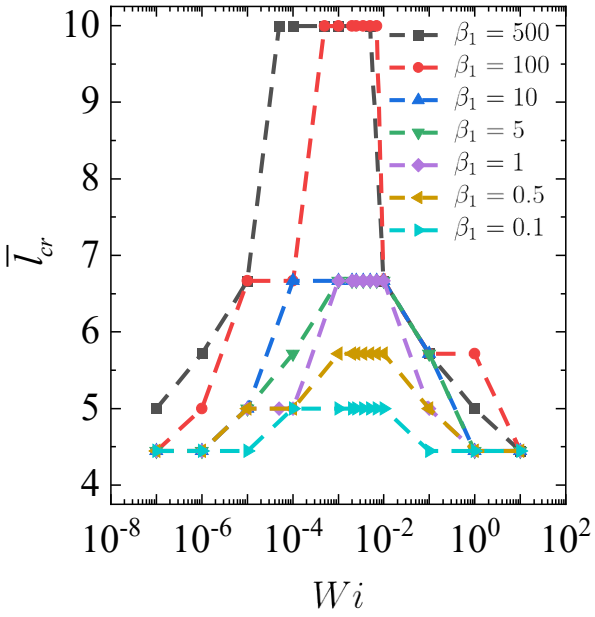

Figure 5.4: The dependence of normalized critical wavelength $\bar{l}_{cr}$ on Weissenberg number Wi for composites with various strain-energy factor β_1.

values β_1 (from 0.1 to 500). Similar to the previous observations, here, we also find that $\bar{l}_{cr}$ is not a smooth function of the Weissenberg number, and it only switches between values 4.44, 5.0, 5.71, 6.67, and 10 with a change in Wi. We observe that slow (such as $Wi = 10^{-7}$) and fast (such as $Wi = 10$) loading rates limit the appearance of possible buckling modes. In particular, $\bar{l}_{cr}$ shifts between 4.44 and 5.0 only for $Wi = 10^{-7}$, and takes a single value of 4.44 for $Wi = 10$ over a range of β_1 (from 0.1 to 500).

In addition, we note that $\bar{l}_{cr}$ shows an increasing trend with an increase in β_1 for composites with strain-energy factors smaller than 100. The normalized critical wavelength can span a broader range of values with the change of Wi for higher β_1. For example, $\bar{l}_{cr}$ has two possible values for $\beta_1 = 0.1$ (see the light blue curve), three possible values for $\beta_1 = 0.5$ and 1 (see the brown and violet curves), four possible values for $\beta_1 = 5$ and 10 (see the green and dark blue curves), and five possible values for $\beta_1 = 100$ and 500 (see the red and

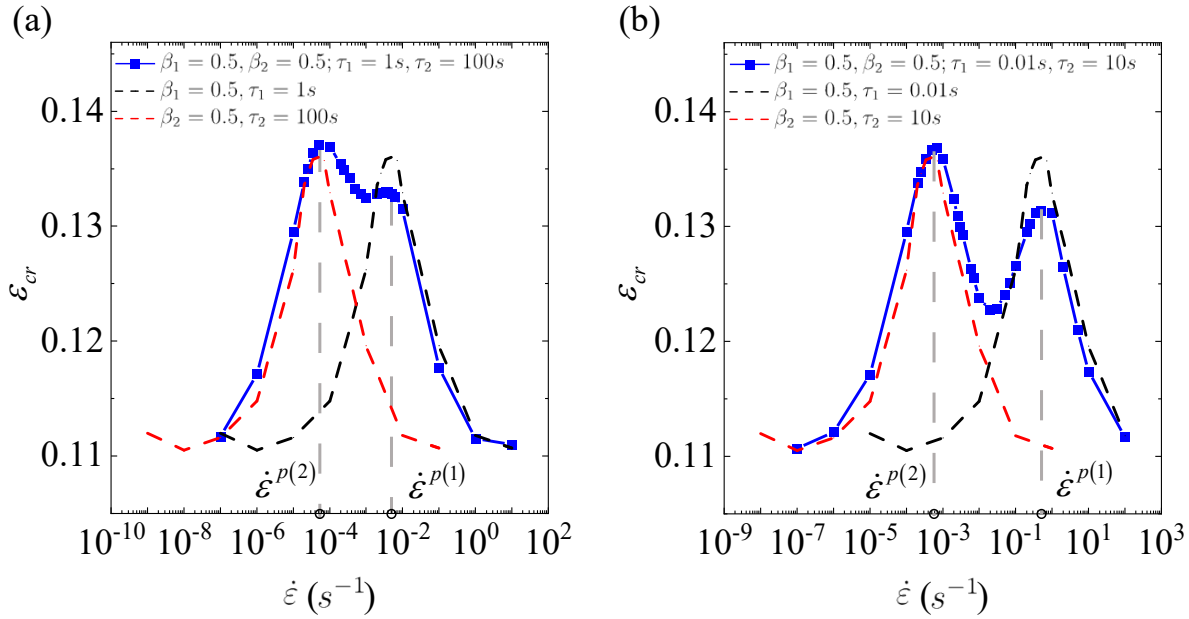

Figure 5.5: The dependence of critical strain on strain rate for the composites with matrix characterized by double-branch model with (a) τ_1=1s and τ_2=100 s, (b) τ_1=0.01s and τ_2=10 s. The strain-energy factors are $\beta_1 = \beta_2 = 0.5$.

black curves). We can conclude that overall a broader set of possible buckling modes can be activated in composites characterized by higher strain-energy factors.

5.2.2 Multiple-branch visco-hyperelastic model

In this section, we examine the rate sensitivity of the critical strain in the composite with the matrix characterized by the multiple-branch visco-hyperelastic model. Figure 5.5 shows the dependence of critical strain on strain rate for the composites with matrix described by the double-branch model (corresponding to $M = 2$ in Eq. 2.25). The results are shown for the composites with $\beta_1 = \beta_2 = 0.5$, and $\tau_1 = 1s$ and $\tau_2 = 100\ s$ in Fig. 5.5 (a); and for the case of $\beta_1 = \beta_2 = 0.5$, and $\tau_1 = 0.01s$ and $\tau_2 = 10\ s$ in Fig. 5.5 (b). The continuous and dashed curves represent the results for the double-branch and single-branch

models, respectively. The single branch models are characterized by their corresponding strain-energy factor and relaxation times: $\beta_1 = 0.5$, $\tau_1 = 1s$ (the black dashed curve) and $\beta_2 = 0.5$, $\tau_2 = 100s$ (the red dashed curve) in Fig. 5.5 (a); and $\beta_1 = 0.5$, $\tau_1 = 0.01s$ (the black dashed curve) and $\beta_2 = 0.5$, $\tau_2 = 10s$ (the red dashed curve) in Fig. 5.5 (b).

We observe that the critical strain function is characterized by two local maxima (or two peaks) for both cases. Interestingly, the strain rate values (corresponding to the maxima) coincide with those of the single-branch models with corresponding relaxation times. For example, $\dot{\varepsilon}^{p(1)}$ and $\dot{\varepsilon}^{p(2)}$ in Fig. 5.5 (a) is the strain rate corresponding to peaks for the composite with the singe-branch model with $\beta_1 = 0.5$, $\tau_1 = 1s$ and $\beta_2 = 0.5$, $\tau_2 = 100s$, respectively (see the perpendicular dashed gray lines). We also observe that the peak corresponding to the larger relaxation time is higher than the peak corresponding to the shorter relaxation time. In particular, the critical strain is higher for the value corresponding to $\dot{\varepsilon}^{p(2)}$ than the value corresponding to $\dot{\varepsilon}^{p(1)}$ (see the blue curves). This observation indicates that for the double-branch model with the same strain-energy factor ($\beta_1 = \beta_2$), the branch with a larger relaxation time plays a more dominant role in the determination of the critical buckling strain.

Figure 5.6 displays the dependence of the critical strain on strain rate for the composites with matrix characterized by the three-branch model ($M = 3$ in Eq. 2.25) in Fig. 5.6 (a), and the five-branch model ($M = 5$ in Eq. 2.25) in Fig. 5.6 (b). In Fig. 5.6 (a), we show the three-branch model with two cases: $\beta_1 = \beta_2 = \beta_3 = 1$ as well as $\tau_1 = 0.01s$, $\tau_2 = 1\ s$ and $\tau_3 = 100\ s$ (see the blue curve); $\beta_1 = 10$ and $\beta_2 = \beta_3 = 1$ as well as $\tau_1 = 0.01s$, $\tau_2 = 1\ s$ and $\tau_3 = 100\ s$ (see the violet curve). In Fig. 5.6 (b), we study the five-branch model with $\beta_1 = \beta_2 = \beta_3 = \beta_4 = \beta_5 = 1$ as well as $\tau_1 = 0.01s$, $\tau_2 = 0.1\ s$, $\tau_3 = 1\ s$, $\tau_4 = 10\ s$ and $\tau_5 = 100\ s$ (see the pink curve). All the dashed curves denote the results of the single-

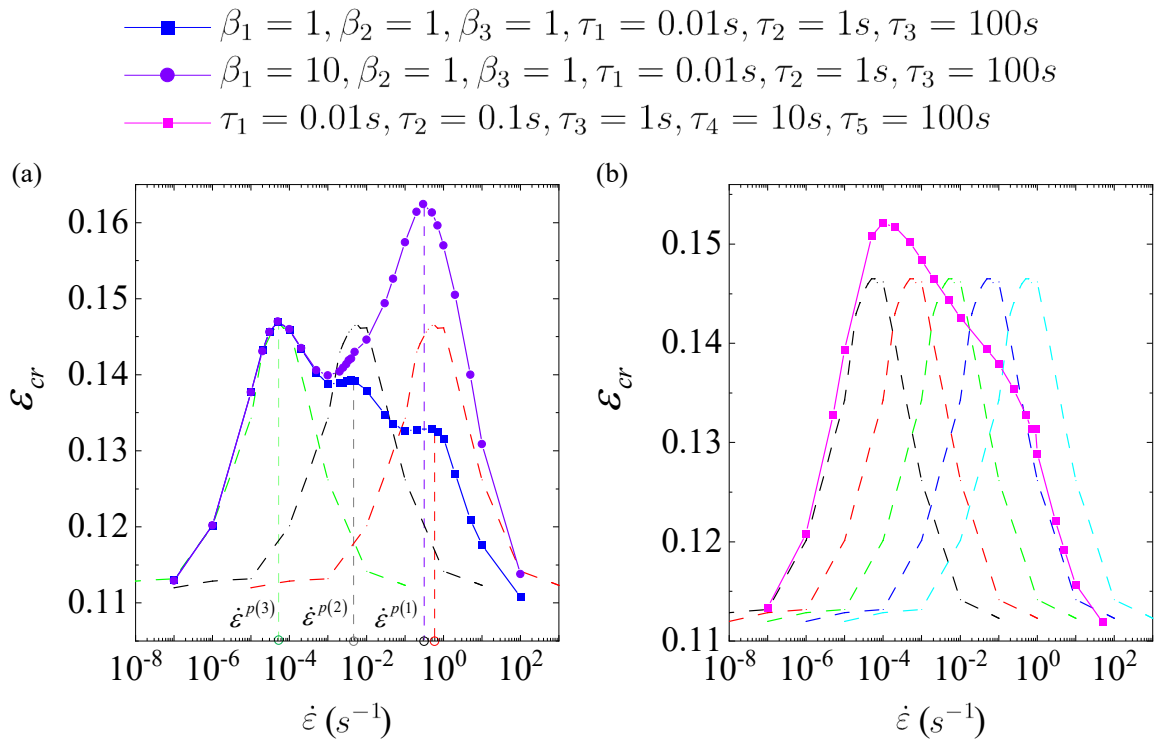

Figure 5.6: The dependence of the critical strain on strain rate for the composites with matrix characterized by (a) the three-branch model and (b) the five-branch model.

branch model with the corresponding strain-energy factor and relaxation time. For instance, the red, gray, and green dashed curves in Fig. 5.6 (a) denote the results with $\beta_1 = 1$ and $\tau_1 = 0.01s$, $\beta_2 = 1$ and $\tau_2 = 1s$ as well as $\beta_3 = 1$ and $\tau_3 = 100s$, respectively.

As expected, the values of the strain rate $\dot{\varepsilon}^{p(\alpha)}$ ($\alpha = 1,\ 2$, and 3) corresponding to the maxima coincide with those of the single-branch models with corresponding relaxation times. In particular, $\dot{\varepsilon}^{p(\alpha)}$ is the strain rate corresponding to peaks for the composite described by the singe-branch model with β_α and τ_α (see the perpendicular green, gray, and red dashed lines in Fig. 5.6 (a)). Similar to the double-branch model, the magnitude of the peak corresponding to the shorter relaxation time is also lower for the three-branch model. In particular, the critical strain corresponding to $\dot{\varepsilon}^{p(1)}$ is lower than the value corresponding to $\dot{\varepsilon}^{p(2)}$ (compare the perpendicular red and gray dashed lines) and the critical strain corresponding to $\dot{\varepsilon}^{p(2)}$ is lower than the value corresponding to $\dot{\varepsilon}^{p(3)}$ (compare the perpendicular gray and green dashed lines). In addition, we note that the critical strain corresponding to the peak increases as the related strain-energy factor increases. For example, an increase of β_1 from one to ten, leads to the corresponding magnitude of the peak increasing from 0.11 to 0.16 (compare the violet and blue curves in Fig. 5.6 (a)). On the contrary, the corresponding strain rate slightly decreases with the increase in β_1 (the perpendicular violet dashed line is the left side of the perpendicular red dashed line). Therefore, the results indicate that a higher strain-energy factor β_α can increase the corresponding local peak and decrease the corresponding strain rate $\dot{\varepsilon}^{p(\alpha)}$. These observations are consistent with the numerical results of the single-branch model. For the single-branch model, the maximum critical strain ε^p_{cr} and the corresponding strain rate increases and decreases with an increase in the strain-energy factor (see the discussion of Fig. 5.3 (b)). Moreover, we find that the increase of the strain-energy factor β_α can even make its adjacent local peak invisible. For example, the

local peaks corresponding to $\dot{\varepsilon}^{p(2)}$ disappear when β_1 increase from one to ten (see the violet curve in Fig. 5.6 (a)).

For the five-branch model, we observe that there is a single peak only (see the pink curve in Fig. 5.6 (b)), and the $\dot{\varepsilon}^p$ almost coincides with the value of strain rate (corresponding to the maximum) of the single-branch model with the largest relaxation time ($\tau = 100\ s$). These observations support the hypothesis that the branch with a larger relaxation time in the multiple-branch model possessing the identical strain-energy factor determines the value of $\dot{\varepsilon}^p$.

5.3 Application of multiple-branch model for 3D-printed soft particulate composite

In this section, we apply the multiple-branch model to capture the instability behavior of the 3D-printed soft particulate composite. To model the 3D-printed soft particulate composite characterized by a broad spectrum of relaxation times [131, 133], Wu et al. [149], [159], we adopt the multiple-branch visco-hyperelastic model.

The composite samples are fabricated with the help of the Objet Connex 260 3D printer. The dimensions of the specimens are $80mm \times 60mm$ (width $\times$ height) with $6mm$ thickness in the out-plane direction. We examine the composites with a single column of inclusions with the spacing ratio $\xi = 0.8$. The height of the primitive unit cell and the diameter of the inclusions are $2.5mm$ and $2mm$, respectively. The soft matrix and stiff inclusions are printed with TangoPlus and VeroBlack, respectively. The stiff inclusions are modeled by incompressible neo-Hookean materials with $\mu^{(i)}/\mu_{\infty}^{(m)} = 10^3$. Based on the dynamic mechanical analysis (DMA) characterization data [163], the TangoPlus material is modeled

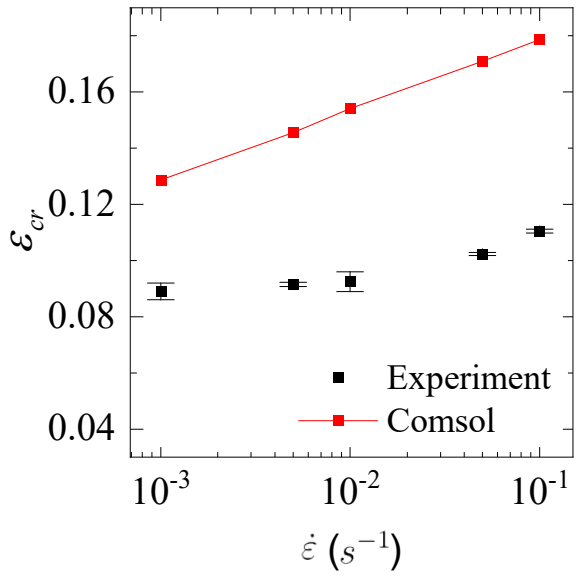

Figure 5.7: The dependence of critical strain on applied strain rate for the single column composite system.

by the multiple-branch visco-hyperelastic model with $M = 10$ in Eq. 2.25. The identified material parameters for the matrix (3D printed in TangoPlus) are provided in Appendix B.5

The in-plane compression tests are carried out by the MTS compression machine at room temperature around 21^oC. The deformation in the thickness direction is restricted by a transparent fixture. The compression is applied at different strain rates: $\dot{\varepsilon} = 10^{-3}s^{-1}$, $5\times10^{-3}s^{-1}$, $10^{-2}s^{-1}$, $5\times10^{-2}s^{-1}$, and $10^{-1}s^{-1}$. At least four samples are tested for each strain rate.

Figure 5.7 shows the dependence of the critical strain on the applied strain rate. In particular, the experimental (the black makers) and numerical (the red curve) critical strain is presented in Fig. 5.7. The critical strain increases with an increase in the strain rate (within the considered loading range). Our simulations also show a similar trend capturing the rate-dependent behavior qualitatively. We note that, here, the critical strain monotonically increases with an increase in the applied strain rate.

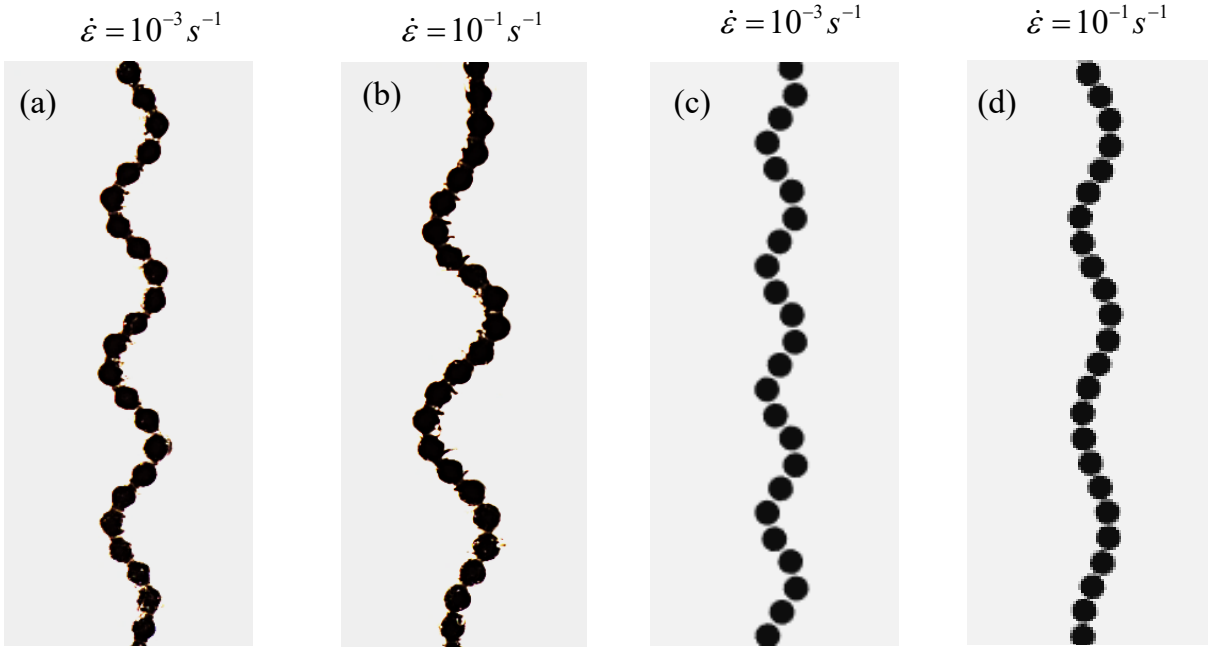

Figure 5.8: (a) Experimental bucking pattern with (a) $\dot{\varepsilon} = 10^{-3}s^{-1}$ and (b) $\dot{\varepsilon} = 10^{-1}s^{-1}$. The simulated bucking pattern with (c) $\dot{\varepsilon} = 10^{-3}s^{-1}$ and (d) $\dot{\varepsilon} = 10^{-1}s^{-1}$ for compressive strain 20%.

Figure 5.8 illustrates the post-buckling patterns observed in experiments (a) and (b), and in simulations (c) and (d). The composite is subject to a compressive strain of 20% with strain rates $\dot{\varepsilon} = 10^{-3}s^{-1}$ (see (a) and (c)) and $\dot{\varepsilon} = 10^{-1}s^{-1}$ (see (b) and (d)). In experiments, we observe that the critical wavelength increases with an increase in the applied strain rate (see (a) and (b)). In particular, the normalized critical wavelengths are $\bar{l}_{cr} = 6$ and 8 for $\dot{\varepsilon} = 10^{-3}s^{-1}$ and $10^{-1}s^{-1}$, respectively. Our simulations also predict a similar increase in the critical wavelength, as illustrated in (c) and (d). The numerical prediction of the normalized critical wavelengths for $\dot{\varepsilon} = 10^{-3}s^{-1}$ and $10^{-1}s^{-1}$ are $\bar{l}_{cr} = 5$ and 8, respectively.

The modeling overestimates the critical strain (see Fig. 5.7) and the predicted post-buckling patterns do not perfectly match the experiments. In particular, the numerical wavelength is smaller than that of experiments for $\dot{\varepsilon} = 10^{-3}s^{-1}$ and the predicted buckling

amplitude is visibly smaller than that of the experimental pattern for $\dot{\varepsilon} = 10^{-1}s^{-1}$ for the same compressive strain level, 20% (see Fig. 5.8). The difference between the numerical and experimental results may be attributed to multiple reasons, such as possible damage occurring in materials during deformation [80, 151, 169] and the friction in the experiment setup, among other factors. Moreover, the material parameters are extracted from the DMA that characterize the material properties in the small deformation range. In the experiments, however, the composite experience high-level deformations (especially the matrix material in the area between the inclusions). In addition, the high-level deformations could cause stiffening behavior of the polymeric materials [8, 34, 49, 151]. However, in our numerical simulation, the equilibrium and instantaneous responses of the matrix material are described by the neo-Hookean model which is unable to capture the stiffening behavior in the deformation process accurately. We also note that the interphase formed in the 3D-printing process may also influence the instabilities in soft composites [5]. Furthermore, the composite buckling behavior may be affected by the imperfections or uncertainties in materials [62, 63, 122] or geometry [29, 37, 161] of composite. The influence of uncertainties can be quantified and implemented into the numerical framework through stochastic analysis [42, 100].

5.4 Concluding remarks

We examined the buckling of the visco-hyperelastic particulate composite with the matrix material described by the visco-hyperelastic model. We started by considering the dependence of the critical strain and wavelength on the applied strain rate in the composite with the matrix characterized by the single-branch visco-hyperelastic model. We found that the stress-strain response of the composites (subjected to compression with a constant strain rate) is identical (both before and after buckling) for a given Weissenberg number regardless

of the relaxation time, although the local deformation history varies significantly. We observed that the critical strain was not monotonically dependent on the applied strain rate. In particular, the critical strain increases first, then reaches its maximum value at a certain strain rate, and finally decreases with an increase in strain rate. Additionally, we noted that the Weissenberg number (corresponding to the maximum of critical strain) sightly decreased with an increase in the strain-energy factor (instantaneous shear modulus). In addition, the critical wavelength was also found to be non-monotonically depending on the applied strain rate. The critical wavelength shows an increasing trend with an increase in the instantaneous shear modulus.

The dependence of the critical strain on the strain-energy factor can be explained in terms of inclusion-to-matrix shear modulus contrast. In particular, the instantaneous shear modulus of the matrix increases with the increase in the strain-energy factor. As a result, the instantaneous inclusion-to-matrix shear modulus contrast decrease with an increase in the strain-energy factor. Accordingly, the corresponding critical strain shows an increasing trend. However, the rate dependence of the critical strain cannot be fully explained based on the modulus contrast. The instantaneous modulus of the visco-hyperelastic matrix monotonically increases with the increase in strain rate. Therefore, if we consider the influence of strain rate on the effective modulus contrast only, the critical strain will monotonically increase with an increase in the applied strain rate; and critical strain will be bounded by the critical buckling strain at the extremely slow and fast loadings. However, the critical strain shows a non-monotonic strain rate dependence. This observation hints at a more complex buckling behavior stemming from the viscoelasticity of the particulate composite. An important component of the complexity is the spatial inhomogeneity of deformation (and rate of deformation). As a result, the estimates based on the rate-dependent instantaneous

modulus may not be accurate.

We further explored the instability behavior of the composites with the matrix characterized by a multiple-branch visco-hyperelastic model. We found that the critical strain versus the applied strain rate curve obtained by the M-branch model tends to have an M number of local maxima (peaks). The strain rates corresponding to the local maxima coincide with those obtained by the single-branch models with the corresponding relaxation times. The branch with the larger relaxation time can significantly affect the local peaks and even make other peaks (with shorter relaxation time) invisible. The local maximum can be significantly increased by increasing the corresponding strain-energy factor. Therefore, the branch with a larger strain-energy factor can significantly influence the rate dependence behavior of the critical strain.

Finally, we experimentally studied the buckling of the 3D-printed soft particulate composite. The 3D printed matrix material (TangoPlus) used in experiments is characterized by a broad spectrum of relaxation times. Therefore, the multiple-branch visco-hyperelastic model is adopted in numerical simulations for the corresponding matrix. The experimental critical strain and wavelength increase with an increase in the applied strain rate, and the numerical modeling can qualitatively capture the rate dependence of the critical strain and wavelength.

Our results provide insights into the complex role of viscoelasticity in the buckling behavior of soft composites. The results can be helpful for the design of soft metamaterial. In particular, the instabilities combined with viscoelasticity can be used to design metamaterials with novel properties that pure elastic metamaterials cannot achieve. For example, viscoelastic metamaterials can show seemingly contradictory behavior - positive and negative Poisson's ratio, by applying different strain rates [22, 71]. Technically, we can tailor

the properties of the soft metamaterials by regulating their viscoelasticity. In practice, the viscoelasticity of soft materials can be tuned by adjusting the temperature and scanning light intensity in the 3D printing process [149, 150]. In addition, the electric [1], magnetic [53, 117, 125], and thermal loading [27, 162] can be remotely applied to control the rate-dependent behavior. Therefore, the mechanical properties can be tuned remotely by programmable external stimuli.

CHAPTER 6

TUNABLE MECHANICAL BEHAVIORS OF VISCO-HYPERELASTIC PARTICULATE COMPOSITE THROUGH BUCKLING*

Yuhai Xiang, Dean Chen, Stephan Rudykh

*(*Prepared for submission to a journal)*

Through numerical simulation, we demonstrate that we can tune the dynamic modulus and damping by pre-compress the particulate composites with different strain rates. We show that the tunability of the dynamic mechanical properties stems from the rate-dependent critical buckling strain. Moreover, we observe that the dynamic negative stiffness of the composites after buckling is triggered when the applied strain rate is below a certain value. Furthermore, we observe that the rate dependence of the energy absorption under large deformation for particulate composites is quite different from that for homogeneous materials. For slow loading rates, the particulate composite shows a higher capability than homogeneous materials to absorb energy. As the applied strain rates increase, the energy absorption capability of homogeneous materials surpasses that of particulate composites in the intermediate loading rate regime. With a further increase in the strain rate into the high loading rate regime, homogeneous materials and the composite show similar abilities to absorb energy.

6.1 Introduction

Instabilities in soft microstructured materials leading to dramatic pattern transformation [82] are exploited to design materials with tunable and target properties, such as tunable

bandgap material [87, 126, 146], auxetic material [16, 86, 110], the materials with negative viscoelasticity [71] and tunable stiffness [101].

The framework of small perturbations superimposed on finite deformation [115] is frequently employed to detect the onset of instability in soft materials. In composites, the instability may develop at macroscopic and microscopic scales [50]. Macroscopic instabilities (longwave instabilities) can be detected with loss of ellipticity analysis which requires evaluating the effective tensor of elastic moduli. The effective tensor of elastic moduli can be calculated either through phenomenological models [103, 104, 105, 106, 107] or the micromechanics-based homogenization approaches [2, 35, 60, 95, 96, 127]. For microscopic instabilities, Bloch-Floquet analysis is widely used to identify the onset of buckling [5, 46, 48, 85, 87, 90, 114, 132, 136, 138].

The pioneering work on both microscopic and macroscopic instability of the particulate composites was reported by Triantafyllidis et al. [137] who investigated the instability of the compressible neo-Hookean porous and rigid particulate composites under biaxial plane compression. Michel et al. [108] examined the microscopic and macroscopic instability of the particulate composites with different particle distribution, particle volume fraction, the matrix's constitutive model and the particles' shape. Li et al. [83] observed the microstructure transformation induced by elastic instabilities in particulate composites in experiments. Chen et al. [28] extensively examined the buckling pattern in soft particulate composites via numerical simulation. Most recently, Xiang et al. [153] explored the rate-dependent critical strain and wavelength in soft visco-hyperelastic particulate composites.

The majority of the studies on particular composites focus on *purely* elastic or hyperelastic materials. However, the influence of instability together with viscoelasticity on the mechanical behavior of the particulate composite is less reported. Most soft composites are

fabricated with a polymeric material that possesses strong viscoelasticity [133, 150, 151]. Therefore the instabilities and the corresponding mechanical behavior in the soft particulate composite are expected to be significantly affected by the applied strain rate.

The present work studies the non-linear mechanical behavior induced by the instability of visco-hyperelastic particulate composites. First, we study the dynamic mechanical properties of the pre-strained composites. Then, we examine the stiffness of buckled composites. Finally, we investigate the energy absorption of composites undergoing finite deformation for different applied strain rates. Our numerical results demonstrate that the instability coupled with viscoelasticity can provide an opportunity to tune material properties.

6.2 Results

We start with investigating the effect of the pre-strain and the rate of the pre-strain on the dynamic modulus $|E^*|$ and loss factor (damping) $tan\delta$. In particular, we calculate the dynamic mechanical properties under the pre-strain state. Firstly, we load the particulate composite to the pre-strain ε_0 with a certain dimensionless strain rate Wi ($t < t_0$). Then we hold the particulate composite at the pre-strain ε_0 until relaxing to the equilibrium state ($t_0 < t < t_d$). Finally, we employ the cyclic loading on the pre-strained composites to obtain the dynamic mechanical properties ($t_d < t < t_f$). The details for the determination of the dynamic mechanical properties are given in Appendix B.4.

Figure 6.1 shows the dynamic modulus ((a) and (c)) and loss factor ((b) and (d)) for composite one ((a) and (b)) and two ((c) and (d)). We demonstrate the dependence of dynamic mechanical properties on the strain rate (Weissenberg number) in the pre-strain process ($t < t_0$) for different pre-strain ε_0 ranging from 0 to 0.16. For homogeneous viscoelastic materials, the dynamic mechanical properties are independent of strain rate in the pre-strain

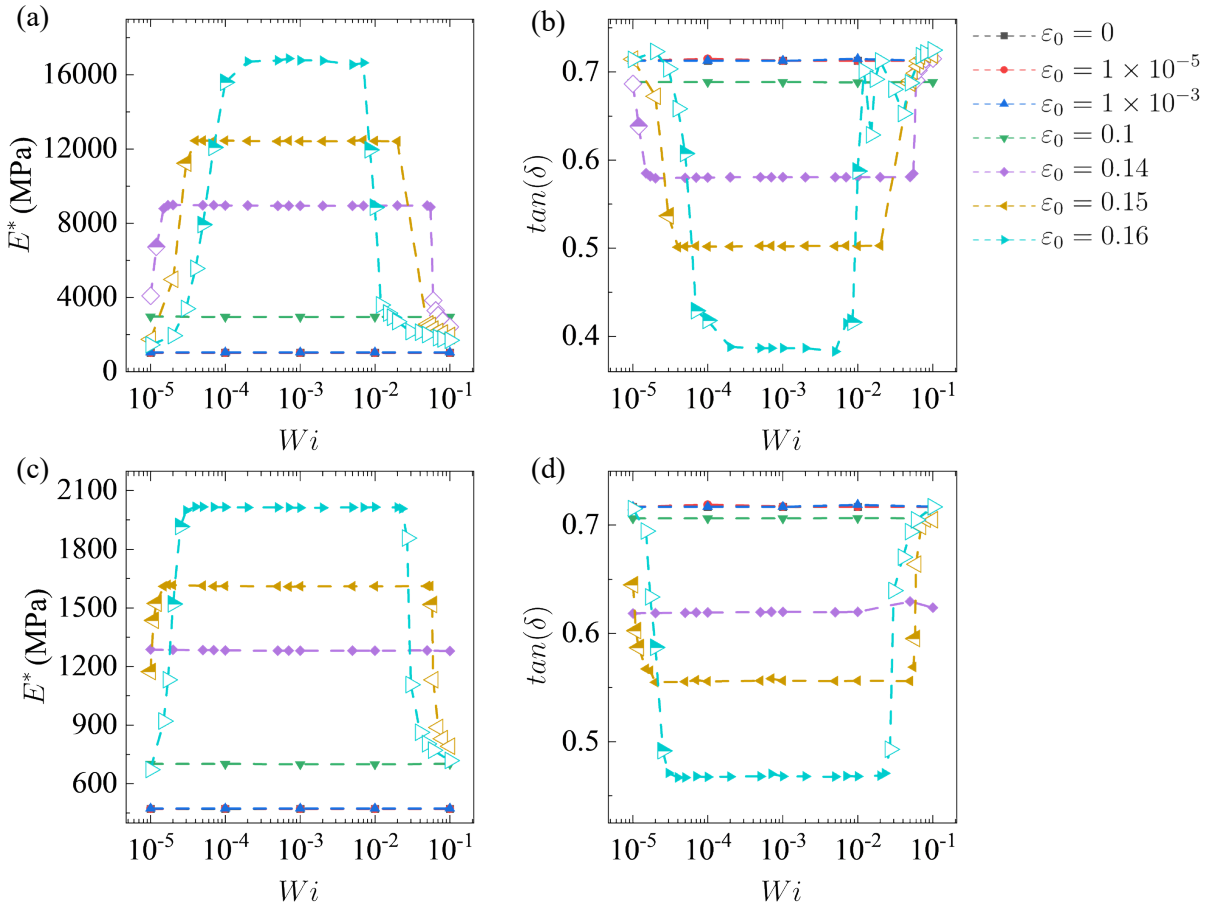

Figure 6.1: (a) The dependence of the dynamic modulus and (b) loss factor on pre-strain rate for composite one; (c) The dependence of the dynamic modulus and (d) loss factor on pre-strain rate for composite two with different pre-strain ε_0.

loading process for any value of the pre-strain ε_0. However, for this particulate composite, one can observe that there exists a threshold strain ε_{cr}^{th}. The dynamic mechanical properties are indifferent to the strain rate in the pre-strain loading process for $\varepsilon_0 < \varepsilon_{cr}^{th}$. Conversely, the dynamic mechanical properties are highly dependent on the strain rate in the pre-strain loading process for $\varepsilon_0 \geq 0\varepsilon_{cr}^{th}$. For $\varepsilon_0 < \varepsilon_{cr}^{th}$, the dynamic modulus increase with the increase in pre-strain. However, the loss factor shows the opposite trend (see the black, red, dark blue, and green curves in (a) and (b); see the black, red, dark blue, green and violet curves in (c) and (d)). The threshold strain ε_{cr}^{th} are around 0.14 and 0.15 for composite one and two, respectively. For composite one, different strain rates in the pre-strain process may result in distinct dynamic mechanical properties when $\varepsilon_0 \geq 0.14$. For instance, when $\varepsilon_0 = 0.16$, the dynamic modulus increases first, then reaches a plateau, and finally it decreases with the increase in strain rate, while the loss factor shows the opposite dependence on strain rate (see the light blue curves in (a) and (b)). The dynamic mechanical properties of composite two show similar rate dependence as composite one for $\varepsilon_0 \geq 0.15$ (see the light blue and brown curves in Fig. 6.1 (c) and (d)).

To interpret the rate-dependent dynamic mechanical properties, we show the rate-dependent critical strain of the composite one in Fig. 6.2 (a) and illustrate the dynamic modulus of the composite one with $\varepsilon_0 = 0.16$ in Fig. 6.2 (b). The details to obtain the rate-dependent critical strain are given in Appendix B.2 When we load the composites relatively slower (such as $Wi = 10^{-5}$) and faster (such as $Wi = 0.1$) (see the vertical dashed black lines), ε_0 is larger than the corresponding critical strain. As a result, buckling occurs. Once bucked, the microstructure pattern is dramatically transformed. However, for intermediate strain rates such as $Wi = 10^{-3}$ (see the vertical dashed gray line), the ε_0 is smaller than the corresponding critical strain, so buckling does not appear. As the different microstructure patterns are

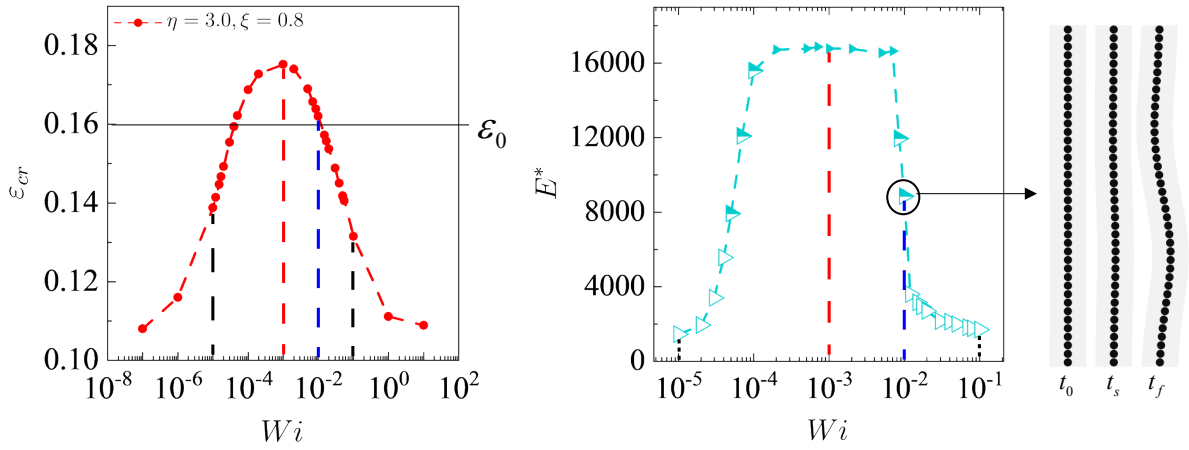

Figure 6.2: (a) Rate-dependent critical strain for composite one. (b) The dependence of dynamic modulus of composite one (subjected to the pre-strain $\varepsilon_0 = 0.16$) on strain rate. (c) Illustration of a case where buckling patterns are activated by the cyclic loading.

triggered by different pre-strain rates, we can expect that the dynamic mechanical properties should depend on the loading rate in the pre-strain loading process. We can observe that the dynamic modulus corresponding to $Wi = 10^{-5}$ and 0.1 is significantly lower than the value corresponding to $Wi = 10^{-3}$ (compare the values corresponding to dashed black and gray lines in (b)). We use the hollow markers to represent the cases where the instability has already occurred (this rule is also applied for makers in Fig. 6.1 (a)-(d)).

In addition, we note that for some pre-strain rates, such as $Wi = 10^{-2}$ (see the vertical dashed blue line), the pre-strain is slightly smaller than the critical strain, so the buckling does not occur in the pre-loading process, but we observe that the buckling pattern is activated in the cyclic loading process. In particular, we show the microstructure of composite one undergoing $Wi = 10^{-2}$ at t_0, t_s and t_f in Fig. 6.2 (c). We note that the buckling does not appear at t_0 and t_s, but appears at t_f. We use the half-hollowed markers to represent the cases where the buckling is activated in the cyclic loading process in Fig. 6.1 (a)-(d). One can observe that the dynamic mechanical properties (corresponding to the cases where the

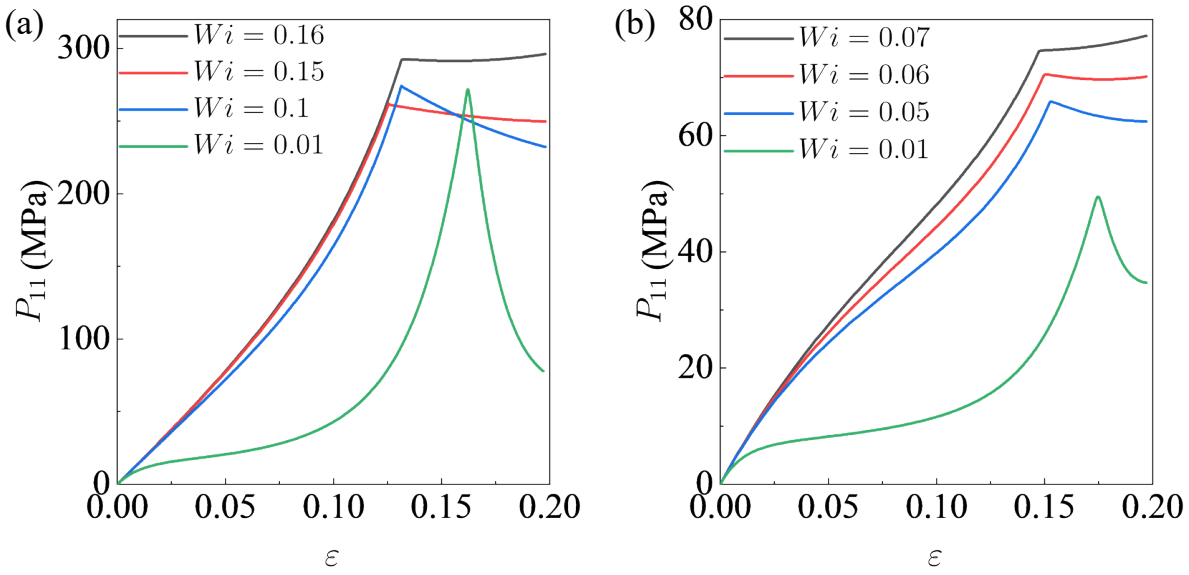

Figure 6.3: The stress-strain curves for (a) composite one undergoing Wi=0.01, 0.1, 0.15 and 0.16 and (b) composite two undergoing Wi=0.01, 0.05, 0.06 and Wi=0.07.

buckling is activated in the cyclic loading phase) are different from the values for the cases where there is no buckling for the whole loading process (compare the filled and half-hollowed markers in Fig. 6.2 (b)).

Next, we examine the stiffness of the composites after buckling. Figure 6.3 shows the first Piola-Kirchoff stress component P_{11} versus the applied strain ε for the composite one (a) and two (b). We illustrate the results of the composite one under Wi range from 0.01 to 0.16 in (a); as well as composite two under Wi range from 0.01 to 0.07 in (b). We note that the stress response (especially in the post-buckling regime) dramatically depends on the strain rate. In particular, we find that below a certain Weissenberg number Wi_c, discontinuous buckling can be observed. Discontinuous buckling is a case where the post-buckling stiffness is negative [32]. Specifically, Wi_c is around 0.16 and 0.07 for the composite one and two, respectively. Namely, the stiffness of the composite one and two right after buckling are

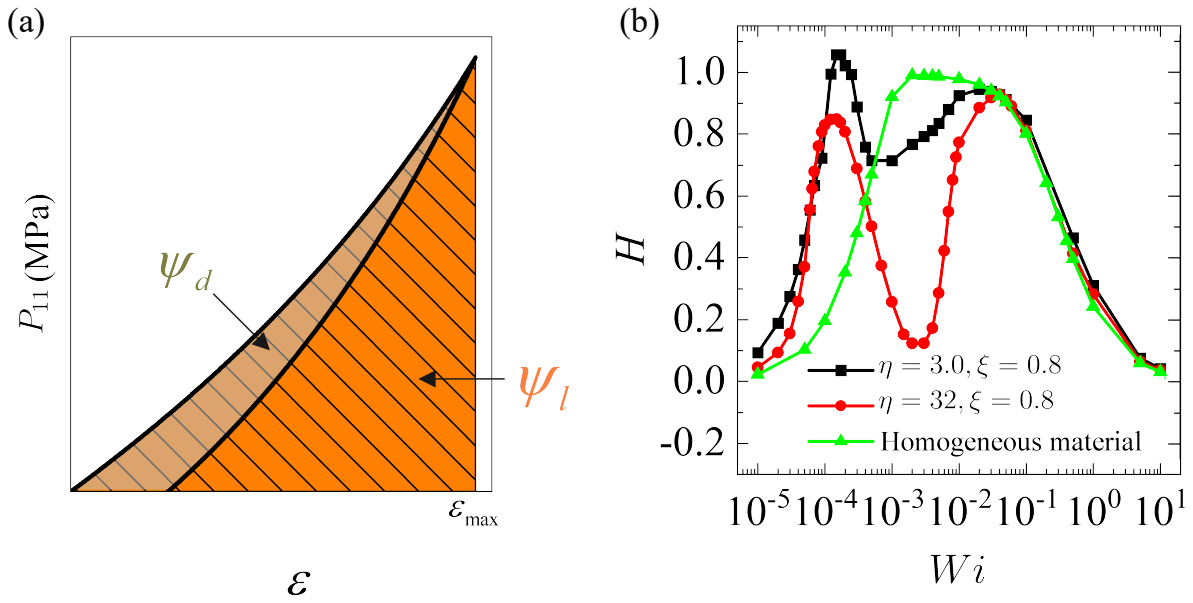

Figure 6.4: (a) Illustration of the dissipated energy and the applied work per unit volume in one cycle; (b) the dependence of relative hysteresis of the particulate composites and homogeneous viscoelastic materials on strain rate.

negative when Wi is smaller than 0.16 and 0.07, respectively (see the red, blue and green curves).

Finally, we explore the dependence of energy absorption capability under finite deformation on strain rate. In Fig. 6.4 (a), we illustrate the stress-strain response undergoing loading and unloading path with a certain constant value of dimensionless strain rate Wi (see the black curve in (a)). The capability of the energy absorption is characterized by the relative amount of hysteresis, H, which is defined as ψ_d/ψ_l [38]. Here ψ_d is the energy dissipated per unit volume during the loading and unloading path (see the shaded gray area in Fig. 6.4 (a)) and ψ_l is the amount of applied work per unit volume during the loading phase only (see the orange slash area in Fig. 6.4 (a)). For a given Wi, we can calculate the corresponding relative hysteresis. Accordingly, the rate dependence of the hysteresis can be obtained.

In Fig. 6.4 (b), we show the rate dependence of hysteresis for the composite one (black curve) and two (red curve), as well as the homogeneous viscoelastic material (green curve). Here the homogeneous viscoelastic material represents the material that only consists of the matrix material of the particulate composite. We focus on the cases where the maximum applied strain ε_{max} is sufficiently large to trigger the instabilities in the particulate composites. In these cases, the rate dependence of the relative hysteresis in composites is quite similar for different maximum applied strains ε_{max}. Thence, $\varepsilon_{max} = 0.25$ is taken as an example for quantitative comparison.

We note that relative hysteresis for the particulate composites shows different rate-dependent behavior compared with homogeneous material. In particular, relative hysteresis for particulate composites shows two local maxima while there is just one maximum for homogeneous material. One can observe that the relative hysteresis of the homogeneous material is higher than that of particulate composites for the intermediate value of loading rates. In particular, the hysteresis of homogeneous material is higher than that of the composite one and two for $5\times10^{-4} < Wi < 0.04$ and $4\times10^{-4} < Wi < 0.04$. For relatively slower loading rates, such as $Wi < 5\times10^{-4}$ (or $< 4\times10^{-4}$) for composite one (or two), the hysteresis of the homogeneous material is lower than that of the particulate composites. For $Wi > 0.4$, the relative hysteresis of the two types of composites and homogeneous material is similar.

We find that the minimum value (between two peaks) of the relative hysteresis is smaller for the composites with a high periodicity aspect ratio η. By contrast, dimensionless strain rate Wi (corresponding to the minimum value between two peaks) increases with the increase in periodicity aspect ratio (compare the black and red curves). In particular, the minimum values (between two peaks) of the relative hysteresis are around 0.669 at $Wi = 5\times10^{-4}$ and

around 0.123 at $Wi = 3\times10^{-3}$ for composite one and two, respectively. In addition, the relative hysteresis of composite one is higher than that of composite two when Wi ranges from 1.5×10^{-4} to 0.04. For $Wi < 1.5\times10^{-4}$, the relative hysteresis of composite one is still larger than that of composite two for $1\times10^{-5} < Wi < 6\times10^{-5}$. Otherwise, the opposite is true.

6.3 Conclusions and Discussions

We explore the buckling-related mechanical behavior of particulate composites under large deformation. First, we investigate the dynamic modulus and loss factor of composites under the pre-compression state. We observe that the pre-strain rate can result in distinct dynamic mechanical properties even for the same pre-compression strain when the pre-strain is higher than a threshold strain. Therefore, we can tune the dynamic mechanical properties of the composite by tuning the pre-loading velocity.

Next, we study the post-buckling stress-strain response and find that the negative stiffness in the post-buckling regimes appears when the Weissenberg number is below a specific value, demonstrating that the viscoelasticity can sharply alter the post-buckling mechanical response of the composite. We can tailor the post-buckling stiffness by selecting the appropriate relaxation time to enable the applied Weissenberg number to be within the required value range.

Finally, we explore the energy absorption under large deformation; the capability of the energy absorption can be tuned by changing the geometric parameters. The rate dependence of relative hysteresis of particulate composites shows a sharp distinction from that of the homogeneous material. In particular, the hysteresis versus strain rate curve has a mono maximum for homogeneous material, while it has two peaks for particulate composites.

The energy absorption capability of particulate composites is lower (higher) than that of homogeneous material for intermediate (relatively low) dimensionless strain rate. We can adjust the energy absorption capability by selecting geometric parameters and relaxation time. The relaxation time is selected to make the applied dimensionless strain rate Wi in the required range.

Theoretically, the relaxation time of polymeric material is connected to the microscopic quantities of the polymer chain, such as the length and diffusion of the free chains (Xiang et al., 2019; Ying et al., 2016). Therefore, the relaxation time can be controlled by changing the microscopic physical quantities. In practice, we can tune the microscopic quantities by adjusting the manufacturing parameters, such as the light intensity or temperature in the process of 3D printing (Wu et al., 2018; Xiang et al., 2020a).

CHAPTER 7

CONCLUSIONS AND PERSPECTIVES

This dissertation focused on the interplay between viscoelasticity and instability in two types of soft composites: soft particulate and laminated composites. Through numerical simulation, experiment, and theoretical analysis, we have a deeper understanding of the buckling in soft visco-hyperelastic composites and demonstrate that the combination of viscoelasticity and instability can be employed to tune the mechanical behavior of the soft composites, such as the dynamic mechanical properties and energy absorption.

We close the dissertation by presenting several prospective research in the future.

1. More fundamental experiments could be carried out to further verify our numerical results. For example, the soft material described by the single-branch visco-hyperelastic model can be synthesized. So that the rate-dependent properties predicted in our simulations could be validated.

2. To our knowledge, a general theoretical framework to identify the critical strain and wavelength onset of instability in visco-hyperelastic periodical composites is still absent. Further efforts in the theoretical aspects would help us better understand the interaction between viscoelasticity and instability.

3. The instabilities in hyperelastic magnetoactive composites have been extensively explored [54, 72, 117, 125, 165]. Yet the instability in viscoelastic magnetoactive composites remains unexplored.

4. To date, the viscoelasticity has only been explored in simple structures such as particulate composite and laminates. The role of viscoelasticity in the mechanical metamaterials with more intricated geometry remains overlooked.

5. The majority of the studies investigate the strain rate dependence of the instabilities in

viscoelastic composites; However, few studies focus on the influence of temperature [27, 26]. The combination of the applied strain rate and temperature may expand the design space of soft composites/metamaterials.

APPENDIX A

SUPPLEMENTARY INFORMATION: VISCO-HYPERELASTICITY OF PHOTOCURED POLYMERS

A.1 Dimensions of specimens

The dimensions of the specimens are shown in Fig. A.1.

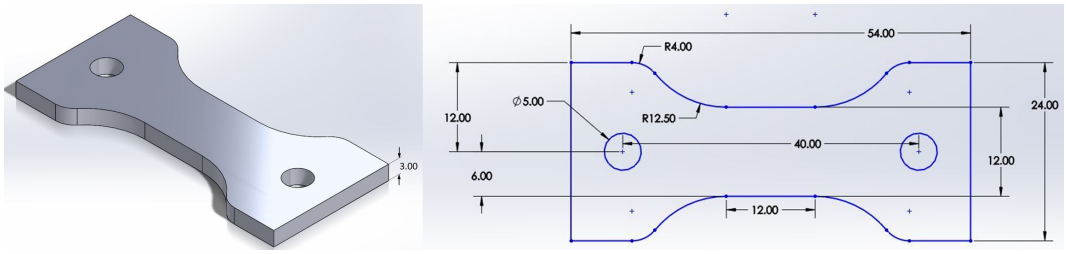

Figure A.1: The dimensions of a specimen (Unit: mm).

A.2 The viscosity of dangling chains

To obtain the nonlinear viscosity of dangling chains in Sec. 3.3.2, here, we briefly illustrate the relation between the viscosity of dangling chains and deformation. Different from the free chains, the reptational motion of dangling chains is suppressed by their crosslinked ends. Arm retraction, as the relaxation mechanisms for arm polymers, is also responsible for the stress relaxation of dangling chains [11, 24, 33, 143, 144], therefore, the rate-dependent behaviors of the star arms and dangling chains are equivalent [24, 33, 55, 143]. Here we introduce the theory of Pearson and Helfand [118], the viscosity η_0 of the arms of star polymer in this work is expressed as

$$\eta_0 = G_e \frac{\zeta L_{eq}^2}{2\Upsilon k_B T} \left(\frac{\pi}{\gamma}\right)^{1/2} \exp(\Upsilon)/2\Upsilon \tag{A.1}$$

where ζ is the friction coefficient of the polymer chains, and Y can be written as

$$Y = v' \left(\frac{M}{M_e} \right) = \frac{4}{5} \frac{Nb^2}{d^2} v' \tag{A.2}$$

where M is the molecular weight of an arm; M_e is the molecular weight between entanglements; v' is estimated as 0.6 [118]; N is the number of the Kuhn monomers of an arm; d is the tube diameter, wherein the arms are confined; b is the length of the Kuhn monomers; L_{eq} is the equilibrium contour length of an arm, which can be expressed by Edwards [40] as

$$L_{eq} = \frac{M}{M_e} d = \frac{4Nb^2}{5d} \tag{A.3}$$

where G_e is the plateau modulus, which can be expressed as [40, 158]

$$G_e = \frac{\rho RT}{M_e} = n k_B T \frac{4Nb^2}{5d^2} \tag{A.4}$$

where ρ is the mass density of arms, R is the molar gas constant, n is the chain number density of arms. Here we assume that the tube diameter of an arm d have a similar evolution relationship with deformation as free chains, thus, d can be expressed as [170]

$$d = \alpha(\mathbf{F}) d_0 \tag{A.5}$$

where $\alpha(\mathbf{F})$ is expressed as the Eq. 3.16 in Sec. 3.3.2, d is the tube diameter of the arm under reference configuration. Hence, Eq. A.1 can be rewritten as

$$\eta_0 = \eta' \alpha(\mathbf{F}) \exp \left(\frac{\Gamma'}{\alpha(\mathbf{F})^2} \right) \tag{A.6}$$

where,

$$\eta' = \left(\frac{4\Gamma}{5}\right)^{-1/2} \frac{b^2 n N \sqrt{\pi}\zeta}{5\left(v'\right)^{5/2}}$$
$$\Gamma' = \frac{12}{25}\frac{Nb^2}{d_0^2} \tag{A.7}$$

The Eq. A.6 can be directly applied to Sec. 3.3.2.

APPENDIX B

SUPPLEMENTARY INFORMATION: INSTABILITIES IN VISCO-HYPERELASTIC SOFT COMPOSITES

B.1 Weissenberg number in laminates

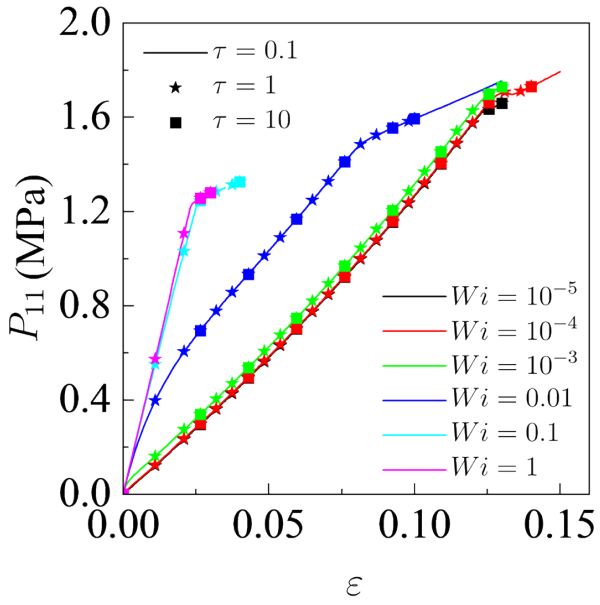

Figure B.1: The nominal stress versus the applied strain for diverse Weissenberg numbers with different relaxation times.

Weissenberg number is defined as $Wi = \dot{\varepsilon}\tau$, which is usually used as the dimensionless "loading rate". In homogeneous material and even particulate composite (see Sec. 5.2.1), the mechanical response will be identical for the same Weissenberg number regardless of the relaxation time. Here, we justify the Weissenberg number as the dimensionless loading rate for laminate composite. As illustrated in Fig. B.1, we show the nominal stress versus the strain for different Wi with different relaxation times. In particular, we applied $Wi = 10^{-5}$

(black), $Wi = 10^{-4}$ (red), $Wi = 10^{-3}$ (green), $Wi = 0.01$ (blue), $Wi = 0.1$ (cyan) and $Wi = 1$ (pink) to the laminate structure with relaxation time $\tau = 0.1s$ (solid curve), $\tau = 1s$ (star markers) and $\tau = 10s$ (square markers). We can observe that the mechanical response is identical for the same Wi in defiance of the relaxation time.

B.2 The identification procedures for critical strain

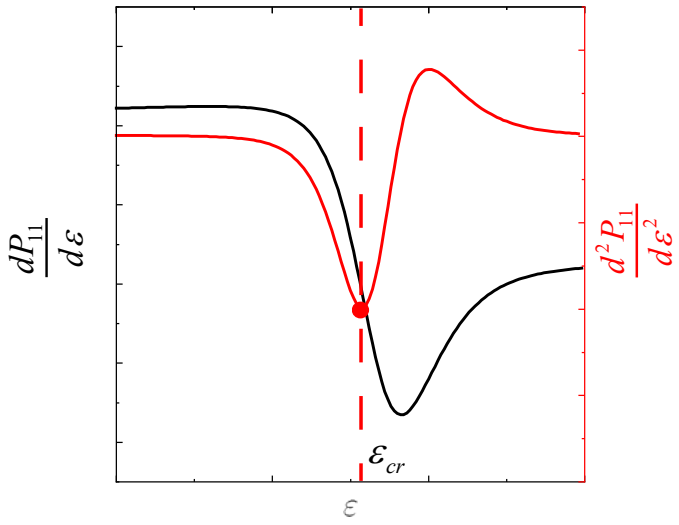

Figure B.2: The illustration of the determination of critical strain.

Here, we show the procedures for identifying the critical strain. Based on the simulation, we calculate the first derivative ($\frac{dP_{11}}{d\varepsilon}$, black curve) and second derivative ($\frac{d^2P_{11}}{d\varepsilon^2}$, red curve) of the nominal stress with respect to the applied strain ε (see Fig. B.2). The second derivation $\frac{d^2P_{11}}{d\varepsilon^2}$ is utilized to identify the critical strain. In particular, in regions where the $\frac{dP_{11}}{d\varepsilon}$ sharply changes the value with the change in ε, ε corresponding to the minimum value of $\frac{d^2P_{11}}{d\varepsilon^2}$ is identified as ε_{cr} (see the red point in Fig. B.2).

B.3 The identification procedures for wavelength for laminates

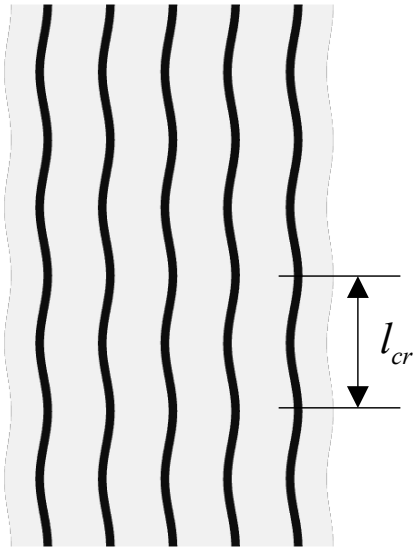

Figure B.3: The identification of the critical wave number

Here, we show the procedures for the identification of the wavenumber for laminates. We take a laminate structure with $v^f = 0.12$ undergoing $Wi = 10^{-4}$ as an example. To obtain the critical wavenumber, we employ the Fourier transformation on the displacement U_2 of the fiber onset of the buckling. U_2 is depicted in Fig. B.3 (a) and we note that the buckling pattern of the laminates is closer to the trigonometric functions compared with the bucking pattern of particulate composites. Therefore, the result of Fourier transformation has more shape peaks, as shown in Fig. B.3 (b). The corresponding buckling pattern is illustrated as an inset in (b). The wavenumber with the dominant magnitude is identified as the critical wavenumber k_{cr}.

B.4 Determination of the dynamic modulus and loss factor

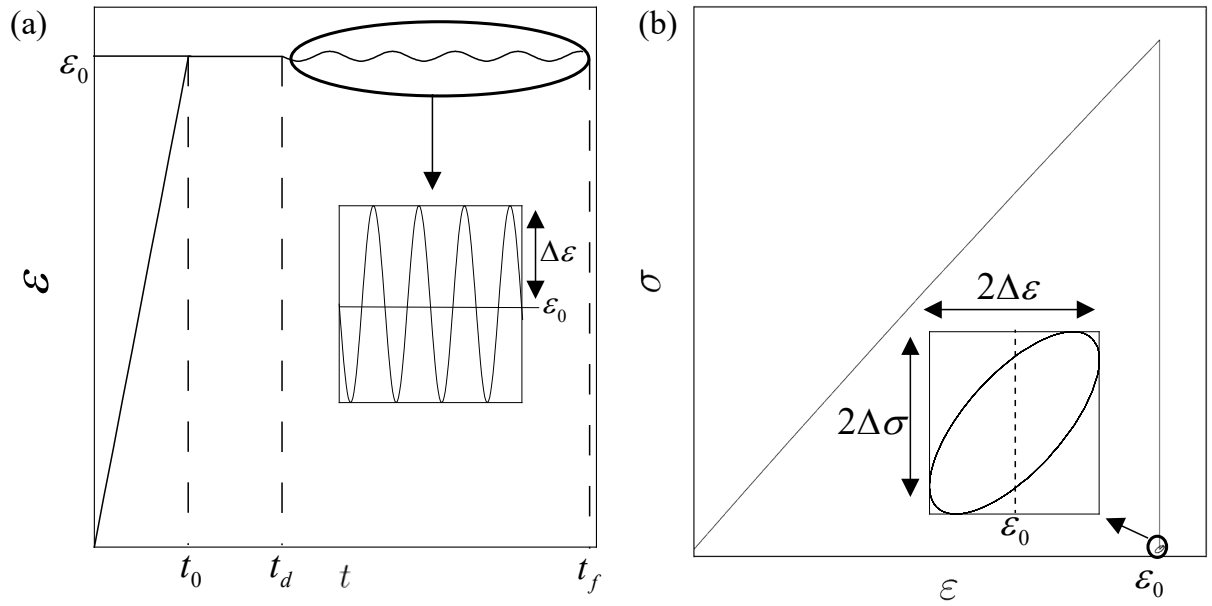

Figure B.4: (a) The applied strain versus the time and (b) stress versus strain for the whole loading process.

Here, we show the procedure to evaluate dynamic mechanical properties through simulations. The dynamic mechanical properties are characterized by dynamic mechanical analysis (DMA). To simulate the dynamic mechanical properties, the oscillatory loading, as illustrated in Fig B.4 (a), is prescribed as

$$\varepsilon(t) = \begin{cases} \varepsilon = \dot{\varepsilon} t \quad t < t_0 \\ \varepsilon = \varepsilon_0 \quad t_0 < t < t_d \\ \varepsilon = \varepsilon_0 + \Delta\varepsilon \sin(2\pi f t) \quad t_d < t < t_f \end{cases} \tag{B.1}$$

where $\dot{\varepsilon}$ is the applied strain rate, t_0 is the loading time to reach the pre-strain ε_0. t_d and t_f are the time of starting and ending of the oscillatory loading, respectively. To ensure the

composite relaxes to the equilibrium state before the cyclic loading, we set $t_d = t_0 + 40\tau$. f and $\Delta\varepsilon$ are the frequency and amplitude of the cyclic applied strain. To only consider the effect of pre-strain and rate of pre-strain, we fix the value of f and $\Delta\varepsilon$ as 1 Hz and 10^{-5}, respectively. The typical stress and strain curve is illustrated in Fig B.4 (b). The stress gradually relaxes to the equilibrium state as holding the strain as ε_0. Subsequently, the hysteresis loop curve (see the inset in Fig B.4 (b)) is produced by the harmonic loading due to the viscoelasticity.

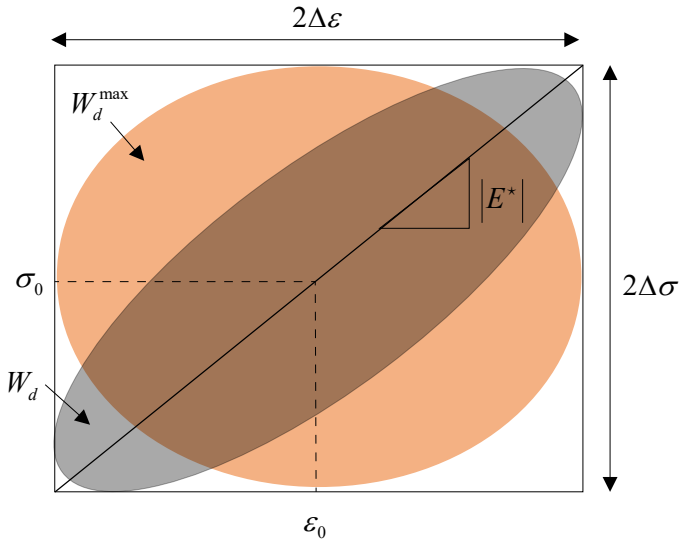

Figure B.5: Stress versus strain under oscillatory loading. Illustration of slope $|E^*|$, dissipated and the maximum dissipated energy for a full cycle.

To get the dynamic modulus and loss factor under the pre-strain state, the final hysteresis loop of the cyclic loading is utilized [3, 78], as illustrated in Fig. B.5. The cyclic stress response can be expressed as

$$\sigma(t) = \Delta\sigma \sin(2\pi f + \delta) + \sigma_0 \tag{B.2}$$

where $\Delta\sigma$ is the amplitude of the stress, δ and is the phase difference between the strain and the stress due to the viscoelasticity. σ_0 is the equilibrium stress in the steady-state corresponding to pre-strain ε_0. The dynamic modulus is defined as

$$|E^*| = \Delta\sigma/\Delta\varepsilon \tag{B.3}$$

We schematically show the dynamic modulus as the slope of the solid curve that connects the upper-right corner and the lower-left corner in Fig. B.5. The loss factor is defined as

$$\tan(\delta) = \tan\left[\sin^{-1}\left(\frac{W_d}{W_d^{\max}}\right)\right] \tag{B.4}$$

where W_d is the dissipated energy per cycle per unit volume (see the gray shaded area in Fig. B.5), and it is calculated as

$$W_d = \int_0^{2\pi/\omega} \sigma(t)\frac{d\varepsilon}{dt}dt \tag{B.5}$$

, and $W_d^{max} = \pi\Delta\sigma\Delta\varepsilon$ (see the orange area in Fig. B.5), representing the maximum energy that the linear viscoelastic material can dissipate per cycle per unit volume.

B.5 The parameters extraction for TangoPlus and DM95

We use the neo-Hookean model for nonlinear springs in all branches of Fig. 2.2. For the neo-Hookean model, the mechanical behaviors are determined by the initial material parameters (initial shear modulus) under small deformation. The mechanical properties under small deformation can be characterized by the DMA test. We also assume that the relaxation times do not change with deformation. So we can get all material parameters

for TangoPlus and DM95 by fitting the viscoelastic model to DMA data. Herein, we use the DMA data of TangoPlus and DM95 from Yuan et al. [163] and Zorzetto et al. [171], respectively. in which the tests are performed at a frequency of 1 Hz. Since the DMA test is executed by scanning temperature, we need to utilize the time-temperature principle (TTSP) to capture the temperature dependence behavior.

Based on the TTSP, τ_α can be calculated from the relaxation time τ_α^R at reference temperature T_{ref} by

$$\tau_\alpha(T) = \alpha(T)\tau_\alpha^R \tag{B.6}$$

where $\alpha\left(T\right)$ is a shift factor, it follows Williams–Landel–Ferry (WLF) equation and Arrhenius type equation as

$$\begin{aligned} \log_{10}[\alpha(T)] &= -\frac{C_1\left(T - T_{ref}\right)}{C_2 + \left(T - T_{ref}\right)}, T > T_{ref} \\ \ln[\alpha(T)] &= -\frac{AF_c}{k}\left(\frac{1}{T} - \frac{1}{T_{ref}}\right), T < T_{ref} \end{aligned} \tag{B.7}$$

where C_1, C_2 and AF_c/k are the material parameters to be extracted.

The relationship between storage modulus and tan δ can be obtained from the DMA test. Theoretically, the dependence of storage modulus $E_s\left(T\right)$, loss modulus $E_l\left(T\right)$ and loss factor tan δ on temperature can be expressed as

$$\begin{aligned} E_s(T) &= E_\infty + \sum_\alpha \frac{E_\alpha \omega^2 \left[\tau_\alpha(T)\right]^2}{1 + \omega^2 \left[\tau_\alpha(T)\right]^2} \\ E_l(T) &= \sum_\alpha \frac{E_\alpha \omega \tau_\alpha(T)}{1 + \omega^2 \left[\tau_\alpha(T)\right]^2} \\ \tan\delta &= \frac{E_l(T)}{E_s(T)} \end{aligned} \tag{B.8}$$

where E_∞ and E_α are initial tensile modulus of the equilibrium branch and α^{th} nonlinear

spring respectively, ω is the angular frequency used in the DMA test. We assume the TangoPlus to be incompressible, so the μ_∞ and μ_m can be derived as $\mu_\infty = E_\infty/3$ and $\mu_\alpha = E_\alpha/3$. We fit the Eq. B.8 to the DMA data (see the markers in Fig B.6) for extracting the parameters including E_∞, E_α, τ_α^R, C_1, C_2, T_{ref} and AF_c/k. In particular, we simultaneously fit storage modulus and tan δ, and the fitting results are shown in Fig B.6) (see the dashed curves). The fitting results show good agreement with the experimental data, indicating the reliability of the extracted parameters.

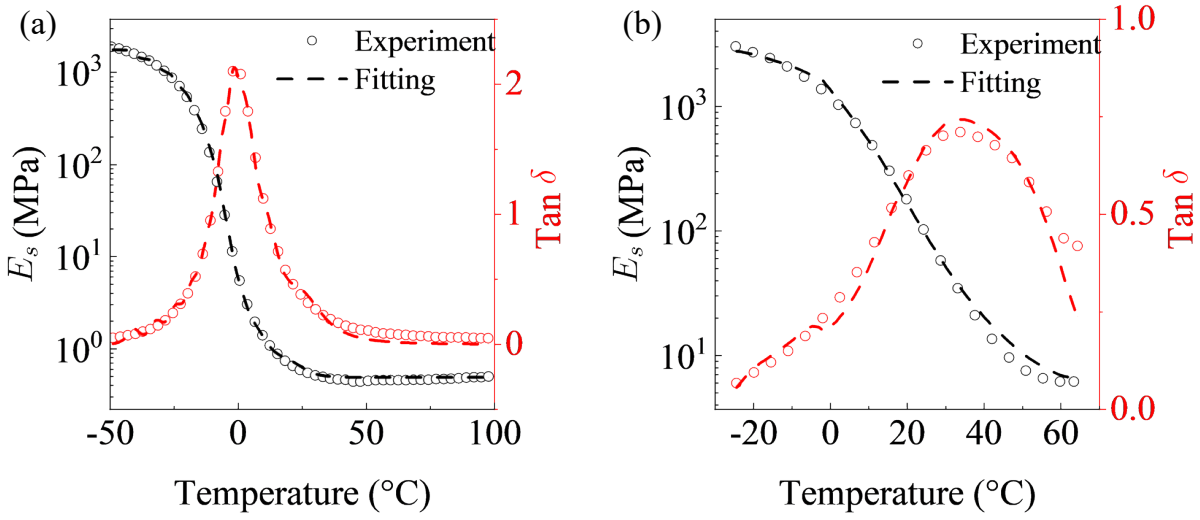

Figure B.6: Fitting curves of the DMA results for (a) TangoPlus and (b) DM95 (The data are extracted from Yuan et al. [163] and Zorzetto et al. [171]).

Recall that we conduct our in-plane compression tests at room temperature 21^oC. To simulate the deformation process of particulate composites, we need to obtain the relaxation time at room temperature by scaling the parameters at the reference temperature with a shift factor through Eqs. B.6 and B.6. The corresponding strain-energy factors and relaxation times for TangoPlus and DM95 under room temperature are listed in Table B.1 and Table B.2.

Table B.1: The material parameters for TangoPlus

Branch (m)	β_m	τ_m (Unit: s)	Branch (m)	β_m	τ_m (Unit: s)
1	733.73	9.35E-11	6	210.28	3.60E-05
2	779.24	4.38E-09	7	40.60	2.37E-04
3	771.50	8.26E-08	8	7.05	0.0017
4	626.76	9.10E-07	9	1.96	0.016
5	426.89	6.50E-06	10	0.65	0.25
E_∞ (MPa)	0.49	C_2 (^{o}C)	45.07		
μ_∞ (MPa)	0.1633	T_{ref} (^{o}C)	-6.75		
C_1	8.76	AF_c/k	-24411.13		

Table B.2: The material parameters for DM95

Branch (m)	β_m	τ_m(Unit: s)	Branch (m)	β_m	τ_m(Unit: s)
1	1.29E+01	1.55E-08	15	2.23E+01	2.29E-03
2	1.96E+01	1.58E-08	16	2.04E+01	7.51E-03
3	3.68E+01	3.84E-08	17	1.79E+01	2.69E-02
4	1.01E+01	9.33E-08	18	9.96E+00	9.44E-02
5	1.21E+01	1.35E-07	19	6.93E+00	2.58E-01
6	3.13E+01	1.75E-07	20	4.70E+00	6.34E-01
7	2.52E+01	5.25E-07	21	3.83E+00	1.90E+00
8	5.85E+01	8.86E-07	22	2.12E+00	6.04E+00
9	1.37E+01	3.94E-06	23	1.31E+00	1.90E+01
10	3.33E+01	6.43E-06	24	8.28E-01	6.12E+01
11	2.43E+01	1.94E-05	25	4.80E-01	2.21E+02
13	3.06E+01	5.47E-05	26	1.30E-11	9.14E+02
13	2.99E+01	2.00E-04	27	6.80E-15	9.48E+03
14	2.54E+01	7.00E-04			
E_∞ (MPa)	6.18	C_2 (oC)	44.63		
μ_∞ (MPa)	2.06	T_{ref} (oC)	-2.5		
C_1	14.56	AF_c/k	-16000		

B.6 The identification procedures for wavelength of particulate composites

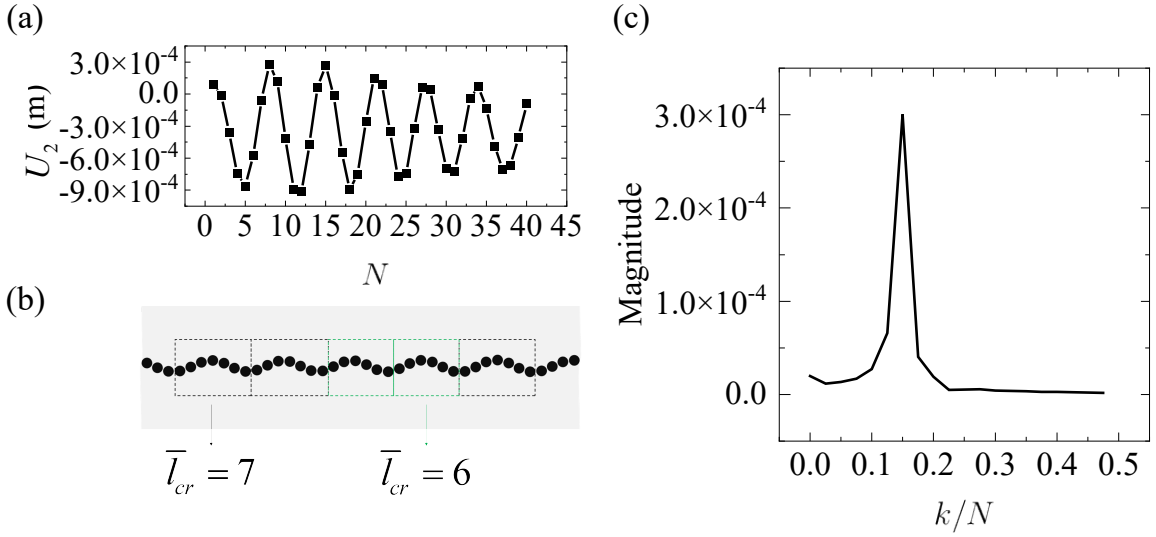

Figure B.7: (a) The displacement of inclusions along the $\mathbf{e_2}$*-direction onset of the buckling; (b) the corresponding buckling shape; (c) the Fourier transformation on the* U_2 *of the inclusions.*

Here, we show the procedure to identify the critical wavelength. After the buckling occurs, we observe that the initial inclusions column transforms into a wavy chain of inclusions. This wavy chain pattern can be described as a discrete pattern by connecting the centers of the stiff inclusions. We consider the displacement of the centers of stiff inclusions in $\mathbf{e}_2$ direction. The position of inclusions along the $\mathbf{e_2}$-direction onset of the buckling is illustrated in Fig B.7 (a). The normalized critical wavelength $\bar{l}_{cr}$ is defined as the number of inclusions in the repeating blocks of the buckled pattern, so $\bar{l}_{cr}$ is expected to be an integer. However, we find that the buckling pattern does not show perfect periodicity. In particular, the buckling pattern contains alternating repeating sets of six and seven inclusions (see Fig B.7 (b)). To quantify the wavelength of irregular quasiperiodic buckling patterns, we apply a Discrete Fourier

Transform (DFT) to the discrete pattern in (a) to characterize the dominant wavelength of the post-buckling pattern.

The position of the centers of the inclusions in $\mathbf{e_2}$-direction is defined as $\{x_n\} := x_1, x_2, x_3 \ldots, x_N$ and the DFT uses a set of harmonic waves with fundamental wavenumber $1/N$ to reassemble the post-buckling pattern $\{x_n\}$. Specifically, N harmonics waves should be selected and the wavenumber of the kth harmonic wave is k/N. The DFT reassembly is defined via

$$x_n = \sum_{k=0}^{N-1} X_k \bullet e^{i2\pi \frac{k}{N} n} \tag{B.9}$$

where the X_k is the Fourier coefficient of the kth harmonic wave. Finally, we determine the dominant harmonic wave for the post-buckling pattern and identify the corresponding wavenumber k/N as the normalized critical wavenumber $\overline{k}_{cr}$, as illustrated in Fig B.7 (c). Then, the normalized critical wavelength is calculated as $\overline{l}_{cr} = 1/\overline{k}_{cr}$. In addition, we observe that the normalized critical wavenumber $\overline{k}_{cr}$ is smaller than 0.5 for all of our simulations, and this observation is physically consistent since there must be at least two inclusions per repeating block of the buckled shape ($\overline{l}_{cr} \geq 2$).

BIBLIOGRAPHY

[1] E. Acome, S. K. Mitchell, T. G. Morrissey, M. B. Emmett, C. Benjamin, M. King, M. Radakovitz, and C. Keplinger. Hydraulically amplified self-healing electrostatic actuators with muscle-like performance. *Science*, 359(6371):61–65, 2018.

[2] M. Agoras, O. Lopez-Pamies, and P. P. Castaneda. Onset of macroscopic instabilities in fiber-reinforced elastomers at finite strain. *Journal of the Mechanics and Physics of Solids*, 57(11):1828–1850, 2009.

[3] K. Alur and J. Meaud. Nonlinear mechanics of non-dilute viscoelastic layered composites. *International Journal of Solids and Structures*, 72:130–143, 2015.

[4] Gayan A. Appuhamillage, Nicholas Chartrain, Viswanath Meenakshisundaram, Keyton D. Feller, Christopher B. Williams, and Timothy E. Long. 110th anniversary: Vat photopolymerization-based additive manufacturing: Current trends and future directions in materials design. *Industrial and Engineering Chemistry Research*, 58(33):15109–15118, 2019.

[5] N. Arora, A. Batan, J. Li, V. Slesarenko, and S. Rudykh. On the influence of inhomogeneous interphase layers on instabilities in hyperelastic composites. *Materials*, 12(5), 2019.

[6] N. Arora, J. Li, V. Slesarenko, and S. Rudykh. Microscopic and long-wave instabilities in 3d fiber composites with non-gaussian hyperelastic phases. *International Journal of Engineering Science*, 157, 2020.

[7] Nitesh Arora, Jian Li, and Stephan Rudykh. Tunable buckling configurations via

in-plane periodicity in soft 3d-fiber composites: Simulations and experiments. *International Journal of Solids and Structures*, 250, 2022.

[8] Ellen M. Arruda and Mary C. Boyce. A three-dimensional constitutive model for the large stretch behavior of rubber elastic materials. *Journal of the Mechanics and Physics of Solids*, 41(2):389–412, 1993.

[9] R. Avazmohammadi and P. P. Castaneda. Macroscopic constitutive relations for elastomers reinforced with short aligned fibers: Instabilities and post-bifurcation response. *Journal of the Mechanics and Physics of Solids*, 97:37–67, 2016.

[10] Ali Bagheri and Jianyong Jin. Photopolymerization in 3d printing. *ACS Applied Polymer Materials*, 1(4):593–611, 2019.

[11] A. Batra, C. Cohen, and L. Archer. Stress relaxation of end-linked polydimethylsiloxane elastomers with long pendent chains. *Macromolecules*, 38(16):7174–7180, 2005.

[12] R. Baumgartner, A. Kogler, J. M. Stadlbauer, C. C. Foo, R. Kaltseis, M. Baumgartner, G. Y. Mao, C. Keplinger, S. J. A. Koh, N. Arnold, Z. G. Suo, M. Kaltenbrunner, and S. Bauer. A lesson from plants: High-speed soft robotic actuators. *Advanced Science*, 7(5), 2020.

[13] Alberto Beccari, Mohammad J Bereyhi, Robin Groth, Sergey A Fedorov, Amirali Arabmoheghi, Nils J Engelsen, and Tobias J Kippenberg. Hierarchical tensile structures with ultralow mechanical dissipation. *arXiv preprint arXiv:2103.09785*, 2021.

[14] J. S. Bergstrom and M. C. Boyce. Constitutive modeling of the large strain time-dependent behavior of elastomers. *Journal of the Mechanics and Physics of Solids*, 46(5):931–954, 1998.

[15] K. Bertoldi and M. C. Boyce. Wave propagation and instabilities in monolithic and periodically structured elastomeric materials undergoing large deformations. *Physical Review B*, 78(18), 2008.

[16] K. Bertoldi, P. M. Reis, S. Willshaw, and T. Mullin. Negative poisson's ratio behavior induced by an elastic instability. *Adv Mater*, 22(3):361–6, 2010.

[17] K. Bertoldi, V. Vitelli, J. Christensen, and M. van Hecke. Flexible mechanical metamaterials. *Nature Reviews Materials*, 2(11), 2017.

[18] Katia Bertoldi and Oscar Lopez-Pamies. Some remarks on the effect of interphases on the mechanical response and stability of fiber-reinforced elastomers. *Journal of applied mechanics*, 79(3), 2012.

[19] Maurice A Biot. Theory of internal buckling of a confined multilayered structure. *Geological Society of America Bulletin*, 75(6):563–568, 1964.

[20] J Bonada, A Muguruza, Xavier Fernández-Francos, and X Ramis. Influence of exposure time on mechanical properties and photocuring conversion ratios for photosensitive materials used in additive manufacturing. *Procedia Manufacturing*, 13:762–769, 2017.

[21] Katherine Bootsma, Martha M Fitzgerald, Brandon Free, Elizabeth Dimbath, Joe Conjerti, Greg Reese, Dominik Konkolewicz, Jason A Berberich, and Jessica L Sparks. 3d printing of an interpenetrating network hydrogel material with tunable viscoelastic properties. *Journal of the mechanical behavior of biomedical materials*, 70:84–94, 2017.

[22] A. Bossart, D. M. J. Dykstra, J. van der Laan, and C. Coulais. Oligomodal metamaterials with multifunctional mechanics. *Proc Natl Acad Sci U S A*, 118(21), 2021.

[23] David Bushnell. Buckling of shells-pitfall for designers. *AIAA journal*, 19(9):1183–1226, 1981.

[24] F. Campise, L. E. Roth, R. H. Acosta, M. A. Villar, E. M. Vallés, G. A. Monti, and D. A. Vega. Contribution of linear guest and structural pendant chains to relaxational dynamics in model polymer networks probed by time-domain 1h nmr. *Macromolecules*, 49(1):387–394, 2015.

[25] J. C. Case, E. L. White, and R. K. Kramer. Soft material characterization for robotic applications. *Soft Robotics*, 2(2):80–87, 2015.

[26] K. Che, C. Yuan, H. J. Qi, and J. Meaud. Viscoelastic multistable architected materials with temperature-dependent snapping sequence. *Soft Matter*, 14(13):2492–2499, 2018.

[27] K. K. Che, M. Rouleau, and J. Meaud. Temperature-tunable time-dependent snapping of viscoelastic metastructures with snap-through instabilities. *Extreme Mechanics Letters*, 32, 2019.

[28] Dean Chen, Nitesh Arora, Yuhai Xiang, Jian Li, Viacheslav Slesarenko, and Stephan Rudykh. Instability-induced patterns in soft particulate composites. *Under review*, 2022.

[29] L. L. Chen, H. Lian, Z. Liu, H. B. Chen, E. Atroshchenko, and S. P. A. Bordas. Structural shape optimization of three dimensional acoustic problems with isogeometric boundary element methods. *Computer Methods in Applied Mechanics and Engineering*, 355:926–951, 2019.

[30] AB Comsol. Structural mechanics module user's guide. *COMSOL Multiphysics (TM) v*, 5, 2012.

[31] Wayne D Cook and Melinda Johannson. The influence of postcuring on the fracture properties of photo-cured dimethacrylate based dental composite resin. *Journal of biomedical materials research*, 21(8):979–989, 1987.

[32] C. Coulais, J. T. Overvelde, L. A. Lubbers, K. Bertoldi, and M. van Hecke. Discontinuous buckling of wide beams and metabeams. *Phys Rev Lett*, 115(4):044301, 2015.

[33] John G Curro, Dale S Pearson, and Eugene Helfand. Viscoelasticity of randomly crosslinked polymer networks. relaxation of dangling chains. *Macromolecules*, 18(6):1157–1162, 1985.

[34] J. D. Davidson and N. C. Goulbourne. A nonaffine network model for elastomers undergoing finite deformations. *Journal of the Mechanics and Physics of Solids*, 61(8):1784–1797, 2013.

[35] G. Debotton. Transversely isotropic sequentially laminated composites in finite elasticity. *Journal of the Mechanics and Physics of Solids*, 53(6):1334–1361, 2005.

[36] Brian Derby. Printing and prototyping of tissues and scaffolds. *Science*, 338(6109):921–926, 2012.

[37] C. S. Ding, R. R. Deokar, Y. J. Ding, G. Y. Li, X. Y. Cui, K. K. Tamma, and S. P. A. Bordas. Model order reduction accelerated monte carlo stochastic isogeometric method for the analysis of structures with high-dimensional and independent material uncertainties. *Computer Methods in Applied Mechanics and Engineering*, 349:266–284, 2019.

[38] D. M. J. Dykstra, J. Busink, B. Ennis, and C. Coulais. Viscoelastic snapping metamaterials. *Journal of Applied Mechanics-Transactions of the Asme*, 86(11), 2019.

[39] David MJ Dykstra, Shahram Janbaz, and Corentin Coulais. The extreme mechanics of viscoelastic metamaterials. *arXiv preprint arXiv:2204.01375*, 2022.

[40] Sam F Edwards. *The theory of polymer dynamics*. Oxford Univ. Press, 1986.

[41] M. El Hamdaoui, J. Merodio, and R. W. Ogden. Two-phase piecewise homogeneous plane deformations of a fibre-reinforced neo-hookean material with application to fibre kinking and splitting. *Journal of the Mechanics and Physics of Solids*, 143, 2020.

[42] Aflah Elouneg, Danas Sutula, Jérôme Chambert, Arnaud Lejeune, SPA Bordas, and Emmanuelle Jacquet. An open-source fenics-based framework for hyperelastic parameter estimation from noisy full-field data: Application to heterogeneous soft tissues. *Computers and Structures*, 255:106620, 2021.

[43] A Cemal Eringen and JL Wegner. Nonlocal continuum field theories. *Appl. Mech. Rev.*, 56(2):B20–B22, 2003.

[44] LJ Fetters, DJ Lohse, D Richter, TA Witten, and A Zirkel. Connection between polymer molecular weight, density, chain dimensions, and melt viscoelastic properties. *Macromolecules*, 27(17):4639–4647, 1994.

[45] E. Frulloni, J. M. Kenny, P. Conti, and L. Torre. Experimental study and finite element analysis of the elastic instability of composite lattice structures for aeronautic applications. *Composite Structures*, 78(4):519–528, 2007.

[46] P. I. Galich, V. Slesarenko, J. Li, and S. Rudykh. Elastic instabilities and shear waves in hyperelastic composites with various periodic fiber arrangements. *International Journal of Engineering Science*, 130:51–61, 2018.

[47] C. Gao and Y. N. Li. Tuning the wrinkling patterns of an interfacial/coating layer via a regulation interphase. *International Journal of Solids and Structures*, 104:92–102, 2017.

[48] C. Gao, V. Slesarenko, M. C. Boyce, S. Rudykh, and Y. Li. Instability-induced pattern transformation in soft metamaterial with hexagonal networks for tunable wave propagation. *Sci Rep*, 8(1):11834, 2018.

[49] A. N. Gent. A new constitutive relation for rubber. *Rubber Chemistry and Technology*, 69(1):59–61, 1996.

[50] G. Geymonat, S. Muller, and N. Triantafyllidis. Homogenization of nonlinearly elastic-materials, microscopic bifurcation and macroscopic loss of rank-one convexity. *Archive for Rational Mechanics and Analysis*, 122(3):231–290, 1993.

[51] Raphaël N Glaesener, Jan-Hendrik Bastek, Frederick Gonon, Vignesh Kannan, Bastian Telgen, Ben Spöttling, Stephan Steiner, and Dennis M Kochmann. Viscoelastic truss metamaterials as time-dependent generalized continua. *Journal of the Mechanics and Physics of Solids*, 156:104569, 2021.

[52] M. Gomez, D. E. Moulton, and D. Vella. Dynamics of viscoelastic snap-through. *Journal of the Mechanics and Physics of Solids*, 124:781–813, 2019.

[53] A. Goshkoderia, V. Chen, J. Li, A. Juhl, P. Buskohl, and S. Rudykh. Instability-

induced pattern formations in soft magnetoactive composites. *Phys Rev Lett*, 124(15):158002, 2020.

[54] Artemii Goshkoderia and Stephan Rudykh. Stability of magnetoactive composites with periodic microstructures undergoing finite strains in the presence of a magnetic field. *Composites Part B: Engineering*, 128:19–29, 2017.

[55] W. W. Graessley. Entangled linear, branched and network polymer systems - molecular theories. *Advances in Polymer Science*, 47:67–117, 1982.

[56] F. Greco, L. Leonetti, U. De Maio, S. Rudykh, and A. Pranno. Macro- and micro-instabilities in incompressible bioinspired composite materials with nacre-like microstructure. *Composite Structures*, 269, 2021.

[57] F. Greco, L. Leonetti, C. M. Medaglia, R. Penna, and A. Pranno. Nonlinear compressive failure analysis of biaxially loaded fiber reinforced materials. *Composites Part B-Engineering*, 147:240–251, 2018.

[58] F. Greco, P. Lonetti, R. Luciano, P. N. Blasi, and A. Pranno. Nonlinear effects in fracture induced failure of compressively loaded fiber reinforced composites. *Composite Structures*, 189:688–699, 2018.

[59] F. Greco and R. Luciano. A theoretical and numerical stability analysis for composite micro-structures by using homogenization theory. *Composites Part B-Engineering*, 42(3):382–401, 2011.

[60] Fabrizio Greco, Lorenzo Leonetti, Andrea Pranno, and Stephan Rudykh. *Investigation of Microscopic Instabilities in Fiber-Reinforced Composite Materials by Using Multi-scale Modeling Strategies*, pages 571–582. Springer International Publishing, 2019.

[61] Bon Kang Gu, Dong Jin Choi, Sang Jun Park, Min Sup Kim, Chang Mo Kang, and Chun-Ho Kim. 3-dimensional bioprinting for tissue engineering applications. *Biomaterials research*, 20(1):12, 2016.

[62] P. Hauseux, J. S. Hale, and S. P. A. Bordas. Accelerating monte carlo estimation with derivatives of high-level finite element models. *Computer Methods in Applied Mechanics and Engineering*, 318:917–936, 2017.

[63] P. Hauseux, J. S. Hale, S. Cotin, and S. P. A. Bordas. Quantifying the uncertainty in a hyperelastic soft tissue model with stochastic parameters. *Applied Mathematical Modelling*, 62:86–102, 2018.

[64] G. A. Holzapfel. On large strain viscoelasticity: Continuum formulation and finite element applications to elastomeric structures. *International Journal for Numerical Methods in Engineering*, 39(22):3903–3926, 1996.

[65] Gerhard A. Holzapfel. Nonlinear solid mechanics: A continuum approach for engineering science. *Meccanica*, 37(4/5):489–490, 2002.

[66] Wei Hong. Modeling viscoelastic dielectrics. *Journal of the Mechanics and Physics of Solids*, 59(3):637–650, 2011.

[67] Mokarram Hossain and Zisheng Liao. An additively manufactured silicone polymer: Thermo-viscoelastic experimental study and computational modelling. *Additive Manufacturing*, 35:101395, 2020.

[68] Mokarram Hossain, Rukshan Navaratne, and Djordje Perić. 3d printed elastomeric polyurethane: Viscoelastic experimental characterisations and constitutive modelling

with nonlinear viscosity functions. *International Journal of Non-Linear Mechanics*, page 103546, 2020.

[69] Y. Huang, C. L. Zhang, and W. Q. Chen. Tuning band structures of two-dimensional phononic crystals with biasing fields. *Journal of Applied Mechanics-Transactions of the Asme*, 81(9), 2014.

[70] Hubert M. James and Eugene Guth. Theory of the elastic properties of rubber. *Journal of Chemical Physics*, 11(10):455–481, 1943.

[71] S. Janbaz, K. Narooei, T. van Manen, and A. A. Zadpoor. Strain rate-dependent mechanical metamaterials. *Sci Adv*, 6(25):eaba0616, 2020.

[72] Neda Karami Mohammadi, Pavel I. Galich, Anastasia O. Krushynska, and Stephan Rudykh. Soft magnetoactive laminates: Large deformations, transverse elastic waves and band gaps tunability by a magnetic field. *Journal of Applied Mechanics*, 86(11), 2019.

[73] Hesam Khajehsaeid. Application of fractional time derivatives in modeling the finite deformation viscoelastic behavior of carbon-black filled nr and sbr. *Polymer Testing*, 68:110–115, 2018.

[74] S. H. Kim, Y. K. Yeon, J. M. Lee, J. R. Chao, Y. J. Lee, Y. B. Seo, M. T. Sultan, O. J. Lee, J. S. Lee, S. I. Yoon, I. S. Hong, G. Khang, S. J. Lee, J. J. Yoo, and C. H. Park. Precisely printable and biocompatible silk fibroin bioink for digital light processing 3d printing. *Nat Commun*, 9(1):1620, 2018.

[75] Yoonho Kim, Hyunwoo Yuk, Ruike Zhao, Shawn A Chester, and Xuanhe Zhao. Print-

ing ferromagnetic domains for untethered fast-transforming soft materials. *Nature*, 558(7709):274–279, 2018.

[76] X. Kuang, J. Wu, K. Chen, Z. Zhao, Z. Ding, F. Hu, D. Fang, and H. J. Qi. Grayscale digital light processing 3d printing for highly functionally graded materials. *Sci Adv*, 5(5):eaav5790, 2019.

[77] Aditya Kumar and Oscar Lopez-Pamies. On the two-potential constitutive modeling of rubber viscoelastic materials. *Comptes Rendus Mécanique*, 344(2):102–112, 2016.

[78] Roderic Lakes. *Viscoelastic materials*. Cambridge university press, 2009.

[79] Alexander K Landauer, Xiuqi Li, Christian Franck, and David L Henann. Experimental characterization and hyperelastic constitutive modeling of open-cell elastomeric foams. *Journal of the Mechanics and Physics of Solids*, 133:103701, 2019.

[80] S. R. Lavoie, P. Millereau, C. Creton, R. Long, and T. Tang. A continuum model for progressive damage in tough multinetwork elastomers. *Journal of the Mechanics and Physics of Solids*, 125:523–549, 2019.

[81] Jim H Lee, Robert K Prud'Homme, and Ilhan A Aksay. Cure depth in photopolymerization: Experiments and theory. *Journal of Materials Research*, 16(12):3536–3544, 2001.

[82] J. Li, N. Arora, and S. Rudykh. Elastic instabilities, microstructure transformations, and pattern formations in soft materials. *Current Opinion in Solid State and Materials Science*, 25(2), 2021.

[83] J. Li, T. D. Pallicity, V. Slesarenko, A. Goshkoderia, and S. Rudykh. Domain formations and pattern transitions via instabilities in soft heterogeneous materials. *Adv Mater*, 31(14):e1807309, 2019.

[84] J. Li, J. M. Shim, J. Deng, J. T. B. Overvelde, X. L. Zhu, K. Bertoldi, and S. Yang. Switching periodic membranes via pattern transformation and shape memory effect. *Soft Matter*, 8(40):10322–10328, 2012.

[85] J. Li, V. Slesarenko, P. I. Galich, and S. Rudykh. Instabilities and pattern formations in 3d-printed deformable fiber composites. *Composites Part B-Engineering*, 148:114–122, 2018.

[86] J. Li, V. Slesarenko, and S. Rudykh. Auxetic multiphase soft composite material design through instabilities with application for acoustic metamaterials. *Soft Matter*, 14(30):6171–6180, 2018.

[87] J. Li, V. Slesarenko, and S. Rudykh. Microscopic instabilities and elastic wave propagation in finitely deformed laminates with compressible hyperelastic phases. *European Journal of Mechanics a-Solids*, 73:126–136, 2019.

[88] J. Li, V. Slesarenko, and S. Rudykh. Emergence of instability-driven domains in soft stratified materials. *Npj Computational Materials*, 8(1), 2022.

[89] Y. Li, S. Tang, M. Kroger, and W. K. Liu. Molecular simulation guided constitutive modeling on finite strain viscoelasticity of elastomers. *Journal of the Mechanics and Physics of Solids*, 88:204–226, 2016.

[90] Y. N. Li, N. Kaynia, S. Rudykh, and M. C. Boyce. Wrinkling of interfacial layers in stratified composites. *Advanced Engineering Materials*, 15(10):921–926, 2013.

[91] Ying Li, Shan Tang, Brendan C. Abberton, Martin Kröger, Craig Burkhart, Bing Jiang, George J. Papakonstantopoulos, Mike Poldneff, and Wing Kam Liu. A predictive multiscale computational framework for viscoelastic properties of linear polymers. *Polymer*, 53(25):5935–5952, 2012.

[92] Christian Linder, Mykola Tkachuk, and Christian Miehe. A micromechanically motivated diffusion-based transient network model and its incorporation into finite rubber viscoelasticity. *Journal of the Mechanics and Physics of Solids*, 59(10):2134–2156, 2011.

[93] Rong Long, Koichi Mayumi, Costantino Creton, Tetsuharu Narita, and Chung-Yuen Hui. Time dependent behavior of a dual cross-link self-healing gel: Theory and experiments. *Macromolecules*, 47(20):7243–7250, 2014.

[94] Rong Long, H. Jerry Qi, and Martin L. Dunn. Thermodynamics and mechanics of photochemcially reacting polymers. *Journal of the Mechanics and Physics of Solids*, 61(11):2212–2239, 2013.

[95] O. Lopez-Pamies and P. P. Castaneda. On the overall behavior, microstructure evolution, and macroscopic stability in reinforced rubbers at large deformations: I - theory. *Journal of the Mechanics and Physics of Solids*, 54(4):807–830, 2006.

[96] O. Lopez-Pamies and P. P. Castaneda. On the overall behavior, microstructure evolution, and macroscopic stability in reinforced rubbers at large deformations: Ii - application to cylindrical fibers. *Journal of the Mechanics and Physics of Solids*, 54(4):831–863, 2006.

[97] O Lopez-Pamies and P Ponte Castañeda. Microstructure evolution in hyperelastic

laminates and implications for overall behavior and macroscopic stability. *Mechanics of materials*, 41(4):364–374, 2009.

[98] J. Lubliner. A model of rubber viscoelasticity. *Mechanics Research Communications*, 12(2):93–99, 1985.

[99] Yunwei Mao, Shaoting Lin, Xuanhe Zhao, and Lallit Anand. A large deformation viscoelastic model for double-network hydrogels. *Journal of the Mechanics and Physics of Solids*, 100:103–130, 2017.

[100] A. Mazier, A. Bilger, A. E. Forte, I. Peterlik, J. S. Hale, and S. P. A. Bordas. Inverse deformation analysis: an experimental and numerical assessment using the fenics project. *Engineering with Computers*, 2022.

[101] G. P. McKnight and C. P. Henry. Large strain variable stiffness composites for shear deformations with applications to morphing aircraft skins. *Behavior and Mechanics of Multifunctional and Composite Materials 2008*, 6929, 2008.

[102] Y. Meng, W. J. Xu, M. R. Newman, D. S. W. Benoit, and M. Anthamatten. Thermoreversible siloxane networks: Soft biomaterials with widely tunable viscoelasticity. *Advanced Functional Materials*, 29(38), 2019.

[103] J. Merodio and R. W. Ogden. Material instabilities in fiber-reinforced nonlinearly elastic solids under plane deformation. *Archives of Mechanics*, 54(5-6):525–552, 2002.

[104] J. Merodio and R. W. Ogden. Instabilities and loss of ellipticity in fiber-reinforced compressible non-linearly elastic solids under plane deformation. *International Journal of Solids and Structures*, 40(18):4707–4727, 2003.

[105] J. Merodio and R. W. Ogden. Remarks on instabilities and ellipticity for a fiber-reinforced compressible nonlinearly elastic solid under plane deformation. *Quarterly of Applied Mathematics*, 63(2):325–333, 2005.

[106] J. Merodio and R. W. Ogden. Tensile instabilities and ellipticity in fiber-reinforced compressible non-linearly elastic solids. *International Journal of Engineering Science*, 43(8-9):697–706, 2005.

[107] J. Merodio and T. J. Pence. Kink surfaces in a directionally reinforced neo-hookean material under plane deformation: I. mechanical equilibrium. *Journal of Elasticity*, 62(2):119–144, 2001.

[108] J. C. Michel, O. Lopez-Pamies, P. P. Castaneda, and N. Triantafyllidis. Microscopic and macroscopic instabilities in finitely strained fiber-reinforced elastomers. *Journal of the Mechanics and Physics of Solids*, 58(11):1776–1803, 2010.

[109] Christian Miehe and Serdar Göktepe. A micro–macro approach to rubber-like materials. part ii: The micro-sphere model of finite rubber viscoelasticity. *Journal of the Mechanics and Physics of Solids*, 53(10):2231–2258, 2005.

[110] T. Mullin, S. Deschanel, K. Bertoldi, and M. C. Boyce. Pattern transformation triggered by deformation. *Phys Rev Lett*, 99(8):084301, 2007.

[111] W. Muschik. Internal variables in nonequilibrium thermodynamics. *Journal of Non-Equilibrium Thermodynamics*, 15(2):127–137, 1990.

[112] Zaid Muwaffak, Alvaro Goyanes, Vivienne Clark, Abdul W Basit, Stephen T Hilton, and Simon Gaisford. Patient-specific 3d scanned and 3d printed antimicrobial poly-

caprolactone wound dressings. *International journal of pharmaceutics*, 527(1-2):161–170, 2017.

[113] Dayakar L. Naik and Ravi Kiran. On anisotropy, strain rate and size effects in vat photopolymerization based specimens. *Additive Manufacturing*, 23:181–196, 2018.

[114] M. D. Nestorović and N. Triantafyllidis. Onset of failure in finitely strained layered composites subjected to combined normal and shear loading. *Journal of the Mechanics and Physics of Solids*, 52(4):941–974, 2004.

[115] Raymond W Ogden. *Non-linear elastic deformations*. Courier Corporation, 1997.

[116] R. Parnes and A. Chiskis. Buckling of nano-fibre reinforced composites: a re-examination of elastic buckling. *Journal of the Mechanics and Physics of Solids*, 50(4):855–879, 2002.

[117] P. Pathak, N. Arora, and S. Rudykh. Magnetoelastic instabilities in soft laminates with ferromagnetic hyperelastic phases. *International Journal of Mechanical Sciences*, 213, 2022.

[118] Dale S Pearson and Eugene Helfand. Viscoelastic properties of star-shaped polymers. *Macromolecules*, 17(4):888–895, 1984.

[119] Gregory I Peterson, Johanna J Schwartz, Di Zhang, Benjamin M Weiss, Mark A Ganter, Duane W Storti, and Andrew J Boydston. Production of materials with spatially-controlled cross-link density via vat photopolymerization. *ACS applied materials and interfaces*, 8(42):29037–29043, 2016.

[120] G. Y. Qiu and T. J. Pence. Loss of ellipticity in plane deformation of a simple directionally reinforced incompressible nonlinearly elastic solid. *Journal of Elasticity*, 49(1):31–63, 1997.

[121] A. Rafsanjani, K. Bertoldi, and A. R. Studart. Programming soft robots with flexible mechanical metamaterials. *Sci Robot*, 4(29), 2019.

[122] H. Rappel, L. A. A. Beex, L. Noels, and S. P. A. Bordas. Identifying elastoplastic parameters with bayes' theorem considering output error, input error and model uncertainty. *Probabilistic Engineering Mechanics*, 55:28–41, 2019.

[123] S. Reese and S. Govindjee. A theory of finite viscoelasticity and numerical aspects. *International Journal of Solids and Structures*, 35(26-27):3455–3482, 1998.

[124] W. Rosen. Mechanics of composite strengthening. *Fiber Comopsite Materials*, 72, 1964.

[125] S. Rudykh and K. Bertoldi. Stability of anisotropic magnetorheological elastomers in finite deformations: A micromechanical approach. *Journal of the Mechanics and Physics of Solids*, 61(4):949–967, 2013.

[126] S. Rudykh and M. C. Boyce. Transforming wave propagation in layered media via instability-induced interfacial wrinkling. *Phys Rev Lett*, 112(3):034301, 2014.

[127] S. Rudykh and G. deBotton. Instabilities of hyperelastic fiber composites: Micromechanical versus numerical analyses. *Journal of Elasticity*, 106(2):123–147, 2012.

[128] Trisha Sain, Kaspar Loeffel, and Shawn Chester. A thermo–chemo–mechanically cou-

pled constitutive model for curing of glassy polymers. *Journal of the Mechanics and Physics of Solids*, 116:267–289, 2018.

[129] J. J. Schwartz and A. J. Boydston. Multimaterial actinic spatial control 3d and 4d printing. *Nat Commun*, 10(1):791, 2019.

[130] Michael F Shlesinger. Williams-watts dielectric relaxation: a fractal time stochastic process. *Journal of Statistical Physics*, 36(5-6):639–648, 1984.

[131] V. Slesarenko and S. Rudykh. Harnessing viscoelasticity and instabilities for tuning wavy patterns in soft layered composites. *Soft Matter*, 12(16):3677–82, 2016.

[132] V. Slesarenko and S. Rudykh. Microscopic and macroscopic instabilities in hyperelastic fiber composites. *Journal of the Mechanics and Physics of Solids*, 99:471–482, 2017.

[133] Viacheslav Slesarenko and Stephan Rudykh. Towards mechanical characterization of soft digital materials for multimaterial 3d-printing. *International Journal of Engineering Science*, 123:62–72, 2018.

[134] Zhigang Suo. Theory of dielectric elastomers. *Acta Mechanica Solida Sinica*, 23(6):549–578, 2010.

[135] Shan Tang, M. Steven Greene, and Wing Kam Liu. Two-scale mechanism-based theory of nonlinear viscoelasticity. *Journal of the Mechanics and Physics of Solids*, 60(2):199–226, 2012.

[136] N. Triantafyllidis and B. N. Maker. On the comparison between microscopic and macroscopic instability mechanisms in a class of fiber-reinforced composites. *Journal of Applied Mechanics-Transactions of the Asme*, 52(4):794–800, 1985.

[137] N. Triantafyllidis, M. D. Nestorović, and M. W. Schraad. Failure surfaces for finitely strained two-phase periodic solids under general in-plane loading. *Journal of Applied Mechanics*, 73(3):505–515, 09 2005.

[138] Nicolas Triantafyllidis and William C Schnaidt. Comparison of microscopic and macroscopic instabilities in a class of two-dimensional periodic composites. *Journal of the Mechanics and Physics of Solids*, 41(9):1533–1565, 1993.

[139] Clifford Truesdell and Walter Noll. *The non-linear field theories of mechanics*, pages 1–579. Springer, 2004.

[140] E. Y. Urbach and E. Efrati. Predicting delayed instabilities in viscoelastic solids. *Sci Adv*, 6(36), 2020.

[141] W. L. Vandoolaeghe and E. M. Terentjev. Constrained rouse model of rubber viscoelasticity. *J Chem Phys*, 123(3):34902, 2005.

[142] W. L. Vandoolaeghe and E. M. Terentjev. A rouse-tube model of dynamic rubber viscoelasticity. *Journal of Physics a-Mathematical and Theoretical*, 40(49):14725–14744, 2007.

[143] D. A. Vega, L. R. Gomez, L. E. Royh, J. A. Ressia, M. A. Villar, and E. M. Valles. Arm retraction potential of branched polymers in the absence of dynamic dilution. *Phys Rev Lett*, 95(16):166002, 2005.

[144] D. A. Vega, M. A. Villar, J. L. Alessandrini, and E. M. Valles. Terminal relaxation of model poly(dimethylsiloxane) networks with pendant chains. *Macromolecules*, 34(13):4591–4596, 2001.

[145] K. Vithani, A. Goyanes, V. Jannin, A. W. Basit, S. Gaisford, and B. J. Boyd. An overview of 3d printing technologies for soft materials and potential opportunities for lipid-based drug delivery systems. *Pharm Res*, 36(1):4, 2018.

[146] P. Wang, F. Casadei, S. C. Shan, J. C. Weaver, and K. Bertoldi. Harnessing buckling to design tunable locally resonant acoustic metamaterials. *Physical Review Letters*, 113(1), 2014.

[147] A. Wineman. Nonlinear viscoelastic solids—a review. *Mathematics and Mechanics of Solids*, 14(3):300–366, 2009.

[148] D. Wu, Z. Zhao, Q. Zhang, H. J. Qi, and D. Fang. Mechanics of shape distortion of dlp 3d printed structures during uv post-curing. *Soft Matter*, 15(30):6151–6159, 2019.

[149] Jiangtao Wu, Zeang Zhao, Craig M. Hamel, Xiaoming Mu, Xiao Kuang, Zaoyang Guo, and H. Jerry Qi. Evolution of material properties during free radical photopolymerization. *Journal of the Mechanics and Physics of Solids*, 112:25–49, 2018.

[150] Y. H. Xiang, C. Schilling, N. Arora, A. J. Boydston, and S. Rudykh. Mechanical characterization and constitutive modeling of visco- hyperelasticity of photocured polymers. *Additive Manufacturing*, 36, 2020.

[151] Y. H. Xiang, D. M. Zhong, S. Rudykh, H. F. Zhou, S. X. Qu, and W. Yang. A review of physically based and thermodynamically based constitutive models for soft materials. *Journal of Applied Mechanics-Transactions of the Asme*, 87(11), 2020.

[152] Y. H. Xiang, D. M. Zhong, P. Wang, T. H. Yin, H. F. Zhou, H. H. Yu, C. Baliga, S. X. Qu, and W. Yang. A physically based visco-hyperelastic constitutive model for soft materials. *Journal of the Mechanics and Physics of Solids*, 128:208–218, 2019.

[153] Y.H. Xiang, D.A. Chen, N. Arora, and S. Rudykh. Towards understanding the role of viscoelasticity in instabilities in soft particulate composite. *In Preparation*, 2022.

[154] Yuhai Xiang, Danming Zhong, Peng Wang, Guoyong Mao, Honghui Yu, and Shaoxing Qu. A general constitutive model of soft elastomers. *Journal of the Mechanics and Physics of Solids*, 117:110–122, 2018.

[155] H. Yamazaki, M. Takeda, Y. Kohno, H. Ando, K. Urayama, and T. Takigawa. Dynamic viscoelasticity of poly(butyl acrylate) elastomers containing dangling chains with controlled lengths. *Macromolecules*, 44(22):8829–8834, 2011.

[156] C. Yang, M. Boorugu, A. Dopp, J. Ren, R. Martin, D. Han, W. Choi, and H. Lee. 4d printing reconfigurable, deployable and mechanically tunable metamaterials. *Materials Horizons*, 6(6):1244–1250, 2019.

[157] D. Yang, B. Mosadegh, A. Ainla, B. Lee, F. Khashai, Z. G. Suo, K. Bertoldi, and G. M. Whitesides. Buckling of elastomeric beams enables actuation of soft machines. *Advanced Materials*, 27(41):6323–+, 2015.

[158] Lin Yn-hwang. *Polymer viscoelasticity: Basics, molecular theories and experiments*. World Scientific, 2003.

[159] K. Yu, A. J. W. McClung, G. P. Tandon, J. W. Baur, and H. J. Qi. A thermomechanical constitutive model for an epoxy based shape memory polymer and its parameter identifications. *Mechanics of Time-Dependent Materials*, 18(2):453–474, 2014.

[160] Kunhao Yu, An Xin, and Qiming Wang. Mechanics of light-activated self-healing polymer networks. *Journal of the Mechanics and Physics of Solids*, 124:643–662, 2019.

[161] P. Yu, S. P. A. Bordas, and P. Kerfriden. Adaptive isogeometric analysis for transient dynamics: Space-time refinement based on hierarchical a-posteriori error estimations. *Computer Methods in Applied Mechanics and Engineering*, 394, 2022.

[162] C. Yuan, X. M. Mu, C. K. Dunn, J. Haidar, T. J. Wang, and H. J. Qi. Thermomechanically triggered two-stage pattern switching of 2d lattices for adaptive structures. *Advanced Functional Materials*, 28(18):1705727, 2018.

[163] C. Yuan, F. F. Wang, B. Y. Qi, Z. Ding, D. W. Rosen, and Q. Ge. 3d printing of multi-material composites with tunable shape memory behavior. *Materials and Design*, 193:108785, 2020.

[164] M. Zarrelli, A. A. Skordos, and I. K. Partridge. Toward a constitutive model for cure-dependent modulus of a high temperature epoxy during the cure. *European Polymer Journal*, 46(8):1705–1712, 2010.

[165] Quan Zhang and Stephan Rudykh. Magneto-deformation and transverse elastic waves in hard-magnetic soft laminates. *Mechanics of Materials*, 169, 2022.

[166] YP Zhao. Modern continuum mechanics, 2016.

[167] Z. Zhao, X. Mu, N. Sowan, Y. Pei, C. N. Bowman, H. Jerry Qi, and D. Fang. Effects of oxygen on light activation in covalent adaptable network polymers. *Soft Matter*, 11(30):6134–44, 2015.

[168] Xiaoyu Zheng, Howon Lee, Todd H Weisgraber, Maxim Shusteff, Joshua DeOtte, Eric B Duoss, Joshua D Kuntz, Monika M Biener, Qi Ge, and Julie A Jackson. Ultralight, ultrastiff mechanical metamaterials. *Science*, 344(6190):1373–1377, 2014.

[169] D. M. Zhong, Y. H. Xiang, T. H. Yin, H. H. Yu, S. X. Qu, and W. Yang. A physically-based damage model for soft elastomeric materials with anisotropic mullins effect. *International Journal of Solids and Structures*, 176:121–134, 2019.

[170] Jianyou Zhou, Liying Jiang, and Roger E. Khayat. A micro–macro constitutive model for finite-deformation viscoelasticity of elastomers with nonlinear viscosity. *Journal of the Mechanics and Physics of Solids*, 110:137–154, 2018.

[171] L. Zorzetto, L. Andena, F. Briatico-Vangosa, L. De Noni, J. M. Thomassin, C. Jerome, Q. Grossman, A. Mertens, R. Weinkamer, M. Rink, and D. Ruffoni. Properties and role of interfaces in multimaterial 3d printed composites. *Sci Rep*, 10(1):22285, 2020.